eman ta zabal zazu

Universidad del País Vasco
Euskal Herriko Unibertsitatea

Departamento de Ingeniería Mecánica / Ingeniaritza Mekanikoa Saila

Experimental and numerical research on some fundamental aspects of the WEDM process

Jun Wang

Experimental and numerical research on some fundamental aspects of the WEDM process

Ph.D. THESIS

Jun Wang

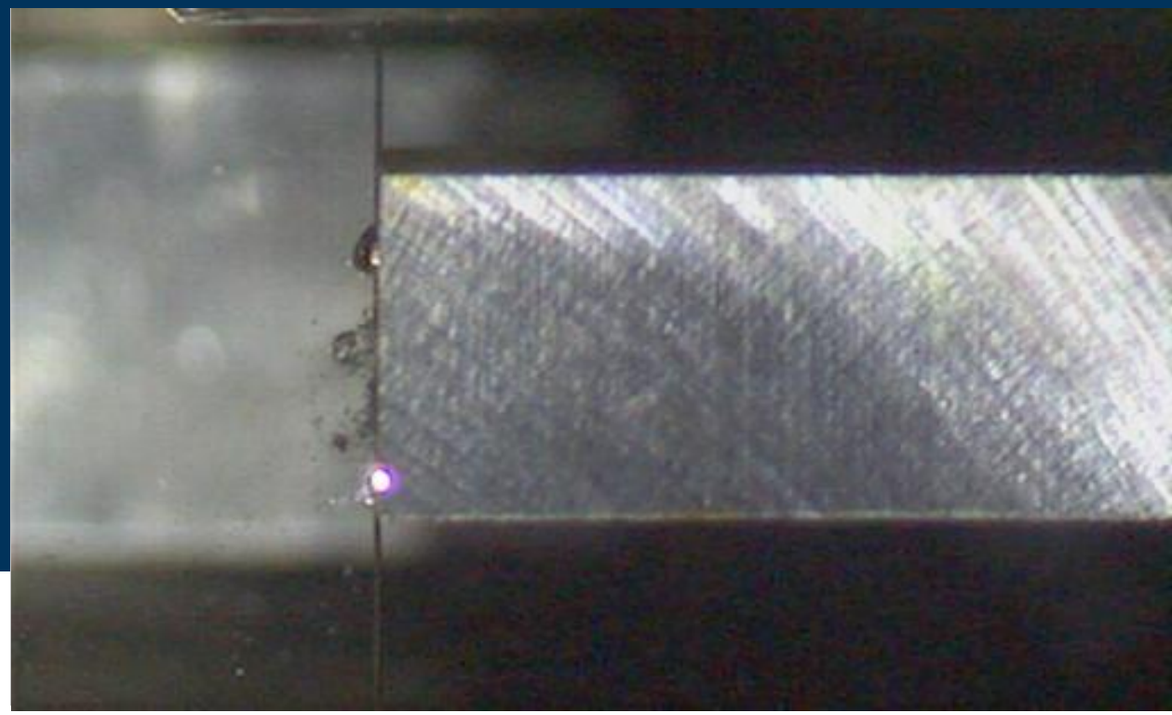

THESIS ADVISORS

Dr. José Antonio Sánchez

Dr. Borja Izquierdo

February 2023, Bilbao

eman ta zabal zazu

Universidad del País Vasco
Euskal Herriko Unibertsitatea

INGENIARITZA MEKANIKOA SAILA
DEPARTAMENTO DE INGENIERÍA MECÁNICA

Universidad del País Vasco Euskal Herriko Unibertsitatea

NAZIOARTEKO BIKAINTASUN CAMPUSA
CAMPUS DE EXCELENCIA INTERNACIONAL

Ph.D. THESIS

EXPERIMENTAL AND NUMERICAL RESEARCH ON SOME FUNDAMENTAL ASPECTS OF THE WEDM PROCESS

Presented by:

Jun Wang

Thesis advisors:

Prof. Dr. José Antonio Sánchez Galíndez

Prof. Dr. Borja Izquierdo Aramburu

January 2023, Bilbao

Universidad del País Vasco Euskal Herriko Unibertsitatea

NAZIOARTEKO BIKAINTASUN CAMPUSA
CAMPUS DE EXCELENCIA INTERNACIONAL

Ph.D. THESIS

EXPERIMENTAL AND NUMERICAL RESEARCH ON SOME FUNDAMENTAL ASPECTS OF THE WEDM PROCESS

Presented to obtain the degree of

Doctor in Mechanical Engineering

Presented by:

Jun Wang

Thesis advisors:

Prof. Dr. José Antonio Sánchez Galíndez

Prof. Dr. Borja Izquierdo Aramburu

January 2023, Bilbao

ACKNOWLEDGEMENTS

It is time to finish this fantastic journey of my Ph.D. study. During these more than 4 years I received a lot of kind help from professors, workmates, friends and family. It is impossible to finish this work without your support. Hence, I want to express my sincere thanks here.

To my tutor José Antonio. You always gave me advice and help not only in my research but also in my life with your wisdom, kindness and patience. You helped me to overcome the hardest time in the process of getting used to a different cultural environment. Thank you so much and you are someone who means a lot to my life.

To my advisor Borja. I got much advice when I had doubts in the process of my research. You made a lot of good suggestions with your wisdom and experience. I feel very grateful for your guidance and help in my Ph.D. study.

To Izaro. Thank you for your help and support as always since I arrive at CFAA. I enjoyed a lot the discussion about the work and the communication with you. You gave me a lot of guidance in the practical work. By the way, your laugh sound is iconic and impressive and can be heard from far away.

To Mª José. You are always so kind to me. Also, I got much help when I met difficulties with the procedure of the document application at the university. I am very grateful for your help and kindness.

To my friend Jon Ander. From I arrived at CFAA you gave me a lot of support in work and life. We shared the happiness of a lot of important things in the life of each other. I wish everything goes well in your new work and enjoy life with Yasmin and your baby.

To my friend Ibon. You called me to climb mountains and took me to meet your family and your friends. You always tried to make me not feel alone here. Thank you so much, my friend. We will have more time in the future to share more happiness.

To all my friends in China, Spain and Japan. We spent many happy times in different stages of these years. Although it may be difficult to have many chances to meet in person, all of you are an important component of my life and I will remember the happy moments.

To workmates. I received friendly treatment from all my workmates in CFAA and university when I need help. Even though maybe I can not remember all the names of everyone but I want to say thank you to you all.

To my love Juan. Thank you for your appearance in my life. Your company and support

always help me to overcome difficulties. We will continue sharing all the life in the future. I love you darling.

To my parents. Thank you, mother. Thank you, father. I could not get here without your support and your love. All the emotions come together in one sentence, I love you forever.

Finally, I would like to thank myself for the persistence in the Ph.D. study. This thesis is the summary of one important stage of my life and it will also bring a new starting point for the next stage.

Keep going and keep being kind.

Jun

CONTENT

Figures

Tables

Nomenclature

A_{remove}	Removed area (μm^2)
$A_{recastlayer}$	Recast layer area (μm^2)
C_p	Specific heat capacity in solid state (J/kg·K)
C_m	Equivalent specific heat in the melting process (J/kg·K)
C_{ev}	Equivalent specific heat in the evaporation process (J/kg·K)
CFD	Computational Fluid Dynamic
CNC	Computer Numerical Control
D_c	Crater diameter (μm)
d_c	Crater depth (μm)
d_{ceq}	Crater depth calculated by equation (μm)
DEV_d	Equation deviation of crater depth
DEV_R	Equation deviation of crater radius
DEV_v	Equation deviation of crater volume
E	Equation error
E_o	Energy density (J/m^3)
EDM	Electrical Discharge Machining
EDX	Energy Dispersive X-ray spectroscopy

F	Wire tension (N)
FEM	Finite Element Method
f	Wire winding speed (mm/min)
f_c	Fraction of total heat transfer to workpiece (%)
g	Gap width (µm)
h	Workpiece thickness (mm)
H	Distance between two nozzles (mm)
H_1	Placement heights of the sheet workpiece (mm)
I	Current (A)
I_{upper}	Upper circuit current (A)
I_{lower}	Lower circuit current (A)
k	Relation between upper and lower circuit current
l	Cutting length (mm)
L_{ev}	Latent heat of evaporation (kJ/kg)
L_m	Latent heat of melting (kJ/kg)
M_1	Weight of electrodes before machining (kg)
M_2	weight of electrodes after machining (kg)
MOE	Modulus of elasticity (MPa)

n	Number of discharge that still does not occur
N	Number of discharges
PFE	Plasma flushing efficiency (%)
q_0	Maximum intensity at the axis of a spark (W/m^2)
Q	Discharge power (W/m^2)
Q_f	Volume flushing flow rate (L/min)
$Q(r)$	Gaussian heat flux (W/m^2)
r	Distance to the center of heat source (μm)
R_a	Mean surface roughness (μm)
R_c	Crater radius (μm)
R_{ceq}	Crater radius calculated by equation
R_p	Plasma channel radius (μm)
R_z	Maximum surface roughness (μm)
$SEDM$	Sinking Electrical Discharge Machining
SEM	Scanning electron microscopy
S_x	Wire movement in the x-direction (μm)
S_y	Wire movement in the y-direction (μm)
t	Time (s)

t_a	Current rise time (s)
t_d	Discharge delay time (μs)
$t_{d,ave}$	Average discharge delay time (μs)
t_{on}	Pulse on time (μs)
t_{off}	Pulse interval (μs)
T	Temperature (K)
T_{ev}	Boiling temperature (K)
TEM	Transmission Electron Microscope
T_m	Melting temperature (K)
T_{ref}	Ambient temperature (K)
U	Voltage (V)
U_o	Open Voltage (V)
U_s	Servo Voltage (V)
V_c	Crater volume (μm^3)
V_{ceq}	Crater volume calculated by equation (μm^3)
$V_{discharge}$	Average removal capacity of each discharge (μm^3)
$V_{simulation}$	Removal volume gotten from the simulation (μm^3)
w	Kerf width (μm)

x	Coordinate on X-axis
x_0	Initial coordinate on X-axis
x_i	Current coordinate on X-axis
y	Coordinate on Y-axis
y_0	Initial coordinate on Y-axis
y_i	Current coordinate on Y-axis
z	Coordinate on Z-axis
WEDM	Wire Electrical Discharge Machining
α	Thermal diffusivity (mm^2/s)
λ	Thermal conductivity (W/K)
ρ	Density (kg/m^3)

Chapter I: Introduction

I. INTRODUCTION

Wire Electrical Discharge Machining (WEDM) is a non-conventional machining method for the manufacturing of high-added-value components for aerospace, tooling and biomedical implants. It utilizes electric sparks to remove conductive or semi-conductive materials to realize the objective of cutting and obtaining an excellent surface finish that requires no further finishing or polishing. Nowadays, it has become a popular choice for precisely producing intricate shapes with very strict tolerance. Through the data from the Web of Science, as shown in Figure 1, more and more research work in the field of WEDM were published in the recent 20 years. This increasing trend shows that WEDM is seen as a promising machining method.

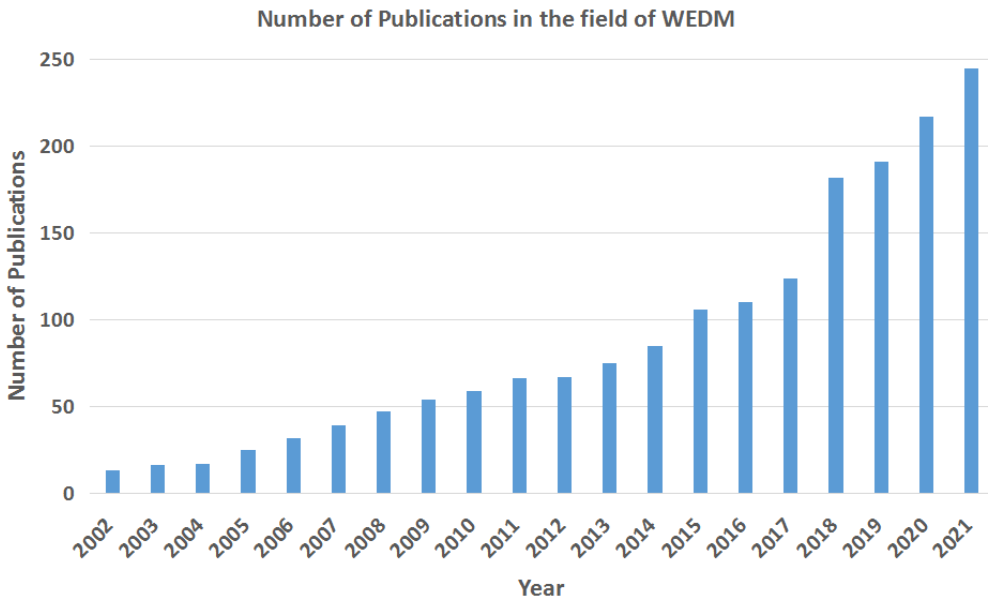

Figure 1. Number of Publications in the field of WEDM [1].

I.1. Industrial context

With the continuous development of technology, more and more super-hard materials are constantly being discovered or synthesized. Among these new materials, there are many materials with better hardness, at the same time, large numbers of precision mechanical parts with new materials, new structures and complex shapes have emerged. Therefore, a series of new problems that need to be solved urgently have been proposed for the mechanical manufacturing industry. For example, the processing of various difficult cutting materials, various structural shape parts, the small or extra-large workpiece, super-precision parts, thin-walled parts, elastic components, and so on. Using traditional processing methods to process these

materials, the tool wear is severe, the surface roughness is high, and the cost of processing is high.

In recent decades, WEDM is becoming more and more important in the modern manufacturing industry, applications for WEDM include the creation of extrusion dies, blanking punches and metal and tool fabrication. WEDM serves many industries making components for automotive, aerospace, medical, energy, mold making, industrial and micro-manufacturing. This fact was attributed to its high-performance involving precision, efficiency, stability and operability and the capacity of machining varying intricate and complex shapes. The WEDM process is used particularly in tooling applications for the machining of various materials. WEDM has been gaining wide acceptance in the machining of various materials used in modern tooling applications. The WEDM process has also evolved as one of the most promising alternatives for the machining of advanced ceramics. Among the different material removal processes, WEDM is considered an effective and economical method in the machining of modern composite materials.

I.2. Development process and latest achievements of WEDM

Electrical Discharge Machining (EDM) was first described by Lazarenko in 1946 [2]. The development of the process was the result of seeking a technique to replace the machined electrode used in EDM. In 1974, D.H. Dulebohn applied the optical-line follower system to automatically control the shape of the component to be machined by the WEDM process [3]. By 1975, its popularity was rapidly increasing, as the process and its capabilities were better understood by the industry [4]. It was only towards the end of the 1970s when Computer Numerical Control (CNC) system was initiated into WEDM that brought about a major evolution of the machining process (Figure 2). As a result, the broad capabilities of the WEDM process were extensively exploited for any through-hole machining owing to the wire, which has to pass through the part to be machined [5].

WEDM is a popular choice for precisely producing intricate shapes and varying tapers in all electrically conductive materials with very close tolerances irrespective of their hardness and toughness. In general, the components produced by WEDM are characterized by a very high added value, because of the complexity of this technology. It is considered an excellent adaptation of the traditional WEDM process, which makes use of an electrode to initialize the sparking process. The WEDM process utilizes electric current to cut conductive materials and also in recent years, with the development of WEDM, semi-conductor ceramic whose electrical resistivity is

between 1 and 3 Ω·m can also be processed [6]. Even the non-traditional WEDM can do the machining of the ceramic [7], [8]. After cutting an excellent surface finish (less than 0.2μm of average roughness, R_a) can be obtained [9], which requires no further finishing or polishing. WEDM is commonly used when low residual stresses are desired, the material is eroded ahead of the wire and there is no direct contact between the workpiece and the wire electrode, eliminating the residual stresses during machining. There is little change in the mechanical properties of a material in WEDM due to its low residual stresses [10].

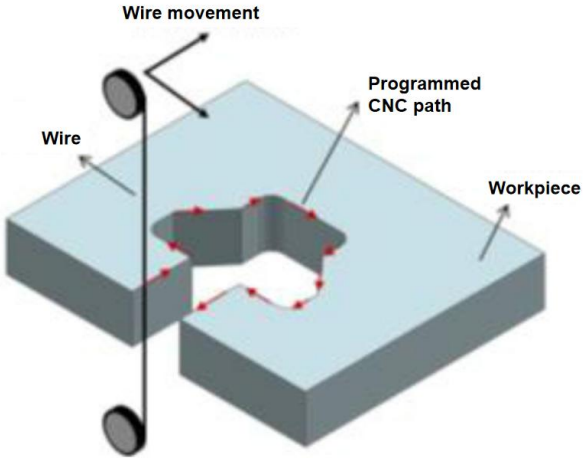

Figure 2. Guides move controlled by CNC.

WEDM mainly uses electric energy to realize the processing of materials. It utilizes a continuously traveling wire electrode made of brass of diameter 0.05–0.3mm, which is capable of achieving the process of machining the workpiece with a very small corner radius. The wire is kept in tension using a mechanical tensioning device reducing the tendency of producing inaccurate parts [11]. In addition, WEDM does not make direct contact between the electrode and the workpiece eliminating mechanical stresses, chatter and vibration problems during machining. Therefore, the WEDM technology is not limited by the material properties and can process any hardness, strength and brittle material.

Figure 3 shows the fundamental concept of electrical discharge machining. Discharge occurs in the gap filled with dielectric liquid between the wire and the workpiece. The role of the dielectric liquid is to prevent the electrolysis effect from acting on the wire and workpiece during a WEDM process. The material erosion mechanism primarily makes use of electrical energy and turns it into thermal energy through a series of discrete electrical discharges occurring between the electrode and workpiece immersed in a dielectric fluid. The thermal energy generates a channel of plasma between the cathode and anode at a temperature in the range of 8000 to 12,000℃ or

as high as 20,000℃ initializing a substantial amount of heating and melting of material at the surface of each pole. When the pulsating direct current supply occurring at the rate of approximately 20,000–30,000Hz is turned off, the plasma channel breaks down [4]. This causes a sudden reduction in the temperature allowing the circulating deionized water [12] to break the plasma channel and flush the molten material from the pole surfaces in the form of microscopic debris. Considering that the temperature drops very sharply, some of the ions are not washed away by the cutting fluid and re-solidified on the surface of the workpiece, then, generating discharge craters on the surface of the workpiece in one discharge. Therefore, the effect of removing excess material from the surface is achieved.

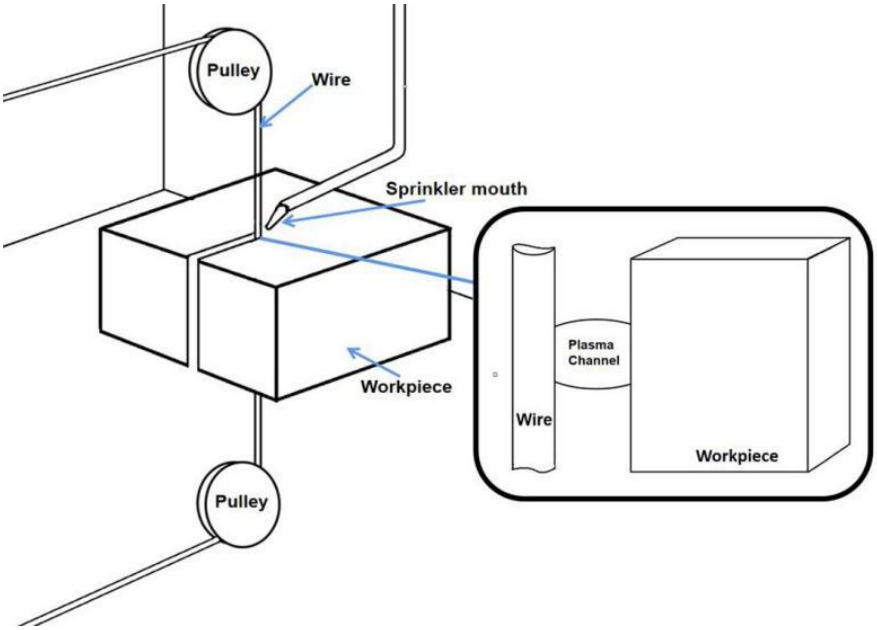

Figure 3. The fundamental concept of WEDM.

With the development of industry, various kinds of WEDM machine tools were manufactured by ONA, AgieCharmilles, Sodick, Makino, Mitsubishi and so on. They are put into use for manufacturing various components with complex shapes and profiles, like fir-tree slot which is an important part of turbine disk in aerospace (Figure 4). Such as AgieCharmilles Cut 200 Dedicated is exclusive for the manufacturing of turbine discs which includes a large number of fir-tree slots. It contains a new B/C tilting rotary table, in-process probing and the company's e-Tracking software, as well as other software functionality to enhance the process of machining large, heavy aerospace parts and make the process to be automated [13].

Furthermore, for improving the stability of the machining process, avoiding wire breakage is an important issue which is needed to be solved. With this aim, recently, GF Machining Solutions has invented a discharge location sensor for doing spark

tracking in the process of machining to avoid the excessive concentration of sparks. Figure 5 shows the principle of this technology briefly. In that, the current value is detected twice from the upper and lower parts respectively. From the spark point, the wire can be divided into two parts of resistance. Also, as the location of each spark is different, with the difference between these two detected current values the position of the spark can be analyzed out. In other words, it can be used to realize spark tracking. In addition, this part will be further introduced in Chapter 2.3.3.

Figure 4. Example of the geometry of fir-tree slot [14].

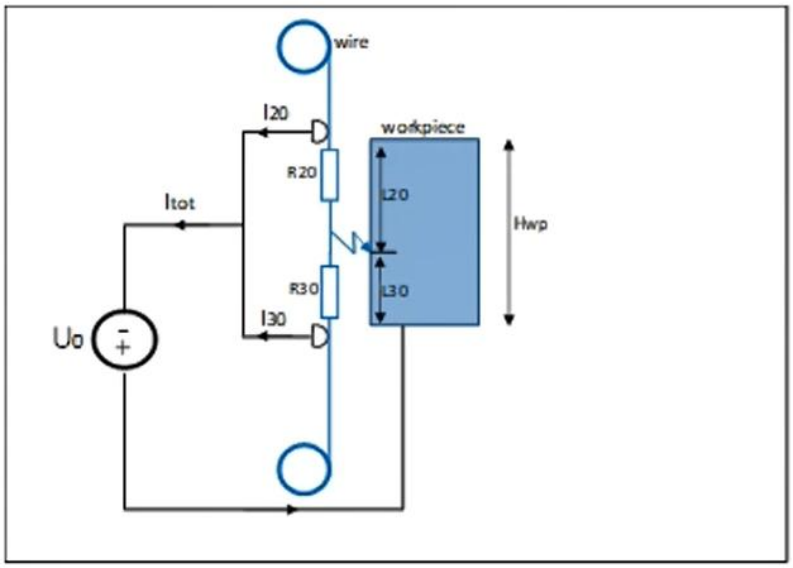

Figure 5. Spark tracking principle of +GF+ technology [15].

Now this discharge location sensor is adopted in the AgieCharmilles CUT P 550 (Figure 6 (a)) WEDM machine. As it has been equipped with this function it can realize the tracking of spark position in the cutting process. In addition, the accuracy of this technology can reach 1µm, which means that the workpiece is divided into several 1µm ranges. In every range, the number of sparks that falls into the corresponding area is recorded. Finally, a complete summary graph of spark tracking can be obtained

in Figure 6(b). Generally, this technology can accurately confirm the intensity and location of sparks along the wire and adjust current and voltage automatically to prevent the concentration of wear on the wire.

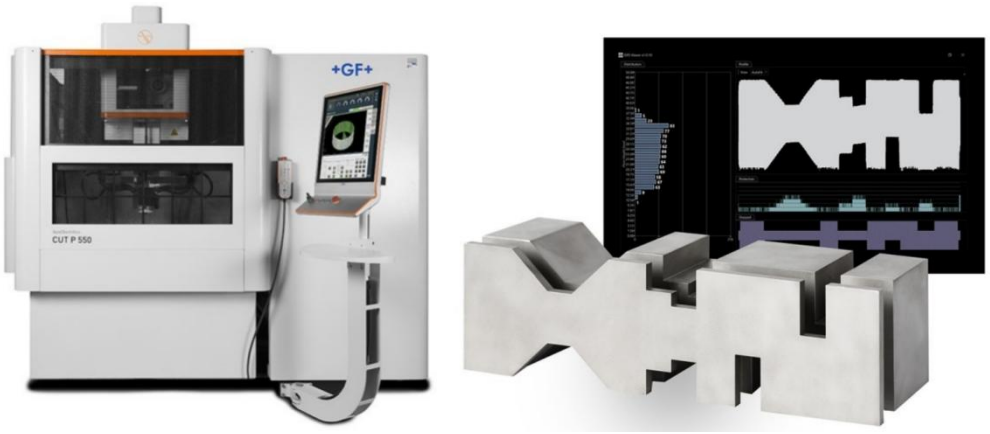

Figure 6. (a) AgieCharmilles CUT P 550 WEDM machine; (b) Result of spark tracking [16].

I.3. Objectives and contributions

The main objectives and contributions of this Ph.D. thesis will be summarized in this section.

To study the influence of different machining conditions on discharge occurrence

The main objective is to explore the discharge occurrence in WEDM. Due to discharge delay time being an important indicator used to distinguish the type of discharge or to judge the discharge situation, a single discharge experiment was finished under different machining conditions to find the possible influencing factor on discharge delay time and the regularity of the influence has been further discussed.

To explore the continuous discharge occurrence during the WEDM process

Because of the short ignition time of discharge and the small gap width, It is hard to understand what happened in the process of continuous discharge and what can influence the continuous discharges occurrent. In this work, observation with a high-speed video camera has been done during the WEDM process. Through the observation result and the discharge delay time analysis, the influence of the bubble on discharge occurrence in WEDM was found and verified for the first time. In addition, the position between continuous discharges was also found and further discussed.

To explore the crater forming in WEDM under different machining parameters

With the objective of better controlling machining parameters in WEDM, it is very important to understand the process of crater forming and the influence of parameters on this process. Several craters on the workpiece generated under different machining conditions were gotten from experiments and further studied. Simultaneously, a thermal model of was built for further understanding of the forming of a crater in detail.

To propose a complete thermal model for the wire wear

The main objective is to build a complete thermal model of the wire considering both latent heat and flushing efficiency. With the result gotten from the simulation and experiment, the precise heat partition ratio to the wire was found for the first time through the inverse fitting.

To study the wire damage caused by continuous discharge to avoid wire breakage

With the aim to understand the influence of discharge accumulation on wire breakage, a discharge location method was designed and verified. With this method, the location of the discharges before wire breakage was found. Then a novel 3D finite element model for studying the craters of consecutive discharge on the wire was built to restore the process of wire breakage and it can be useful for avoiding wire breakage in future work.

To collect and study the debris particles in WEDM

Because of the continuous movement of wire in the machining process, the collection of debris particles is very difficult. For collecting debris particles accurately and efficiently in the process of WEDM, a novel apparatus was designed and produced by a 3D printer. Based on this, the gotten particles were used to observe and analyze. Finally, a complete volume distribution of debris particles was obtained for understanding the matching process in depth.

I.4. Content layout

This thesis starts with the State of the Art of EDM area, in **Chaper II**, the works finished by other researchers about discharge characteristics, debris particles wire breakage and numerical model are described.

Chapter III explores the discharge delay time in WEDM. Through the single discharge experiment, the influence of different machining conditions was found. Then, for further exploring the discharge delay time in the general machining process, the experiment of continuous discharges was also done and further discussed.

Chapter IV describes the exploration through collecting various data on different kinds of craters under different situations of surface roughness and gap width. Simultaneously, a thermal model of a single crater was built for further understanding of the forming of a crater in detail.

Chapter V introduces the study of the wire breakage during the WEDM process. In this chapter, a complete thermal model considering both latent heat and flushing efficiency was built. With this model, several simulations were finished, and by comparing the experimental result and simulation result, the heat partition to the wire was gotten. Then, the effect of heat accumulation in the wire was studied. Furthermore, the sparks before wire breakage were located, based on the gotten position, the simulation of wire with craters was done and the findings allow for a more in-depth understanding of the effect of discharge accumulation on wire breakage.

In Chapter VI, the design and production of a novel apparatus for collecting debris in process of WEDM are presented. With that, debris particles were collected in various WEDM experiments under different processing parameters. Through observation and analysis, a complete volume distribution of particles was obtained.

Finally, **Chapter VII** lists the main conclusions of this thesis and the future research interest that has been found in the research and learning.

Chapter II: State of the art

II. STATE OF THE ART

EDM has become a popular topic in terms of accuracy machining. More and more relevant works were published by various researchers. They are very important for understanding the machining principle and based on the existing work, future studies can be inspired. This chapter aims to study the development process of EDM and several of the latest works in different aspects. Through assessing their contributions and detecting improvement lines to make a critical review of existing works and find novel work direction. The whole content can be divided into the following parts. Firstly, discharge characteristics are included. Then, the debris produced in the process of WEDM is presented. In addition, the wire breakage in WEDM is also discussed. After that, the application of numerical models in WEDM is described.

II.1. Studies on discharge characteristics in EDM

It has been well known that EDM is a removal machining technology through the material melting and even evaporating that is caused by the high temperature emitted by the plasma channel in the process of EDM machining. In other words, in EDM a plasma channel is generated between the electrode and the workpiece, and heat is released. When the surface temperature of the workpiece reaches the melting point or evaporation point, the material will be removed to achieve the processing effect. As the basic processing principle of EDM, the experimental studies on discharge characteristics in EDM play a vital role in the EDM process.

II.1.1 Plasma generation environment

Since in the EDM process, the electrodes are merged into a dielectric liquid, such as oil or deionized water [17], in early research, the environment of plasma generation was generally regarded as a dielectric liquid. In recent years, through more observations, some researchers have found that the plasma generation environment is not only liquid. Kunieda et al. [18] indicated that in the EDM process, much fine dust-like processing debris will be discharged due to the dissolution of the electrode. At the same time, small bubbles are suspended in the gap between the tool electrode and the workpiece. Therefore, the gap condition will constantly change in the whole EDM machining process.

To better understand the influence of different plasma generation environments, single discharge experiments were finished by Yoshida [19] and Takeuchi [20]. As a result, single pulse discharges in gas exhibit larger diameters than those in liquid, and

geometry is also different in both cases. Furthermore, by using transparent electrodes and a high-speed camera, Kitamura et al. [21] finished the observation of the EDM gap phenomena. They proposed that the gap atmosphere also influenced the plasma channel radius. After the observation of the obtained results, it was revealed that most of the discharges occurred in liquid (51% of the events in their observations) followed by the boundary of the bubble (35% of the events). The size and type of the single pulse discharged in gas exhibited larger diameters than those in liquid, and geometry is also different in both cases (Figure 7).

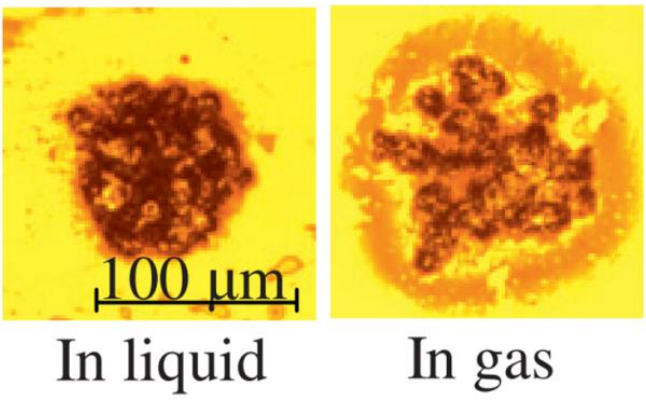

Figure 7. Crater in different gap atmospheres [21].

Besides, Descoeudres [22] pointed out that the main difference between plasma generation in a gas and liquid environment is the density of the medium in which it is decomposed. The higher the density of the liquid, the more difficult it is to generate a discharge. It means that a higher electric field is required to generate a discharge. The breakdown mechanism is also slightly different, compared with the gas environment, the plasma characteristics are strongly affected by the pressure exerted by the surrounding liquid.

Therefore, it can be concluded that plasma is not only generated in a dielectric liquid environment but also in a bubble. With the research of various researchers, including the plasma geometry and characteristics, the difference in EDM discharge in different environments is gradually being revealed. Thus, the plasma generation environment should be an indispensable consideration in future work, and simultaneously it is still worth to further study.

II.1.2 Plasma observation

In recent years, more and more researchers focused on plasma observation for further understanding the plasma with a method more direct. Since in the process of EDM machining the gap width is very small and the duration of plasma is very short, it is

very difficult to do the observation directly. Therefore, spectroscopy was introduced to realize the observation. A spectrum is a pattern in which monochromatic light dispersed by polychromatic light is separated by a dispersion system according to the size of wavelength or frequency. One of the biggest features of spectroscopy is that in many problems of inaccessible and non-damageable objects, when other instruments and other methods are powerless, spectroscopy can be used to observe and solve.

In the work of Descoeudres et al. [23], the plasma generated in the electrical discharge machining process was systematically studied through optical emission spectroscopy. As shown in Figure 8 they found in the typical emission spectrum of plasma, that strong H_α which was emitted by the splitting of atomic hydrogen for dielectric molecules occupied the most part. Also, some other elements such as Cu and Fe that came from two electrodes were found in the spectrum. Furthermore, they successfully obtained the spectrum of plasma in different dielectric liquids including water, oil and liquid nitrogen (Figure 9). With this result, they found that especially under the dielectric of liquid nitrogen, the tool electrode wore out more than the workpieces. This work provides a lot of useful information for further understanding electrode wear.

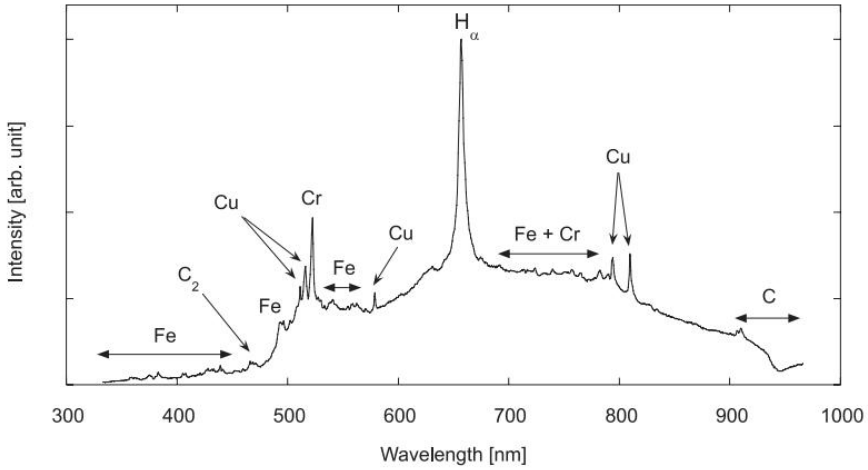

Figure 8. The typical emission spectrum of plasma in SEDM [23].

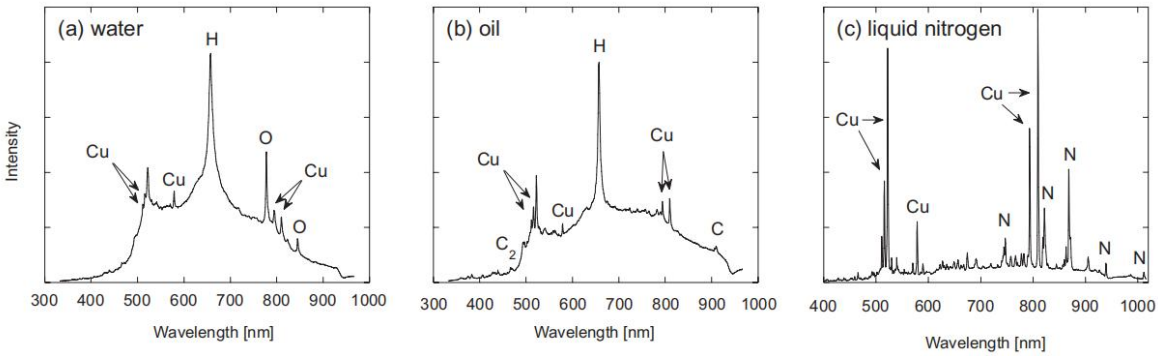

Figure 9. Spectrum under different dielectric liquids [23].

Optical emission spectroscopy was also applied in the work of Nagahanumaiah et al. [24]. They measured the typical emission spectrum of plasma in micro-EDM (Figure 10). Then the average plasma temperature and electron density were gotten through the spectrum. They also discussed the role of the electrode size and spark gap in the machining process of micro-EDM. They concluded that as the size of the electrode decreased and the spark gap increased, the plasma temperature and electron density would increase. This work contributed to a further understanding of the plasma expansion pattern and could be useful for modeling temperature evolution.

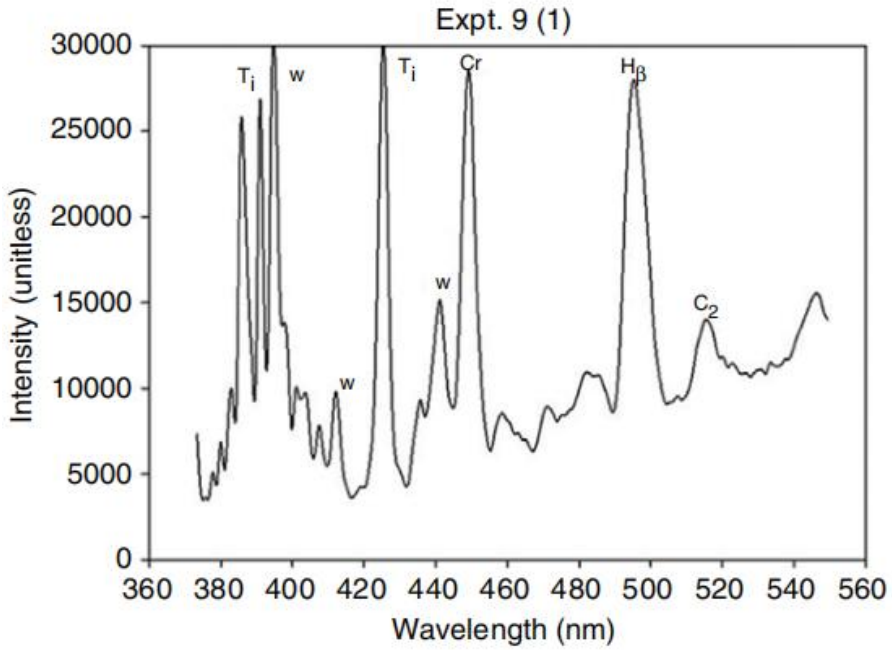

Figure 10. Emission spectrum of plasma in micro-EDM [24].

In addition, Kojima et al. [25] combined the application of spectroscopy and a high-speed video camera. In that, as the trigger, the oscilloscope with the current senor is adopted to decide the timing to capture the photo of plasma and spectrum. As the result, the radial temperature in the plasma is gotten through a series of calculations, and the diameter of the plasma and crater are measured and compared in the different processing conditions (Figure 11). Based on that, they quantified the increase in plasma diameter with changes in discharge current and gap width.

From the introduction above in this section, it can be known that spectroscopy and a high-speed camera can successfully realize the observation and study of plasma. Furthermore, through the result of the researchers' works, it is proved that the observation of plasma in the EDM process is very critical to further understanding the machining principle and the formation of sparks.

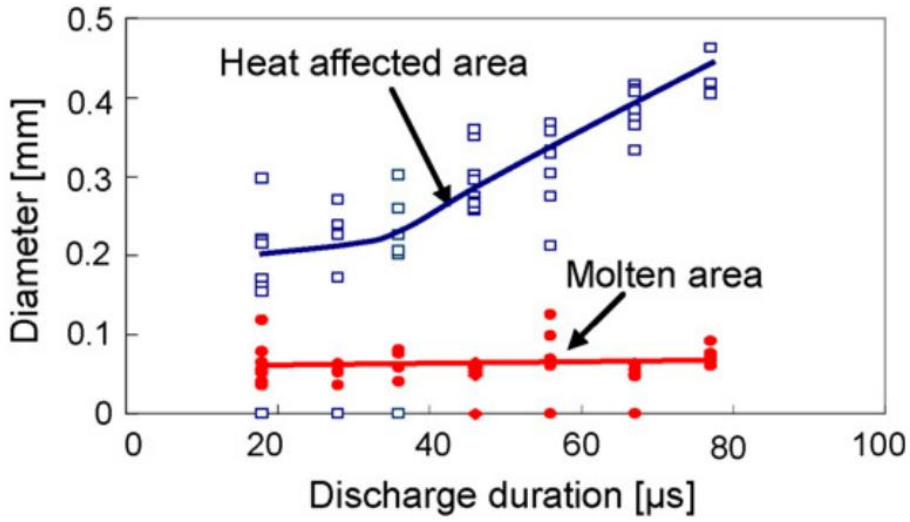

Figure 11. Diameter of plasma and crater are measured and compared in the different processing conditions [25].

II.1.3 Distribution of discharge energy

With the presentation before, it can be known that the plasma channel is the critical element in EDM. As shown in Figure 12, a plasma channel generates between the tool electrode and the workpiece due to the current breakdown. With the generation of the plasma channel, discharge energy mainly flows to the following four parts, they are respectively workpiece, tool electrode, dielectric liquid and debris. Among them, the energy absorbed by the workpiece is the effective energy for electric spark erosion of the material. One part of the energy absorbed by the dielectric liquid is mainly taken away by the high-speed flushing, and part of the energy flows out in the form of radiation, which makes the electrode gap reach a new balance and prepares for the next electric discharge machining. Furthermore, the part of the energy which is absorbed by the workpiece is mainly used for removing material to get the objective of cutting. The part which flows to the wire may cause the wire breakage. Also, a part of the energy is absorbed in the process of debris condensation. Regarding the distribution ratio of discharge energy, many researchers have different viewpoints, which are mainly divided into the fixed energy distribution ratio and the energy distribution ratio with parameter changes.

Regarding the fixed energy distribution ratio, in the early EDM models, it is simply considered that the ratio of energy flowing to the workpiece and the electrode is 50% in the work of Snoeys and Van Dijck [26] and also in the work of James [27], [28]. They assumed that no heat was lost to the dielectric fluid and tool electrodes, and the total heat was only transferred to the workpiece. As in the flushing process, there must be a part of heat loss to the dielectric. Therefore, this assumption is unrealistic.

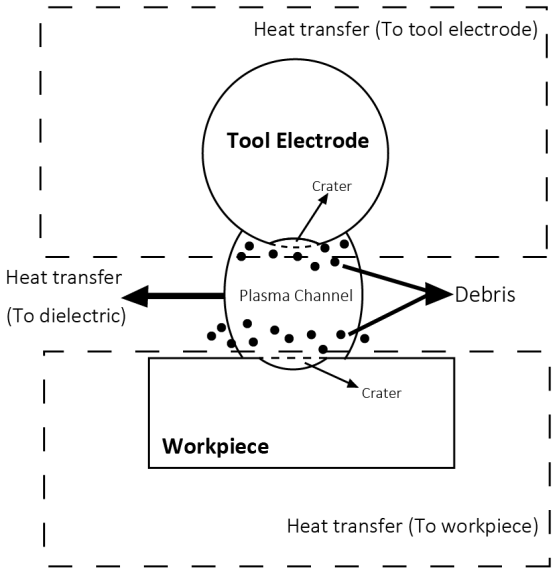

Figure 12. General model of heat transfer in WEDM.

Following one series work of DiBitonto et al. [29] and Patel et al. [30], respectively they build thermal models of cathode and anode. They revealed the complex relationship between the electrode and plasma. Through the model captures the main physical effects they assumed a constant total heat loss to the electrodes. They predicted that the heat absorbed by the anode accounts for about 8% of the total heat. About 18% is absorbed by the cathode and the rest is discharged into the dielectric liquid.

Besides that, Yeo [31] also finished work on the thermal model of anode and cathode in micro-EDM. They proposed a thermal model that combines voltage, current, and pulse on time during material removal to estimate the geometry of the micro pits and predicted the temperature distribution of the workpiece due to a single discharge in the micro-EDM. They combined iterative calculation results with experimental data to determine empirically the fraction of energy transferred to the anode and cathode which are respectively 39% and 14%. Until here, the result of discharge energy distribution is still not persuasive enough.

As a consequence, Izquierdo et al. [32] established the EDM machining erosion divisor model with a finite difference approach (Figure 13). Followed by that they compared it with the experimental discharge craters. They finally obtained 18.8% of the discharge energy flow to the workpiece by using the inverse algorithm. In the part of the energy flow to the tool electrode in WEDM, Banerjee [33] studied the temperature field distribution of the electrode wire during the discharge process, he believed that when the pulse width is 10μs and the electrode wire diameter is 0.25mm, the energy absorbed by the electrode wire accounts for 8.7% of the entire discharge energy. In these two works, the solution of a combination of thermal model and experimental data was used and it makes the result more credible.

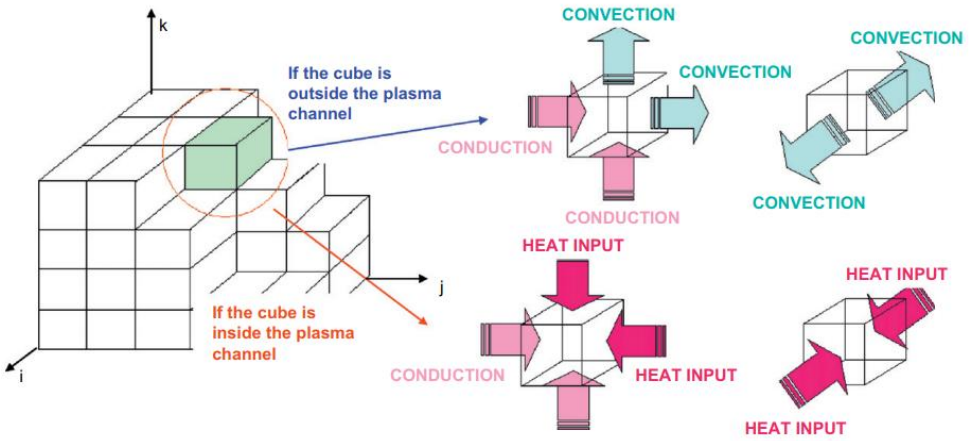

Figure 13. Hexahedral element and boundary conditions in the finite difference-based thermal model [32].

Besides the view that the energy distribution ratio is fixed, at the same time, some researchers believe that the energy allocation ratio will change according to experimental parameters. Singh [34] believes that the distribution ratio of discharge energy is a process that varies with electrical discharge machining parameters and conducted experiments to study the percentage of energy transferred to the workpiece using the heat transfer equation under different EDM parameters. Using theoretical models and experimental fitting methods, it is found that the flow of discharge energy is the curve of discharge current and pulse width, and the energy absorbed by the workpiece ranges from 6.1% to 26.82%.

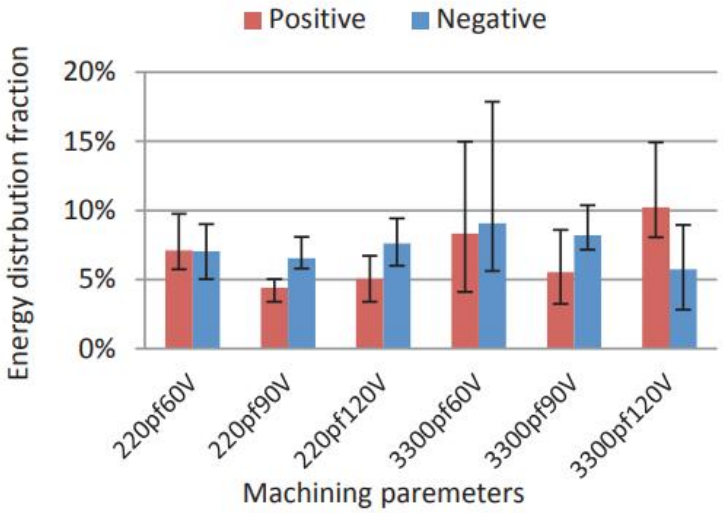

Figure 14. Heat distribution to Anode and Cathode [35].

Moreover, Shao et al. [35] also used a comprehensive miniature EDM electric Finite Element Method (FEM) thermal model to simulate the formation of the crater. In this work, they combined the Gaussian distribution of heat flux, the temperature-related thermal characteristics and the extended plasma radius. As the result, the heat

transfer equation and the experimental measurement of the size of the crater produced are used to determine the energy distribution ratio of the electrode. The final result of pulse energy allocation with the change of machining parameter is shown in Figure 14.

In addition, in the study of single pulse discharge, Hong [36] found that the distribution ratio of discharge energy is related to many factors. When the material is a Titanium alloy, the energy absorbed by the workpiece and the electrode is 10% and 8% respectively. When the workpiece is STAVAX die steel, the energy absorbed by the workpiece and the electrode is 12%. Moreover, processing parameters such as the density of the dielectric, the thermal conductivity of the workpiece, the discharge energy and the pulse current are closely related to the distribution ratio of the discharge energy.

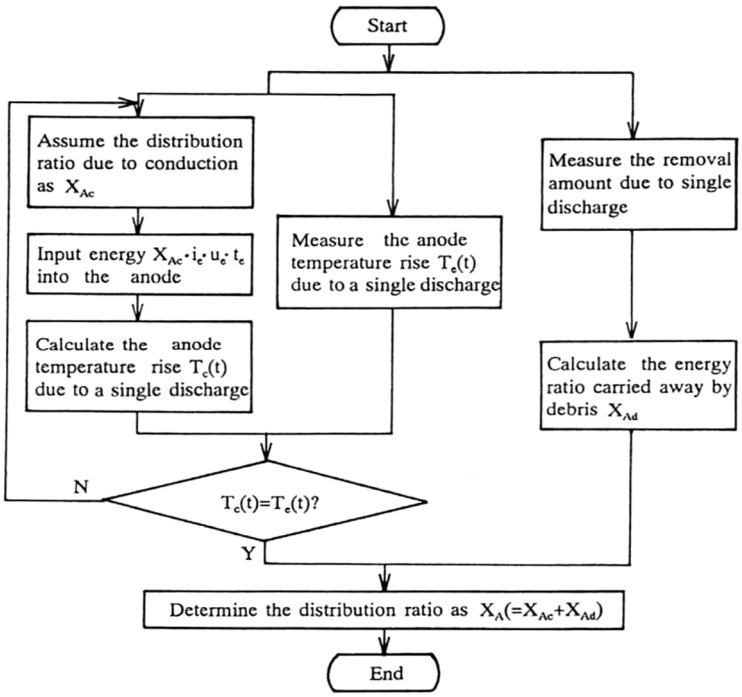

Figure 15. Method of determining the distribution of discharge energy [37].

In order to study the effect of the pulse duration of the discharge current on the removal efficiency in EDM, Xia et al. [37] measured the temperature rise and removal of the electrode during a single discharge to obtain the energy distributed in the anode and cathode. The method is shown in Figure 15, in that, X_{Ac} is the ratio of energy loss due to heat conduction within the anode, X_{Ad} is the ratio of energy carried away by debris, i_e is the pulse current u_e is the discharge voltage and t_e is the pulse on time. As the result, they found that the fraction of energy distributed amongst the electrodes that 30% of the total heat goes to the cathode and 40% goes to the anode.

Besides the works mentioned above, in Figure 16, Klocke et al. [38] also presented a lot of different assumptions of discharge energy distribution. Although many authors have studied the power distribution of a single discharge in the EDM process and the power distribution in a continuous process there is still not a comprehensive model. Therefore obtaining a more accurate ratio of discharge energy distribution is still a good topic to explore. Whereas based on works before, a very important point can be determined is that the combination of the thermal model and the experimental result is a good solution idea for detecting the truth in this problem.

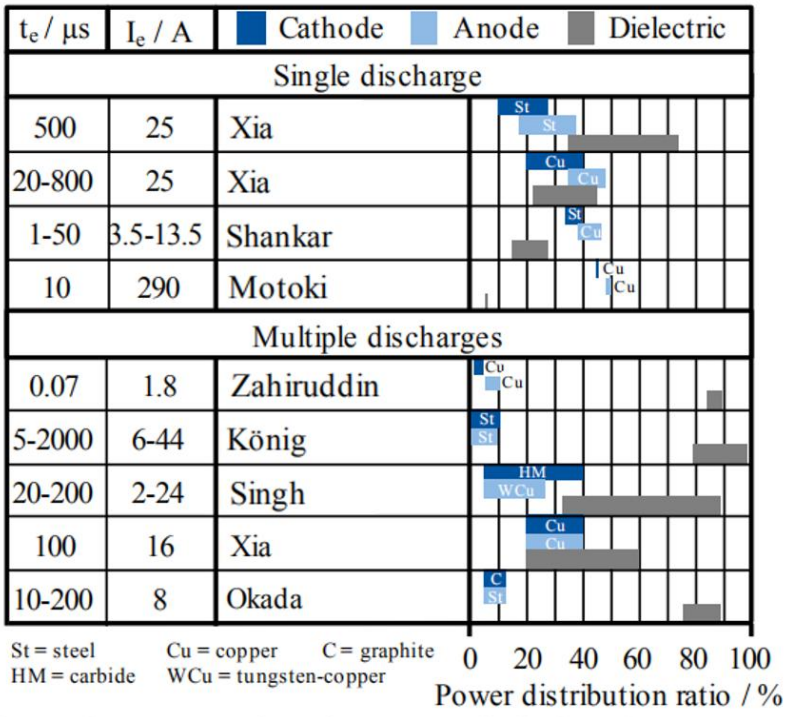

Figure 16. Percentages for energy distribution in the EDM system gotten by different researchers [38].

II.1.4 Geometry of the heat source

After the explanation of heat distribution in the previous part, it can be concluded that the thermal problem is a crucial and complicated point in EDM. Therefore, in this part, the geometry of the heat source will be presented in detail. Nowadays, building a thermal model is an important and effective method in the thermal study area. With thermal simulation software tools, the internal change of heat can be observed and investigated clearly and efficiently. Thence for further learning the thermal problem in WEDM, firstly, the determination of heat source geometry seems particularly important. There are currently many assumptions, including uniform plane heat sources, ring heat sources, point heat sources, and Gaussian plane heat sources.

Firstly, in 1956, Zingerman [39] adopted a uniform plane heat source to obtain an analytical solution for the surface temperature of the workpiece. And then in 1960, Zolotykh [40] used a circular heat source to solve the surface temperature of the workpiece. Following this, in the work of Hocheng et al. [41], they explored the correlation between current and spark on time and used the heat conduction model for the research. In that, as the duration of a single discharge is as short as a few microseconds, they selected an instantaneous point heat source. The existing solution for the induced temperature is shown as Eq.1. where T is the temperature, T_{ref} is the ambient temperature, E_o is the energy intensity, a is the heat diffusivity, t is time, and x, y and z are coordinate on X, Y and Z-axis. This equation shows the temperature change with time at any distance from the heat source. In the end, the experiment successfully compared the material removal rate with ordinary steel based on the thermal conductivity model and predicted the ratio of current, spark on time and crater size.

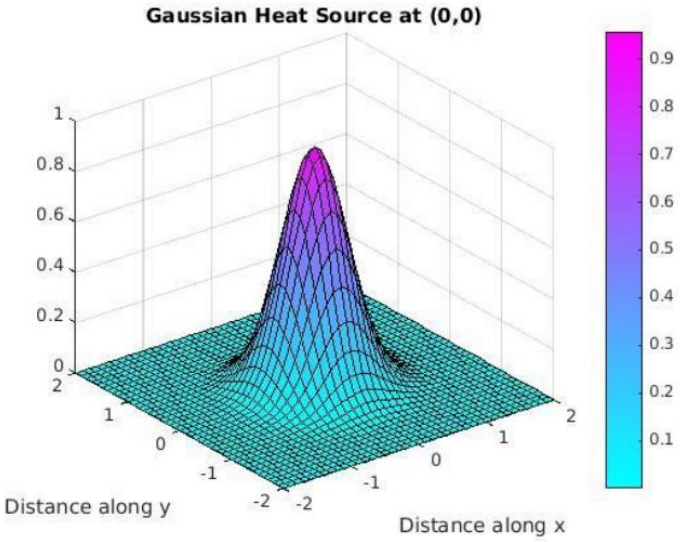

Figure 17. Gaussian heat source [43].

$$T - T_{ref} = \frac{E_o}{8(\pi at)^{3/2}} e^{-[(x-x')^2+(y-y')^2+(z-z')^2]/4at} \quad \text{Eq.1}$$

At present, as shown in Figure 17, the assumption that regards the heat source model as a Gaussian heat source is more popular. Then Yadav [42] verified the reliability of this assumption. The Gaussian heat source equation is shown in Eq.2. In that, $Q(r)$ is the heat flux, q_0 is the maximum intensity at the axis of a spark and its radius is R_p, r is the distance to the center of the heat source. Through the calculation of the surface temperature they found that in the case of applying a Gaussian heat source, a steep temperature gradient is applied in the spark radius area, which is closer to the actual situation.

$$Q(r) = q_0 \exp\left(-4.5\left(\frac{r}{R_p}\right)^2\right) \quad \text{Eq.2}$$

Furthermore, there are also two branches within the hypothesis of the Gaussian heat source. Firstly, it is assumed that the heat source function changes with time. In the work of Joshi [44], they chose this kind of heat source to develop a finite element thermal model for the prediction of the shape of the crater, material removal rate, and tool wear rate. The heat source model is shown as Eq.3, where *Q(r)* is the heat flux, f_c is the energy distribution to the electrodes, *U* is the discharge voltage, *I* is the pulse current and t_{on} is the spark on time. Based on this heat source model, they developed a two-dimensional axisymmetric finite element thermal model for single spark EDM and finally achieved an accurate prediction of the EDM process response.

$$Q(r) = \frac{3.47878 * 10^5 f_c U I^{0.14}}{{t_{on}}^{0.88}} \exp\left(-4.5\left(\frac{t}{t_{on}}\right)^{0.88}\right) \quad \text{Eq.3}$$

In recent years, more and more researchers have adopted another type of Gaussian heat source model in which the heat source changes with the coordinate position. In other words, the heat decreases in a direction away from the center of the heat source. In the work of Shabgard [45], this kind of Gaussian heat source was chosen as Eq.4. In that, *Q(r)* is the heat flux, f_c is the energy distribution to the electrodes, *U* is the discharge voltage, *I* is the pulse current, R_p is the plasma channel radius, *r* is the distance to the center of heat source. With this, they built a FEM thermal model for researching the relation between radial distance and surface temperature and finally revealed that the energy absorption fraction of the electrode is variable and depends on the process settings.

$$Q(r) = \frac{4.57 f_c U I}{\pi {R_p}^2} \exp\left(-4.5\left(\frac{r^2}{{R_p}^2}\right)\right) \quad \text{Eq.4}$$

In another work by Kansal [46], they used the FEM to establish an axisymmetric two-dimensional model of powder hybrid electrical discharge machining to predict heat behavior and the mechanism of material removal in this process. The model includes several important aspects, such as temperature-sensitive material properties, size of heat source, percentage of heat distribution, pulse on time, pulse interval, etc. Among that, in terms of heat source selection, they also adopted the Gaussian heat source as Eq.4. After the thermal simulation, the Material Removal Rate (MRR) can be predicted

based on the temperature distribution. Further to verify the model, they compared the predicted theoretical MRR with the experimentally determined MRR value. There is a good agreement between the experimental and theoretical results.

Based on the above results, it can be concluded that the hypotheses of the heat source model and the conditions used by different authors present a lot of variations. Whereas now a considerable amount of experiments have proved that the Gaussian heat source model is the most realistic approach for the thermal simulation of EDM process research. Nowadays more and more researchers are adopting this kind of heat source assumption to do further study in EDM.

II.1.5 Radius of the plasma channel

Through the introduction of the previous two parts, it can be known that the plasma channel is where the heat source, which is responsible for distributing the most heat to the workpiece and wire, is generated (Figure 12). Besides the geometry of the heat source and the heat partition, as another crucial point, the size of the spark is also worth to be explored. It is well known that Plasma Channel Radius (R_p) is the decisive factor of spark size that determines the heated area on the surface of no matter workpiece or wire. For this radius, a lot of researchers have done various hypotheses. In this part, a review of this aspect of the process will be carried out.

Literature shows that the existing models for R_p almost can be divided into two different groups. The first hypothesis is that R_p is dependent on process parameters. Special attention deserves the model proposed by Ikai and Hashiguchi [47]. In their work, for each fixed current and pulse on time, numerous experiments were performed to measure the EDM'ed crater. Through the measurement of experiments, they found that the radius of the plasma channel depends on both the pulse on time and the discharge current. Hence in their work, this kind of R_p is adopted and the equation that they got is shown as Eq.5, where I is pulse current and t_{on} is pulse duration.

$$R_p = (2.04e-3) \cdot I^{0.43} \cdot {t_{on}}^{0.44} \qquad \text{Eq.5}$$

Based on this kind of formula of plasma channel radius, some researchers have done different research. In the work of Chen [48], they proposed a thermal model to study the wire electrode retreat and hysteresis when the servo feed rate does not match the achievable material removal rate in WEDM. In this thermal model, they adopted the radius formula above. At the same time with this model, they also predicted the achievable material removal rate and the best servo feed speed. In terms of the

maximum cutting speed and the expected achievable material removal rate, the average relative error between the simulation data and the experimental data is less than 13%. Furthermore, Shabgard [45] also adopted this equation in his work. They simulated the temperature distribution of the workpiece and the tool surface during a discharge in the electrical discharge machining process. This temperature profile is then used to calculate the size of the crater. Also, they established a thermal model to predict the achievable material removal rate and optimal servo feed speed.

From the works mentioned above in which the researchers adopted Eq.5, the validity of this formula can be confirmed to a certain extent. Apart from this kind of hypothesis, DiBitonto et al. [29] found that the size of the plasma channel is not constant, and grows over time. Therefore, they mathematically calculated the radius of the discharge channel in the form of an integral equation of the rectangular pulse. They presented their equation of plasma channel as Eq.6, where *t* is the time. At the same time, Erden [49] further integrates the equation. Finally, they proposed a formula of R_p as Eq.7, where the spark radius depends on the time. In that, *Q* is the discharge power, *t* is time, *m*, *n* and *K* are empirical constants. Furthermore, as shown in Eq.8, these constants are defined based on the coefficients L, *M* and *N* determined for different electrode material experiments. In addition, l is the discharge length.

$$R_p = 0.788 \cdot t^{0.74} \quad \text{Eq.6}$$

$$R_p = K \cdot Q^m \cdot t^n \quad \text{Eq.7}$$

$$K = \frac{L}{lM + 0.5N}, m = 0.5N, n = N \quad \text{Eq.8}$$

With the experimental data on the expansion of a high energy capacitor discharge in water Spur [50] plotted the change of plasma channel radius as Figure 18, based on this the plasma channel radius can be expressed as a function of the current rise time and the time during the discharge as Eq.9. In that, t_a is current rise time, *t* is time, *a*, *b, c* are three constants that can be obtained from Figure18. With this, they built a thermal model to simulate the crater on the workpiece and they also did the verification through the corresponding experiment. The result is plotted in Figure 19. Through contrast, they found that both the radius of the plasma channel and the radius of the crater increase linearly with time. Moreover, the absolute value and the slope of the curve of the plasma channel radius are smaller than the absolute value and the slope of the curve of the radius in the crater. The difference between the two curves is consistent with the theoretical prediction deviation between these two quantities. Therefore, they proved the validity of this thermal model.

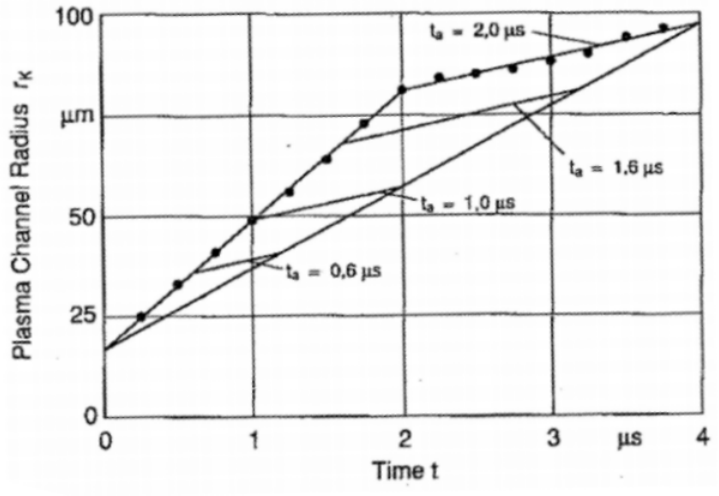

Figure 18. Radius of plasma channel versus time [50].

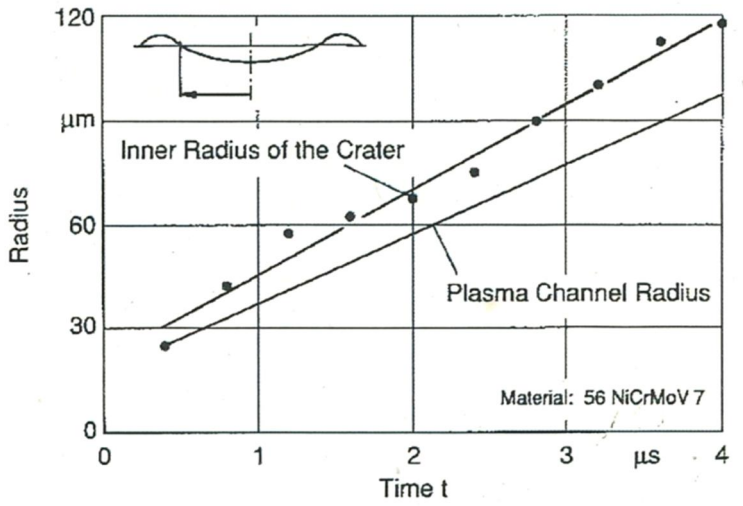

Figure 19. Contrasting between the inner radius of the crater and the plasma channel radius [50].

$$R_p(t_a,t) = \begin{cases} a+bt, 0 \le t \le t_a \\ R_p(t_a,t_a) + c(t-t_a), t_a \le t \le 2t_a \end{cases} \quad \text{Eq.9}$$

In the work of Natsu et al. [51], by observing the craters generated by discharges of different pulse duration, it was determined that the arc plasma diameter changed with time. In order to confirm the changing process of the plasma radius, they analyzed and experimentally studied the expansion of arc plasma and the formation of craters. By observing the arc plasma with a high-speed camera and measuring the plasma temperature after dielectric breakdown by spectroscopy, the shape and volume of the crater are calculated based on the thermal conductivity theory. Through heat conduction analysis, they proposed the expansion process of the plasma channel as

Figure 20. After that, they compared the size of the crater obtained from the simulation with the experimental results. They got the ratio of the depth to diameter from the simulation was 0.17 at 200 μs and that ratio was about 0.1 in the experimental result.

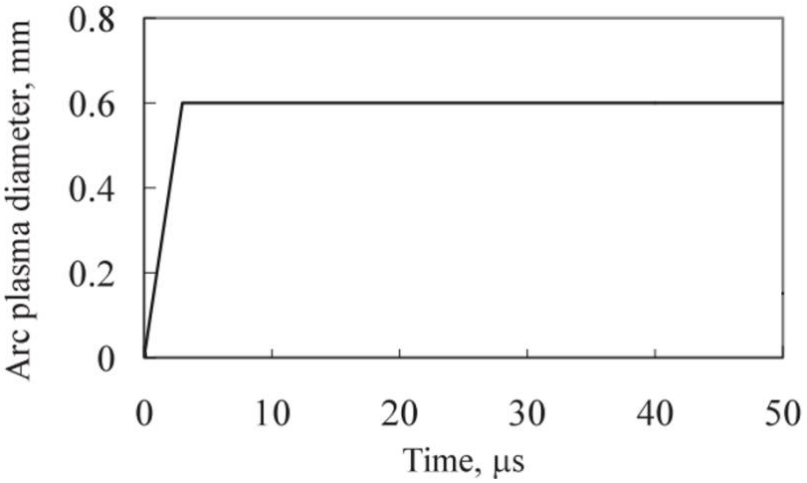

Figure 20. The expansion process of the plasma channel [51].

Furthermore, in the later work of Kojima et al. [25], with the conditions that the discharge current was 17A, the discharge duration was 80 μs, the gap width was 0.1 mm, and the electrode was copper, they also successfully measured the plasma diameter by optical emission spectroscopy to be 0.5mm, which is five times larger than the diameter of the crater. At the same time, they said that after the dielectric breakdown, the plasma expands within 2μs and remains constant during the discharge. In addition, with the observation, they also found that the radius of the plasma channel increases with the increase of the gap width. Based on this, they revealed the reason that when the gap width increases, the material removal rate decreases, and the surface roughness becomes smoother.

In addition, Pandey and Jilani [52] supposed that the plasma channel radius is a function of the average input power and the thermophysical properties of the workpiece material. They proposed that the constant surface temperature method can be used to estimate the radius of change of the heat source, and the model is given by Eq.10, where T_{ev} is boiling temperature, E_o is energy density and α is thermal diffusivity. But this expression is only valid for a few cases of selected electrode pairs and dielectrics. Finally as shown in Figure 21, through the calculation with Eq.6, Eq.9 and Eq.10 Banerjee [53] plotted the growth characteristic curve of the plasma radius channel.

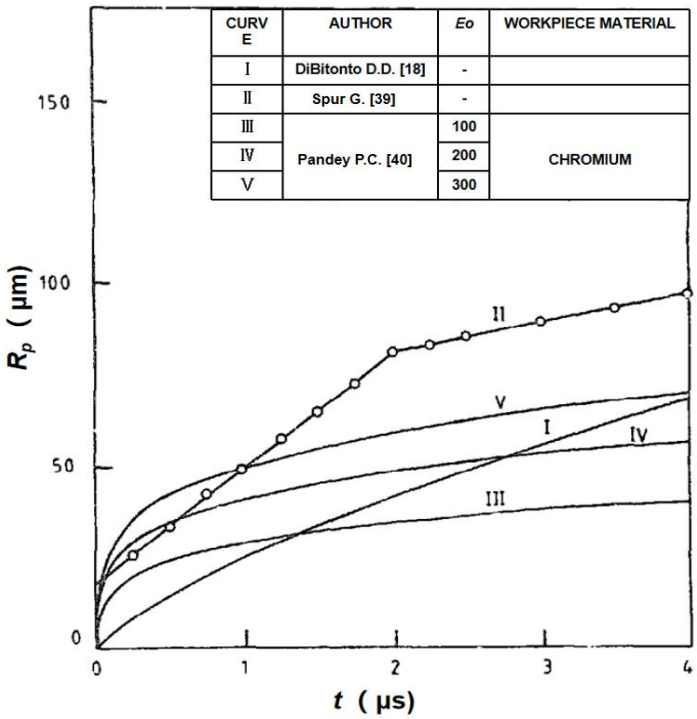

Figure 21. Summary of the relationship for variation of the plasma channel radius [53].

$$T_{ev} = \frac{E_o R_p}{K\pi^{0.5}} \tan^{-1}\left(\frac{4\alpha t}{{R_p}^2}\right)^{0.5} \quad \text{Eq.10}$$

According to the introduction of this section, it can be stated that these two kinds of hypotheses of plasma channel radius have a certain degree of validity since they have been successfully used by numerous researchers. Since there is no optimum plasma channel radius model yet, its selection must be further studied and verified in future work.

II.1.6 Plasma flushing efficiency

Plasma Flushing Efficiency (PFE) is also an important aspect of the EDM machining process which refers to the ratio of the actual volume of material removed during the spark discharge to the theoretical volume of melted material per pulse. In the work of Klocke [38], they proposed that this efficiency depends on the inlet fluid velocity. Simultaneously, this inlet fluid velocity depends on the initial constant flushing speed which is set by the EDM machine. On the other hand, it depends on the flushing jump movement of the electrodes that are present in the process of machining.

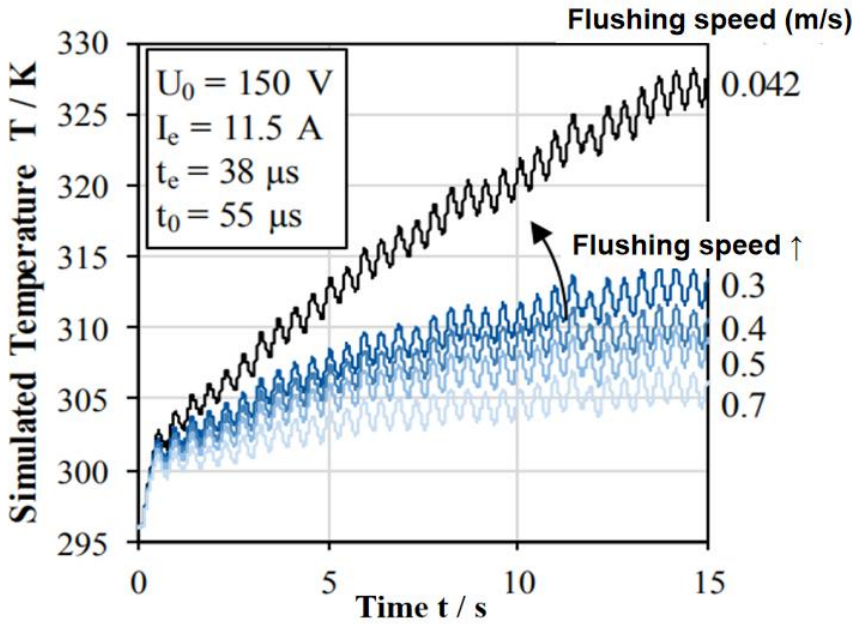

Figure 22. Effect of initial constant flushing speed on simulated temperature [38].

First, in order to verify the effect of the initial constant flushing speed (u_0), a series of simulations with different u_0 were implemented by Klocke [38]. It can be seen from Figure 22 that a higher flushing speed leads to a decrease in the temperature in the electrode. Then they also simulated the temperature changes under three different flushing jump movements. As the result shown in Figure 23, they found that the flushing jump movement has little effect on temperature in the simulation results. Especially at the beginning of the simulation, there is almost no obvious difference. Only at the end part of the simulation, did the different velocity amplitudes affect the temperature on the electrode. The temperature curve shows that although the average fluid velocity is the same, the higher amplitude of the flushing jump movement results in a lower temperature.

For further evaluating PFE, some researchers assumed the PFE to be 100% during the simulation process, and then the PFE is obtained by comparing the simulation results with the experimental data. Such as in the work of Shabgard [45], the value of PFE is described in Eq.11 and Eq.12. Where, $V_c(EXP)$ and $V_c(FEM)$ are respectively the crater volume gotten by experiment and simulation, M_1 and M_2 are the weight of electrodes before and after machining, N is the number of discharges and ρ is material density. Then they plotted out the correlation between PFE, pulse on time and pulse current as Figure 24. Based on this they obtained the equation of PFE on the workpiece and tool electrode shown in Eq.13 and Eq.14 respectively. In that, I is pulse current, t_{on} is the pulse on time. For verifying the validity of the model, they used the established model to predict the thickness of the recast layer and then contrasted it with the observation result. Finally, the prediction errors of the cathode and anode were

respectively 2.89% and 2.64%.

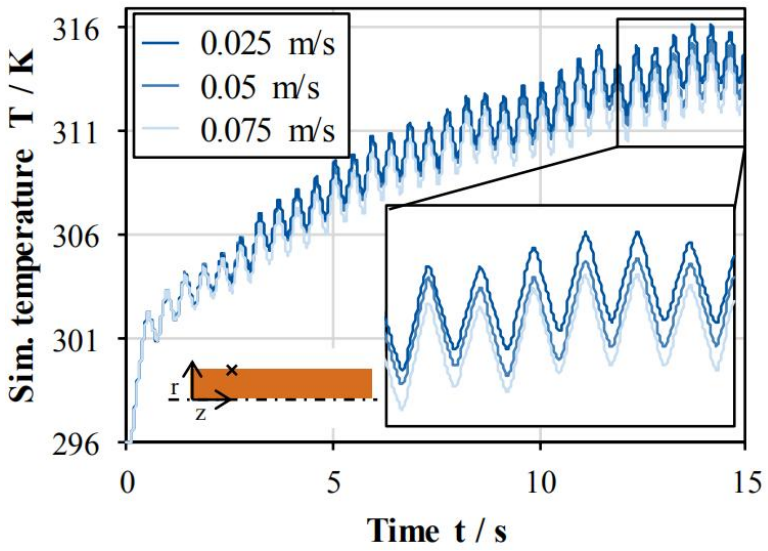

Figure 23. Effect of flushing jump movement on simulated temperature [38].

$$PFE = \frac{V_c(EXP)}{V_c(FEM)} \quad \text{Eq.11}$$

$$V_c(EXP) = \frac{(M_1 - M_2)}{N \cdot \rho} \quad \text{Eq.12}$$

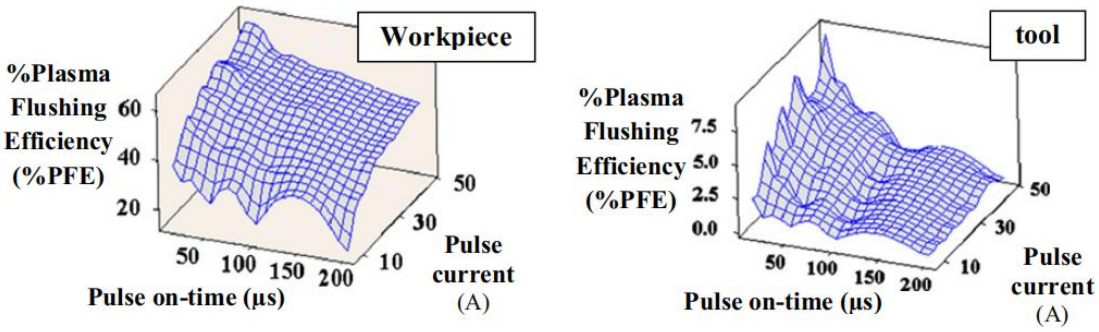

Figure 24. The correlation between PFE, pulse on time and pulse current [45].

$$PFE(Workpiece) = 149.197137 - 134.135686 \cdot I^{-0.1673} \cdot {t_{on}}^{0.5} \quad \text{Eq.13}$$

$$PFE(Tool) = 8.1055143 \cdot I^{0.631356} \cdot {t_{on}}^{-0.86781} \quad \text{Eq.14}$$

The revised literature in this section reveals the influence of plasma flushing efficiency in the EDM machining process. Hence, its application in EDM process simulation seems particularly important, and in terms of obtaining PFE value, it is also worth to further study in future work.

II.1.7 Latent heat

Aims to achieve the purpose of material removal in EDM, the tool electrode and the workpiece are repeatedly heated above the melting point and sometimes even above the evaporation point. And then they are both cooled in the dielectric. At the critical point for providing or extracting the change of substance state, although the temperature is not changed, a hidden form of energy exists, namely the latent heat.

Firstly in the work of DiBitonto et al. [29], they proposed a simple cathodic corrosion model that captured the main physical effects. In that model, they ignored the influence of latent heat. Finally, by contrasting the result of the simulation and experiment, they got a difference of 2%. Based on that they proposed that the influence of this factor in EDM on the material removal rate would not exceed 2%. With this conclusion in some early works, this factor was also not neglected in building simulation models, such as in the work of Banerjee et al. [53]. They pointed out that the latent heat value during the melting and evaporation process was not taken into account in the simulation process.

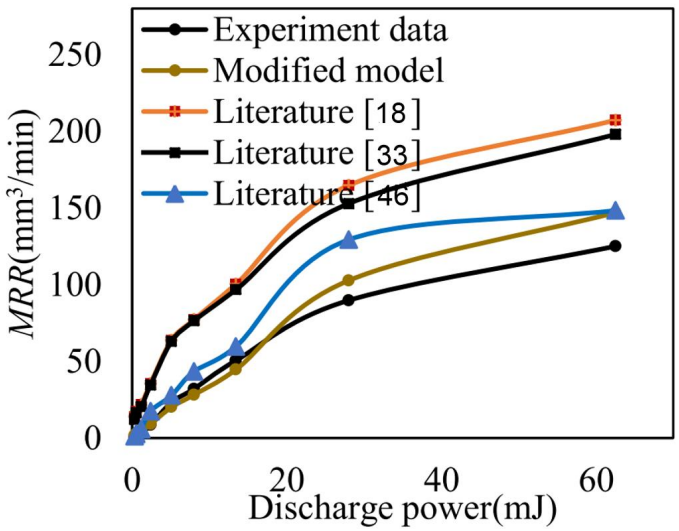

Figure 25. The relationship between discharge power and material removal rate in different thermal models [48].

Whereas, Kunieda et al. [18] indicated that with the advent of powerful computers and numerical methods, the relationship between the thermophysical properties of electrode materials and temperature and the latent heat of melting and vaporization should be taken into account in the establishment of thermal models. For further improving the simulation, more and more researchers believe that the influence of latent heat can make the model more realistic and reliable. In the work of Chen et al. [48], considering the latent heat of evaporation with Eq.15 and Eq.16, an improved

thermal model was established to obtain the size of the discharge pit during the single pulse discharge. In that, C_p is the specific heat capacity in the solid state, C_m is the equivalent specific heat of liquid, C_{ev} is the equivalent specific heat of gas, L_m is the latent heat of melting, L_{ev} is the latent heat of evaporation, T_m is the melting point, and T_{ev} is the boiling point. Finally, they compared their model with some others'. As shown in Figure 25, the improved thermal model with latent heat has high feasibility and accuracy.

$$C_m = C_p + \frac{L_m}{T_m - T_{ref}} \quad \text{Eq.15}$$

$$C_{ev} = C_m + \frac{L_{ev}}{T_{ev} - T_m} \quad \text{Eq.16}$$

Also in the work of Klocke [54], they studied the accuracy of several parameters that were proposed in some typical heat transfer models of single discharge. For doing that they rebuilt a thermal model and in that, the latent heat consumed at the melting point and evaporation point during the phase transition is also taken into account. On this basis, they successfully analyzed the influence of different modeling parameters on the obtained results.

The study of the importance of latent heat carried out in this section fully shows that latent heat is now being considered by more and more researchers in the EDM thermal model. To a certain extent, the accuracy and credibility of the thermal model are also improved. Therefore, the application of latent heat in the future thermal model is imperative.

II.1.8 Discharge delay time

In the EDM process, when an open circuit voltage is applied between the two electrodes, the discharge does not occur immediately but after a certain discharge delay time. The discharge delay time reflects the dielectric breakdown strength of the gap between the electrodes. As it is known that with the change of machining conditions in EDM, the delay time of discharge is also variable. In the work of Oßwald et al. [55], they distinguished the type of discharge by the discharge delay time. Through various experiments, they found that the distribution of different discharge types can be controlled by adding a controller and changing discharge current or conductivity during the machining process. On this basis, the processing efficiency and the processing quality can be improved.

Kunieda and Yakashima [56] proposed that the working gap width, the concentration

of debris particles, the surface area and the plasma deionization are important factors that affect the discharge delay time. At the same time, they proposed that since the discharge will occur in the area with the shortest discharge delay time, the location of the discharge can be predicted. Through their experiments, it was found that the discharge does not always occur in the narrowest part of the gap. And if the plasma formed by the first discharge is deionized during the discharge interval, the first discharge in the continuous pulse discharge will not affect the delay time of the second discharge or its discharge position.

Morimoto and Kunieda [57] finished several experiments for exploring the internal regularity of discharge delay time in SEDM. By changing the machining conditions as variables like electrode area, gap width, size and concentration of debris on the surface, respectively they calculated the probability of the spark occurring depending on the delay time in each condition. Based on this they plotted the Laue plot in Figure 26. Simultaneously, they further obtained an equation that can predict the average discharge delay time with the relative variables.

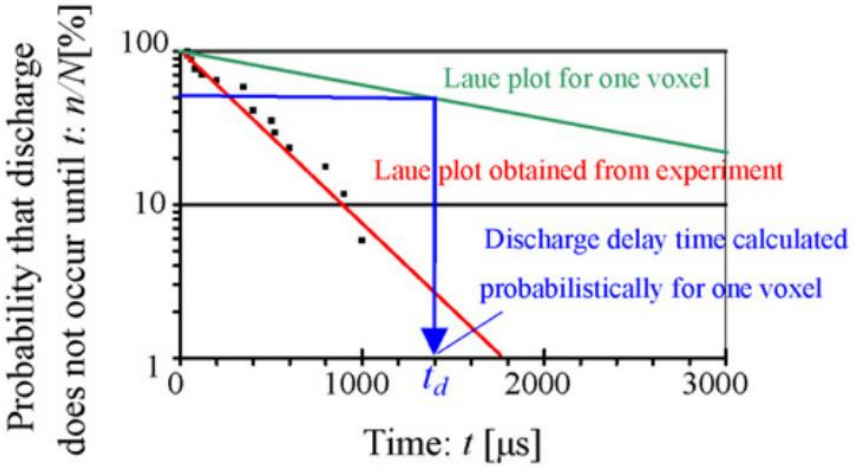

Figure 26. Laue plot [57].

Furthermore, in the work of Tang et al. [58], they studied and compared the changes in discharge delay time when copper, brass, and zinc were used as tool electrode materials. They found that different tool electrode materials do affect the discharge delay time. At the same time, they also studied the influence of the debris particles in the gap of two electrodes on the discharge delay time. The result shows that the impact of debris particles on the discharge delay time is negligible.

Morimoto and Kunieda [59] studied the influence of debris concentration and processing area on discharge delay time in the SEDM process. Through experiments,

they found that at the same concentration of debris particles, the discharge delay time decreases with the increase of the machining area, which means that the discharge probability is proportional to the machining area. At the same time, they also found that the debris formed in the gap during processing has a significant effect on shortening the discharge delay time and can increase the material removal rate to a certain extent.

Araie et al. [60] studied the influence of electrode surface roughness on the discharge delay time of single pulse discharge. As the experiment results are shown in Figure 27, they found that the discharge delay time is affected by the surface profile of the electrode, and the delay time of a single pulse discharge will be shortened when the electrode surface is rough. Another aspect studied is that the surface roughness of the workpiece has a more significant impact on the discharge delay time than the tool electrode. When the surface roughness of the workpiece is greater than that of the tool electrode, the discharge delay time will be shorter.

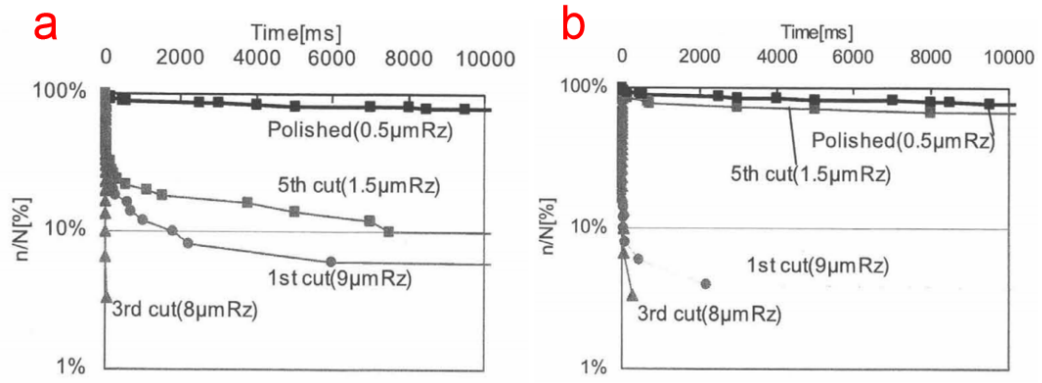

Figure 27. Change of discharge delay time with different surface roughness: (a) Tool electrode; (b) Workpiece [60].

After this revision work, it can be concluded that many researchers have completed many studies on the discharge delay time in the field of SEDM and a certain understanding of this problem has already been gained. For WEDM, there are still few studies in this area. Therefore, more experiments and simulation work in terms of WEDM should be carried out to get a deeper understanding.

II.2. Nature of debris in EDM

Since most of the material removal in the EDM is caused by the boiling of the overheated melt in the crater, as shown in Figure 28, after the discharge is terminated, the bubble will break and the liquid jet that penetrates the bubble from all directions

will hit the crater and expel molten metal. Based on that, debris particles are generated by the recondensation of that molten metal by the dielectric liquid flushing during the discharge. In recent years, many researchers have conducted research on the debris produced in the EDM process to understand its influence on the machining process and results.

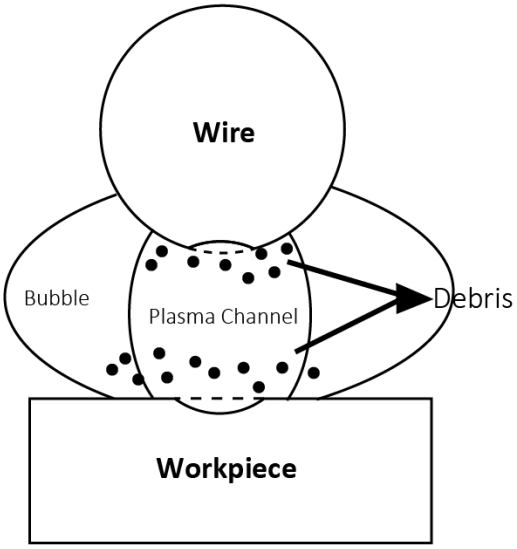

Figure 28. The production of debris.

II.2.1 Observation and size distribution of debris

In order to understand the movement of debris, Kunieda and Yanatori [61] used an image conversion camera to observe the SEDM process (Figure 29). They found that the debris particle in contact with the tool electrode is negatively charged and accelerates toward the workpiece. When the debris particle collides with the workpiece, the negative charge is released, and the particles are positively charged and accelerate to move toward the tool electrode. As to realize a kind of debris-reciprocating movement between the two electrodes. In addition, they proposed that the number of particles in the gap can be estimated by measuring the leakage current during the discharge delay time.

Debris size distribution and location during single discharge SEDM were studied by Yoshida et al. [19]. They found that debris particles tend to concentrate at the boundaries of the discharge bubble. In his work, the debris generation in air and liquid were studied respectively (Figure 30). The debris generated in the liquid is mainly distributed at the boundary of the bubbles formed due to the evaporation and dissociation, while in the EDM gap, the distribution of the debris in the radial direction is affected by the number of bubbles generated. When the debris forms in the air, it is distributed widely in the radial direction, and as the radial distance from the center of the discharge crater increases, the debris density decreases. In addition, the debris

generated in the air is usually smaller and larger than that found in liquids and when the discharge takes place in liquid and low values of on-time are used about 80% of the particles have a diameter of around 30µm.

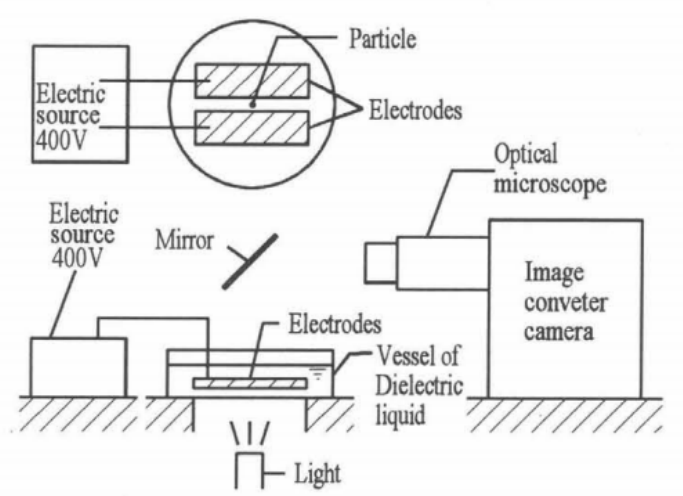

Figure 29. Observation system with image conversion camera [61].

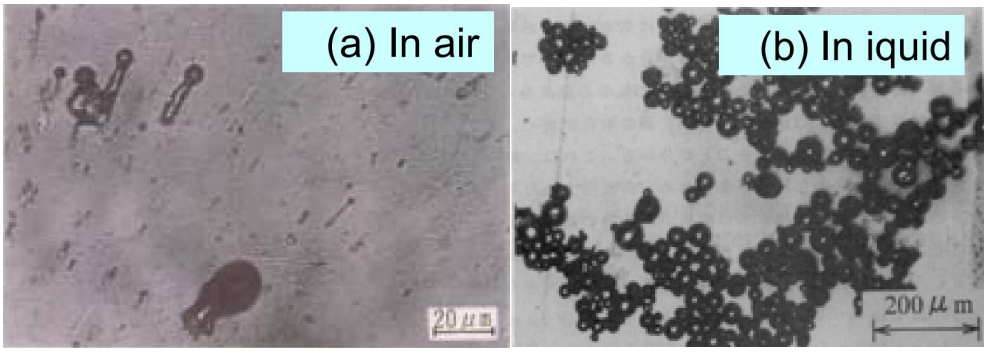

Figure 30. Shapes of debris generated in air and liquid [19].

Murray et al. [62] revealed that sub-micron and even nanometric or probably sub-nanometric particles result from the SEDM removal process. Si and TiC electrodes were used for the anode and 304 stainless steel for the cathode. They used scanning electron microscopy (SEM) to classify particles larger than 0.2µm and found that the largest particles were below 10µm. Then, they used Transmission Electron Microscopy (TEM) analysis to resolve smaller-scale debris. It was found that there is a matrix of debris made up of extremely small particles (1nm or even lower) surrounding micron-scale debris.

Oßwald et al. [63] studied the characteristics of debris particles produced during the SEDM process. They used different processing parameters to produce particles with different size distributions. Through dynamic image analysis, they found that SEDM

can produce particles with high sphericity and it shows a low rate of internal powder porosity. They also obtained the debris size distribution as shown in Figure 31, which shows that most of the debris is between 10µm and 100µm in diameter. In addition, they proposed that the size distribution can be controlled by EDM parameters.

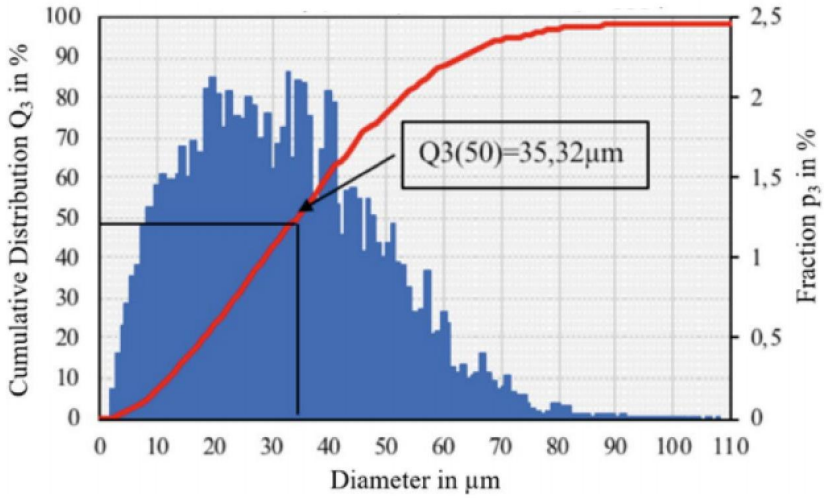

Figure 31. Size distribution of debris [63].

From the consulted bibliography, a preliminary understanding of debris observation and distribution in EDM can be obtained. Existing works in this field are still not enough to completely understand the effect of debris on the EDM process. More studies of debris including but not limited to the observation in a range of nanometers and the study of debris composition are still need to be researched.

II.2.2 Simulation of debris in the EDM process

Due to the large flow rate and the small processing gap width, it is difficult to study the movement of debris during the EDM process through direct observation. To further understand the debris movement in the process of EDM and find a method to avoid its negative influence as much as possible, in recent years, many researchers have begun to work on the simulations of debris in the EDM process.

Liu et al [64] used Fluent software to simulate the distribution and movement of debris and the effect of ultrasonic vibration assistance in the EDM process. They simulated the movement and distribution of debris in processing with different vibration frequencies and different amplitudes. Through the results, they found that ultrasonic vibration assistance can speed up the circulation of the dielectric liquid and increase the flow of the working fluid flowing through the gap between the wire and the workpiece, thereby accelerating the removal of debris and enhancing the stability and

efficiency of the machining process.

Zhang et al. [65] used a combination of simulation analysis and experimental research to study the movement of debris between electrodes during the EDM process. Through the Fluent software simulation and corresponding experiments, they found that the dielectric liquid has enough pressure to remove debris during the shallow machining process. However, as the tool electrode goes deeper into the workpiece, higher flushing pressure is required to achieve the purpose of removing debris.

In order to study the mechanism of debris movement during continuous pulse discharge, Wang and Han [66] proposed a three-dimensional model of the flow field in the machining EDM gap which is shown in Figure 32 and they also conducted experimental observations. Eventually, they found that most of the debris moved outward following the bubbles in the working gap. In addition, they found that as the discharge current and pulse time increase, the bubble expands stronger and makes it easier for debris to be removed.

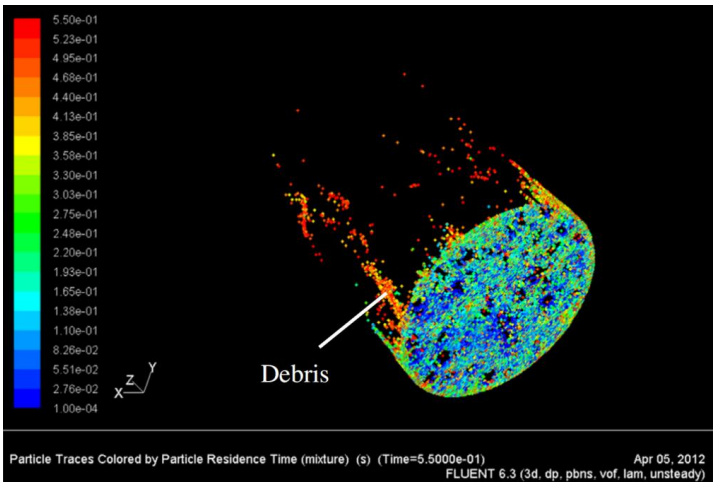

Figure 32. Three-dimensional model of the flow field in the machining EDM gap [66].

Cetin et al. [67] used a computational fluid dynamics (CFD) simulation program to analyze the dielectric fluid flow and debris distribution in the EDM machining gap. They proposed that the simulation model can be improved by considering the distribution of different numbers and sizes of debris. At the same time, they examined and compared the interaction between the fluid flow between the electrodes and the movement of debris. Finally, they found that the concentration of debris in the area where the eddy current is generated in the machining gap will increase, which will lead to the occurrence of secondary discharge. Through their simulation model results, the mechanism of debris movement can be better understood, which also helps to optimize the accuracy and stability of the EDM process.

Tanjilul et al. [68] proposed a CFD model to study various factors affecting the removal of debris from the machining gap. Based on CFD simulation and experimental results, they found that the processing current affects the size of the debris particles, and the size of the debris increases with the increase of the processing current. They also proposed that the optimal flushing pressure can be calculated by introducing the experimentally measured debris data into the CFD model, thereby achieving the effect of improving the EDM quality.

From the review presented in this section, it can be stated that more and more researchers have simulated the movement of debris in the machining gap. This not only helps to better understand the movement principle and distribution of the debris but also can be useful for finding better processing parameters through the analysis of the debris. Therefore, more relevant research is worthy of further exploration to achieve the purpose of improving the quality, efficiency and accuracy of the EDM process.

II.3. Wire breakage in WEDM

II.3.1 Wires for EDM

It is now generally believed that the electrode wire can greatly affect the performance of the wire-cutting machine tool. The choice of wire used to be copper or brass. Then, in order to meet the processing needs, various high-performance wire electrodes have been developed, such as galvanizing, diffusion annealing, coated steel core wire, etc.

Objective	Wire selection
To Increase Cutting Speed	Zinc-coated copper/Zinc coated brass
To Cut Steep Tapers	Soft brass/Zinc coated soft brass/Diffusion annealed brass
To Cut Thicker Workpieces	Diffusion annealed copper/Diffusion annealed brass/Coated steel core
To Increase Straightness	Al or Mg brass alloy/Moly or tungsten wire/Coated steel core
To Increase Accuracy	Al or Mg brass alloy/Coated steel core

Table 1. Wire selection for different machining objectives [69].

Novotec [69] proposed that the general wire selection needs to consider the following characteristics. The first aspect is the tensile strength, which is based on the material's ability to resist stretching and breaking and the maximum load-bearing capacity of the

material. High-strength wires can provide better edge straightness and help improve the accuracy of parts. The second one is wire toughness. The wire with good toughness is more resistant to the influence of the dynamic environment of the spark gap. Then it is the conductivity. In WEDM, with the higher conductivity of the wire greater power can be delivered to the workpiece. At the same time, the cutting speed can be accelerated. The last aspect is vaporization temperature. When the surface of the wire evaporates during processing, it quickly turns into gas, thereby helping to flush and enhancing machining efficiency. Finally, as shown in Table 1, they proposed some wire selections for different machining objectives.

In order to understand the influence of different wire materials on the WEDM process, Kumar et al. [70] chose brass wire, galvanized wire, and high-cutting speed wire respectively to study the cutting performance parameters of AISI D3 steel such as cutting speed, wire wear and surface roughness. With the corresponding material of the wire, they finished several experiments with the same machining parameter. As the result, they found that with brass wire the cutting speed is the lowest but in terms of surface roughness and wire wear it shows the best performance.

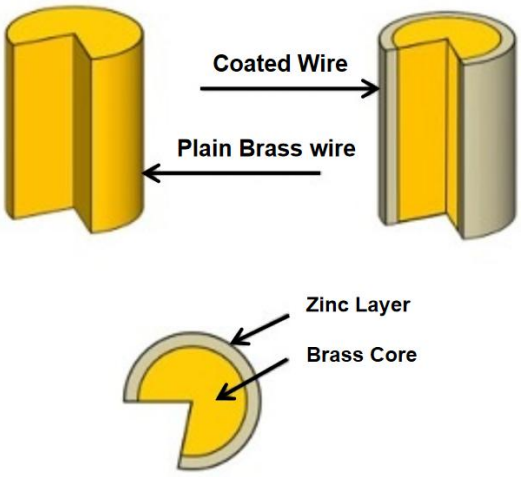

Figure 33. Plain brass wire and coated brass wire [71].

In addition, Dave [71] has done a comparison between the coated brass wire and plain brass wire (Figure 33). He found that the coated wire has higher conductivity and this coating can protect the inner core to achieve faster material removal rate. By comparing the two kinds of wires by processing with the same parameters, it is found that with the use of coated wires the wire breakage occurring times become fewer. Simultaneously, it was proposed that although the cutting speed of the coated wire is 20-30% faster than that of the plain brass wire, the use of the coated wire will incur higher costs. Therefore, when processing time is not crucial and good flushing conditions can be obtained, plain brass wire is a more economical choice.

Therefore, it can be concluded that wire plays a crucial role in WEDM. This aspect of the process can affect the machining efficiency and machining quality. The choice of different wires can solve different processing problems. Although brass and copper-based wire are commonly used in WEDM, more kinds of wire are still worthy of being further studied and applied in future machining.

II.3.2 Experimental studies to explain the causes of wire breakage

Wire breakage during WEDM is one of the worst cases (Figure 34), which greatly affects the machining accuracy and the quality of the parts produced. Therefore, wire breakage is a critical topic in WEDM Industry. For instance, in current industrial practice, cutting in non-sealed conditions during roughing cuts may result in wire breakage. This is a common industrial situation when cutting stepped parts, or when due to part geometry accessibility is limited. As technology application progresses, the need for a satisfactory scientific explanation of underlying phenomena has become even more evident.

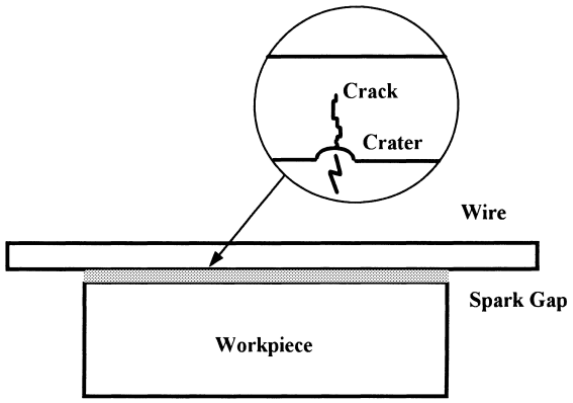

Figure 34. Wire breakage in WEDM process [72].

In fact, the reliability of WEDM machines in the early years depended on the possibility of wire breakage, which limited machine productivity. The first researchers of the process found that wire breakage was in some way related to excessive temperatures. Kinoshita [73] observed that the pulse frequency of the gap voltage rose rapidly and lasted about 5-40ms before wire breakage. So they developed a monitoring system to turn off the pulse generator and servo system. This method can effectively prevent the wire from breaking, but this system also has a disadvantage, that is, it will affect the processing efficiency. Besides that, a US Patent by Itoh [74] introduced a new invention aiming at monitoring the location of discharges occurring within the gap between a wire electrode and workpiece, confirming thus since the early days the importance of discharge concentration on wire breakage.

Banerjee et al. [75] proposed an expression for the heat source generated by a single

discharge, in which the plasma channel radius depends on part material properties and the average input power. In a later work, Banerjee et al. [53] attempted to predict the wear of the wire by using the finite difference method to calculate temperature fields generated by a single discharge. They proposed using the recrystallization isotherm (at 733.15K for the brass wire) as a measure of the minimum possible "load-bearing area" of the wire. Interesting results from the sensitivity analysis of the boundary conditions of the problem can be found in this work.

Luo [72] studied the phenomenon of sudden and random wire breakage from the point of view of fracture mechanics, including the influence of spark pressure and wire deformation. However, the development of advanced digital discharge generators and efficient process monitoring has largely reduced the possibility of random wire breakage when cutting under sealed flushing conditions. Certainly, under controlled dielectric flushing and following machine manufacturer recommendations, the possibility of wire breakage becomes nearly zero. In the same paper, it is recognized again that insufficient flushing may lead to arcing and excessive heat concentration on the wire. At the current state of the technology, strong interest is focused on wire breakage when cutting in non-sealed conditions in rough cuts. This is a common industrial situation when cutting stepped parts, or when due to part geometry accessibility is limited. In those cases, dielectric nozzles cannot be set at a very close distance (about 0.1mm in conventional machines) from workpieces' upper and lower surfaces, flushing conditions deteriorate and debris from previous discharges accumulate within the working gap. In the work of Tosun and Cogun [76], they successfully performed the observation of wire with presence of craters (Figure 35). They approached the problem of wire wear using regression analysis to find statistical relations between the wire wear ratio and process parameters. An interesting conclusion is that a high wear ratio is related to low values of flushing pressure, confirming thus the negative effect of debris and local concentration of discharges.

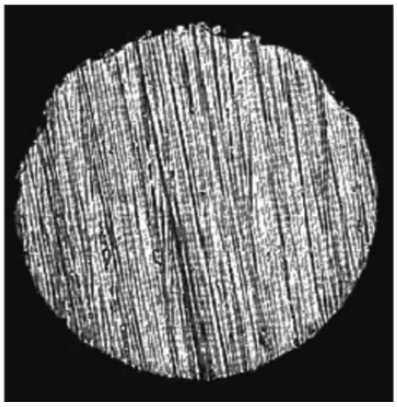

Figure 35. Wire with craters [76].

Following in the research of Saha et al. [77], they confirmed the existence of internal thermal stresses resulting from non-uniform heating of the wire. Even though the stress level predicted by the model is well below the yield stress of the wire, and therefore it cannot fully explain wire breakage. Fedorov et al. [78] confirmed this result in a recent paper. By considering the tensile force imposed by the machine, the thermal stresses derived from the non-even temperature distribution on the wire and accounting for the amorphization of the wire surface, they concluded that actual stresses on the wire during normal processing are about 50% of the actual tensile strength of the wire. This work also sohowed that the Rehbinder effect combined with wire damage and process loads do not significantly affect wire breakage.

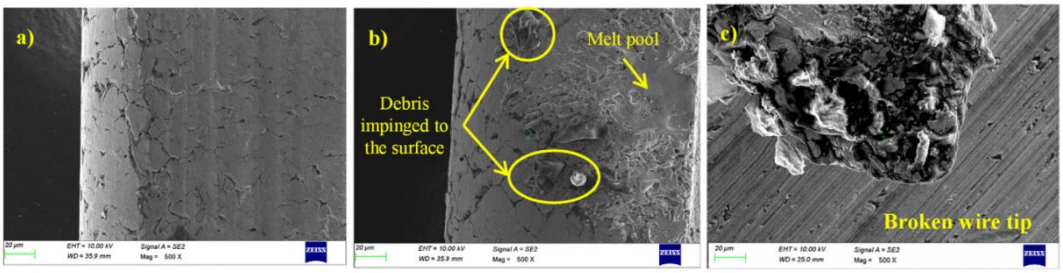

Figure 36. Wire surface observation by SEM: (a) Under low average gap voltage; (b) Under medium average gap voltage; (c) Broken wire under high average gap voltage [79].

In order to find the relationship between the average gap voltage change and the wire breakage in WEDM, Abhilash and Chakradhar [79] performed a lot of experiments using the average gap voltage change as an index. They found that if the value of the average gap voltage exceeds a certain threshold limit, the number of occurrences of wire breakage will increase and affect processing efficiency. Based on this finding, to predict the disconnection, they used an adaptive neuro-fuzzy inference system to model the average gap voltage. And experiments confirmed the reliability of their model. In addition, they also conducted microstructure analysis with SEM (Figure 36) and further revealed the influence of average gap voltage on wire wear and component quality. They found that a higher average gap voltage value would lead to more frequent wire breakage and reduce machining quality.

Das and Joshi [80] measured and analyzed the erosion of the Ti-6Al-4V alloy wire after cutting at different input discharge voltages, discharge currents, pulse duration, pulse interval and feed speed. They used SEM to analyze the wire surface damage and used image processing technology to estimate the wire surface quality index of the allowable limit of wire surface erosion. They concluded that during processing, the wire diameter initially increased on one side compared to the original diameter, and then, with the wire moving forward in the feed direction, the diameter of the wire

gradually became smaller. At the same time, in addition to the corrosion of the wire, they also found that the increase in the temperature of the wire during the processing caused the strength to decrease, which is also an important cause of wire breakage.

According to the revised bibliography, it is clear that wire breakage is still a hot topic today. A lot of researchers focused on this popular problem in WEDM and did a huge number of experiments to intend to further understand and figure out its cause. Although now the existing work can explain to a certain extent the internal reasons for wire breakage, it is still not enough to realize the objective of avoiding that in the process of machining. So there is still more work that needs to be done.

II.3.3 Discharge location in WEDM

Based on the previous section, it can be stated that the temperature distribution of wire has a great influence on wire breakage. Since the concentration of discharge will cause the accumulation and concentration of heat, it is considered to be an important cause of wire breakage. Therefore, for decreasing the frequency of wire breakage and improving machining quality, research on the discharge position becomes very important. In the early 1980s, a US Patent by Itoh [74] introduced a new invention aimed at monitoring the location of discharges occurring within the gap between a wire electrode and workpiece, thus providing early confirmation of the importance of discharge concentration in wire breakage (Figure 37).

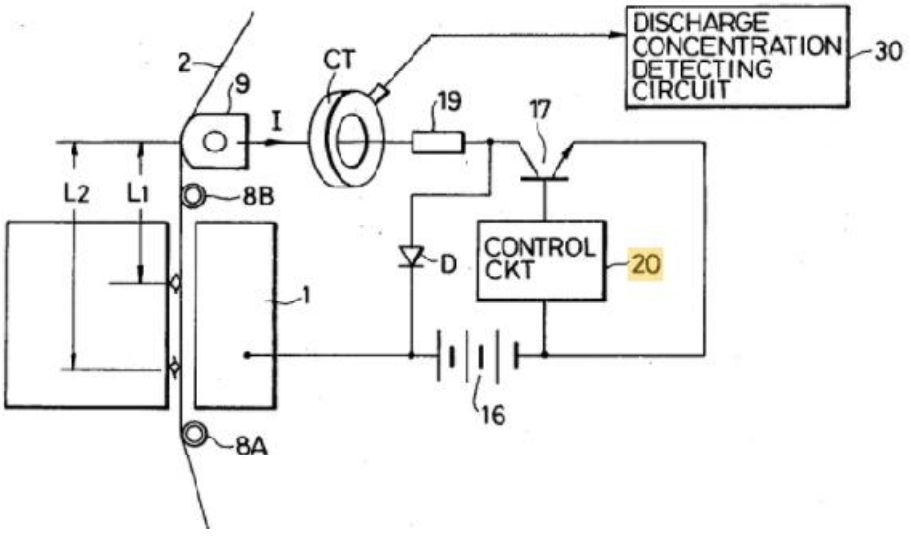

Figure 37. Discharge concentration detecting circuit [74].

In the work of Kunieda et al. [81], they proposed that with the change of spark position, the part of wire included in the upper circuit and lower circuit respectively will also

change. Since the wire is seen as the resistance in the circuit, it means that the current value is distinct depending on the spark position. Based on this theory, Han et al. [82] used the probability method to simulate the discharge position in the WEDM process. The simulation results were also verified by comparing the processed shape obtained by simulation with that obtained by actual processing. At the same time, they found that compared to constant feed rate control, adaptive servo feed control is more likely to cause fringes on the machined surface.

Although the fundamentals of discharge location were known, it has not been until recent years that the technology has been fully developed. Locating and tracking the discharge position during the WEDM process has become an important research direction again for many researchers and strives to be applied to actual industrial processing to achieve the improvement of machining efficiency and quality. Boccadoro et al. [15] created a model of wire shape and wear and they successfully located the position of discharges during the WEDM process. As shown in Figure 38, through the current changes in the upper and lower parts of the circuit they realize real-time monitoring of discharge position. With the detection of this model, the feed rate of the wire can be adjusted during the machining process and the complete process of the machining process can be tracked to obtain the machining contour. At the same time, the cause of the final processing defects of the workpiece can be found and it is helpful to improve the traceability of the WEDM process.

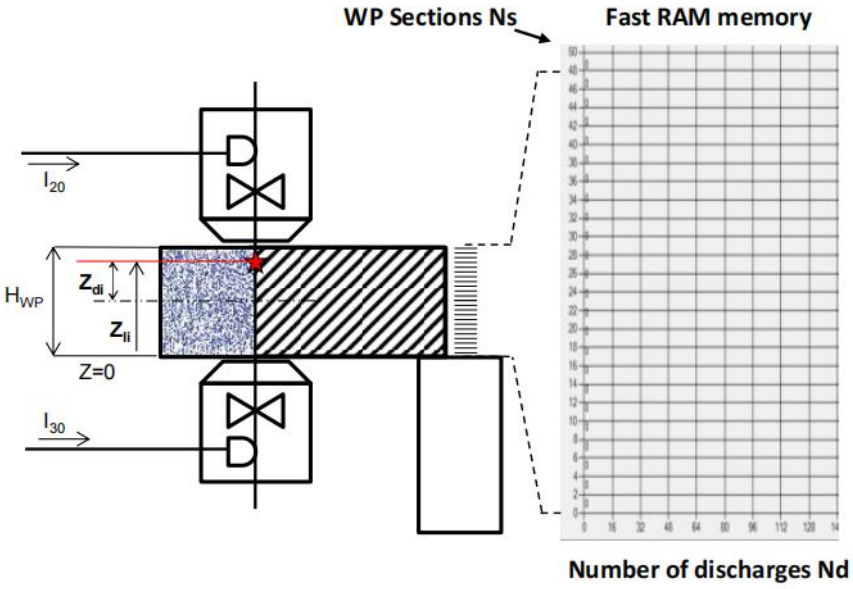

Figure 38. Schematic diagram of the discharge location positioning system [15].

In addition, Okada et al [83] indicated that when the workpiece is very thin, the current method is difficult to accurately evaluate the spark position distribution. As shown in

Figure 39, they proposed a method to measure the location of discharges by analyzing images recorded by high-speed cameras. Then they studied the influence of servo voltage, pulse interval time and wire feed speed on discharge distribution. Finally, they found that when the servo voltage is high, the pulse interval time is long, and the wire speed is low, the spark distribution becomes uniform. The conclusion is that this method has a great effect on evaluating the distribution of discharge positions.

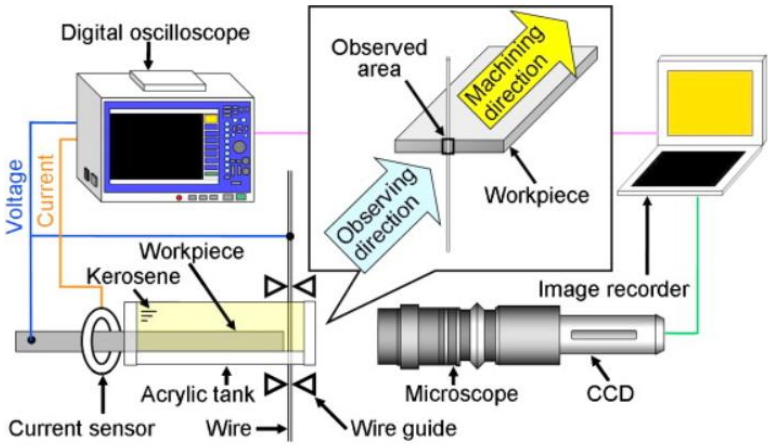

Figure 39. High-speed observation system [83].

In addition, Chen et al. [84] proposed a new high-speed observation system to evaluate the spark position during continuous discharge. The discharge sparks passed through the heat-resistant glass, the filter, the focusing lens, and finally, the image was collected by the digital high-speed camera. They used a series of image processing methods and centroid methods to obtain the discharge position and found that most discharge sparks are in the middle area of the workpiece, followed by the lower and upper areas. At the same time, they also explained the relationship between discharge distribution and machining quality and optimized the process parameters based on the uniform discharge position. Finally, they achieved a 32.6% reduction in average surface roughness while maintaining machining efficiency.

In the work by Han et al. [85], they clarified that the discharge position can be controlled by the principle of local superposition of high electric fields. Based on this, to improve the controllability of the discharge position, they proposed that the local high electric field can be improved by increasing the superimposed voltage, and it can also be superimposed successively to increase the discharge probability. Through experiments, they succeeded in the uniform distribution of discharge positions on the surface of the workpiece, which can improve the quality of the machined surface.

As a conclusion for this section, it can be seen that due to the importance of uniform

discharge on the processed surface in reducing wire breakage, improving processing quality and increasing processing efficiency, the research on discharge location has been paid a lot of attention by researchers in recent years. At the same time, it is more than research, and the application of the monitoring of the discharge position in the WEDM field has become more and more popular in the industry. However, in actual industrial applications, the accuracy and real-time monitoring are still worth studying and need to be improved.

II.4. Numerical model in EDM

As the essence of cutting is the superposition of craters produced by discharges, analysis of craters is a crucial approach to understanding the process of material removal. Now combining modeling and simulation with realistic experiments is a sound approach to getting a better understanding of craters. Theoretical models of the WEDM process must assume important simplifications not only because of the complex phenomena involved but also because of the difficulty in setting realistic boundary conditions. The main advantage of numerical methods is that they allow the modeling of complex geometries, variable boundary conditions and variable material properties. Therefore, fundamental studies are very necessary for better-defining boundary conditions and reducing modeling uncertainties.

II.4.1. Numerical model establishment

The discharge material erosion heat model is established based on the classic Fourier heat conduction model which is shown in Eq.17 [42]. In that, ρ is the density of the workpiece material, C is the specific heat capacity, and λ is the thermal conductivity. This equation represents the most general case. The solution of the differential equation requires the definition of the initial conditions and boundary conditions of the problem. The initial conditions will be given by the temperature distribution at the initial moment, and the boundary conditions will reflect the possible symmetry, isolation, convection with the surrounding medium, etc. Among all these boundary conditions, the most important for EDM process modeling is the heat source that represents the energy input related to the spark.

$$\rho C_p \frac{\partial T}{\partial t} = \frac{1}{r}\frac{\partial}{\partial r}(\lambda r \frac{\partial T}{\partial r}) + \frac{\partial}{\partial z}(\lambda \frac{\partial T}{\partial z}) \quad \text{Eq.17}$$

The schematic diagram of the H-dimensional axis-symmetric single-pulse heat conduction model is shown in Figure 40 [48]. Assuming that the surrounding environment is maintained at 20°C, the boundary conditions are: (a) Surface 1: Absorb

the discharge energy in the pulse during the pulse on time and release the heat energy through thermal conduction with the dielectric during the pulse interval. (b) Surface 2: It loses heat energy by conducting heat with the dielectric. (c) Surfaces 3 and 4: Due to symmetry, they are heat-insulating surfaces. (d) Surface 5: It is an insulating surface.

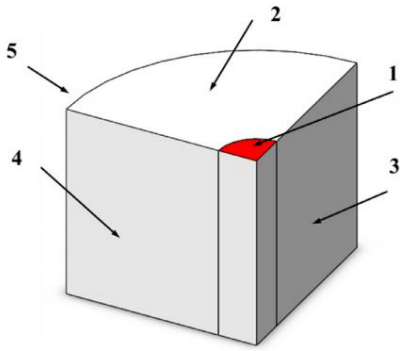

Figure 40. Axis-symmetric configuration on single discharge process [48].

For the multi-pulse discharge process, the thermal model is also established based on the Fourier heat conduction equation, and the plane-symmetric structure of the model is shown in Figure 41. The boundary conditions are: (a) Surface 1: Absorb the heat energy in the pulse during the pulse on time and release the heat energy through the heat conduction with the dielectric during the pulse interval. (b) Surface 2: It spreads thermal energy to the outside through thermal conduction with the dielectric. (c) Surfaces 3 and 5 are heat-insulating. (d) Surface 4: Due to its symmetry, it is also an insulating surface.

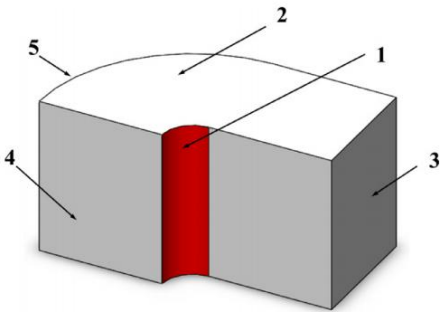

Figure 41. Axis-symmetric configuration on multi-discharge process [48].

Nowadays, the most used numerical method is FEM, which is also based on the geometric discretization to be studied. For doing research work, different commercial finite element software tools (such as ABAQUS, ANSYS or DEFORM) are adopted. In addition, the other crucial elements in the establishment of a numerical model in EDM such as the distribution of discharge energy, heat source model, the radius of the plasma channel, plasma flushing efficiency, and latent heat have already been introduced in Section II.1.

II.4.2. Application of numerical model

The application of numerical models is becoming more and more popular in the study of the crater in EDM. The main advantage of numerical methods is that they allow the modeling of complex geometries and variable profile conditions as well as variable material properties. Nowadays, this method is widely used in various fields of EDM to study the machining process.

II.4.2.1. Numerical model application in SEDM

In recent years, there are a lot of research works on SEDM that were finished based on numerical application. Das et al. [86] used the FEM to establish a numerical model to simulate the influence of a single spark. The model used process parameters such as power input, pulse duration, etc. In addition, they verified the model with experimental data. Finally, based on this model, they used the solver of DEFORM to solve the heat transfer problem to successfully predicted the temperature distribution, material transformation, and residual stress in EDM. The result is shown in Figure 42, the EDM crater shape was obtained.

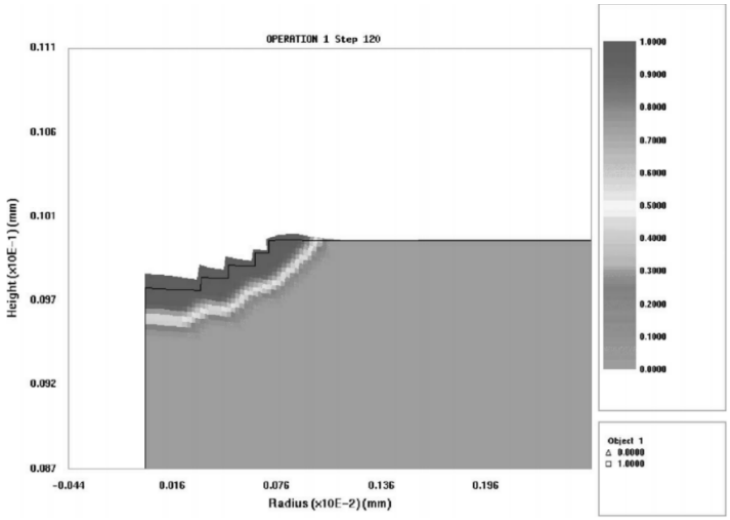

Figure 42. EDM crater simulation with a numerical model [86].

As shown in Figure 43 (a), Liu et al. [87] also built a FEM numerical model of single discharge. More importantly, they successfully implemented a model to solve the random discharge phenomenon in ABAQUS, they simulated the induced temperature field generated by a large number of electrical discharges in NiTi alloy workpieces which is shown in Figure 43 (b). Among them, the discharge position is determined by implementing random theory in the finite element model. As the result, they successfully predicted thermal damage by this novel numerical model and proved that

the proposed model considering the random discharge phenomenon is an effective method.

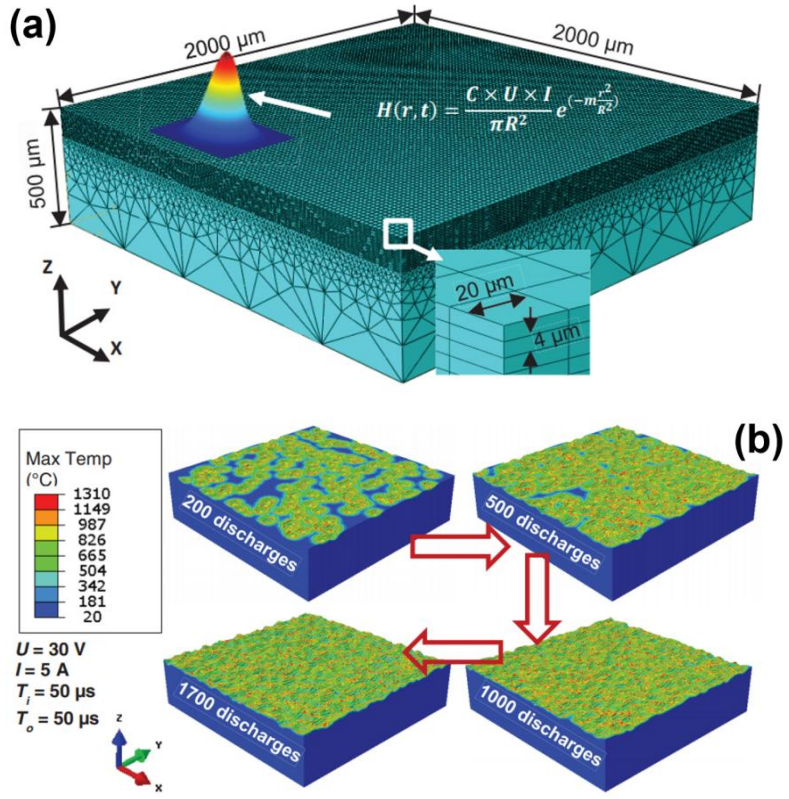

Figure 43. (a) 3D FEM numerical simulation of single discharge; (b) Multi-discharges numerical model [87].

Izquierdo et al. [32] proposed to use the method of finite difference scheme to numerically calculate the temperature field inside the workpiece produced by the superposition of multiple discharges. The discharge characteristics (heat transferred to the workpiece, diameter of the discharge channel and material removal efficiency) for a given operation can be estimated by inverse identification based on the results of the numerical model. And the model was verified by an industrial EDM test, showing that their proposed model can effectively predict the material removal rate and surface roughness with an error of less than 6%.

After that, Tlili et al. [88] improved the numerical model based on the finite difference method with Ansys. The model takes into account the growth of the plasma channel and the instantaneous removal of material during the entire discharge process. It can be used to evaluate the effectiveness of the model based on the material removal rate and the crater shape. For verifying the model, they used tool steel AISI D2 to conduct related experiments. As shown in Figure 44, they compared the material removal rate (MRR) obtained in the experiment with the simulation data, and the results proved the validity of the numerical model.

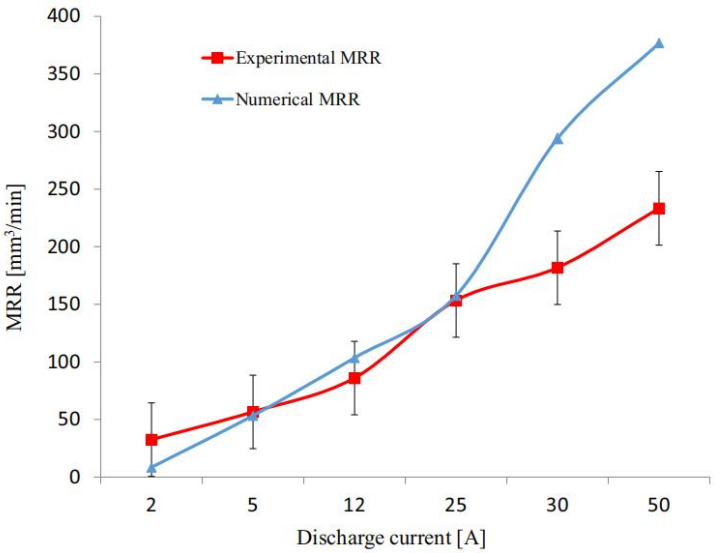

Figure 44. Comparison of results between experimental and simulation data [88].

Shabgard et al. [45] used ABAQUS to simulate the temperature distribution of the workpiece and tool electrode surface during a single discharge in the electrical discharge machining process. In the establishment of the numerical model, they used the temperature dependence of material properties and the expansion of the plasma channel radius over time. They used the temperature distribution curve to calculate the size of the discharge pit and compared them based on the results of finite element analysis and experimental observations. Finally, the prediction errors of the cathode and anode are 2.89% and 2.64%, respectively. In addition, they found that the increase of the pulse current and the increase of the pulse on time have opposite effects on the plasma flushing efficiency.

In another work that modeled SEDM, in order to predict the stress field caused by thermal shrinkage and martensite deformation, Perez et al. [89] calculated the temperature and the resulting change by CALCOSOFT and performed stress analysis by ABAQUS, and finally, they obtained the corresponding tensile stress. They found that in addition to the area of the material that has undergone the martensitic transformation, this causes an increase in the volume of the material and compressive stress in a small part of the crater.

II.4.2.2. Numerical model application in WEDM

In the field of WEDM, the numerical model application is also very often adopted to do research work. To explore the influence of the vibration of the wire on the discharge position and temperature distribution of the workpiece, Zhang et al. [90] proposed a FEM model that considers three-dimensional wire vibration based on the classic thermal model of EDM. Through this model, they simulated the machining process

and verified it through a series of EDM experiments. Finally, they verified that wire vibration had an important effect on the discharge location and could change the temperature. Furthermore, through the comparison of the simulation result, they found that the transverse motion of the wire electrode in all vibration directions has the greatest impact on the WEDM process. As shown in Figure 45, they found that with the increase in the amplitude of wire vibration, the thickness of the recast layer gradually decreases.

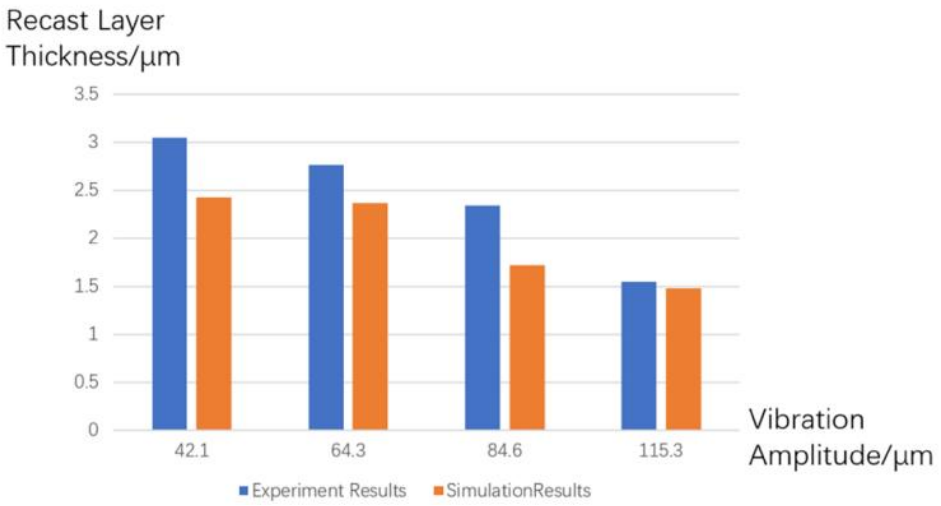

Figure 45. Relation between recast layer thickness and vibration amplitude [90].

To study the optimal parameter values of the WEDM process to obtain better surface integrity and material removal rate, Senkathir and Sandeep [91] selected Inconel 718 as the workpiece and molybdenum as wire. They selected 9 groups of specific parameters for experiments. The time spent in each experiment during the processing and the weight loss after each experiment were recorded to calculate the material removal rate. At the same time, the surface integrity after each experiment was also measured. After that, they used ANSYS to build a FEM model for simulation with corresponding parameters. Finally, in a conclusion, they found that the pulse on and off time plays an important role in improving the material removal rate, and the feed rate plays an important role in optimizing the surface finish.

Kumar et al. [92] used ANSYS to numerically simulate the WEDM to determine the temperature curve. Firstly they obtained the accuracy rate of the numerical model by comparing the experimental results and as shown in Figure 46, the accuracy of the simulation results obtained under the same parameters was 87%. This is because there were some assumptions in the model they defined (such as 100% flushing efficiency, no recast layer deposition, etc.), which makes the numerical model and the experiment have a certain difference. In actual processing, the recast layer exists and

its formation has been introduced in Section II.1.6. At the same time, through simulation results, they found that discharge delay time is the most important factor that caused all investigation results, and by increasing the value of discharge delay time, better MRR results can be obtained.

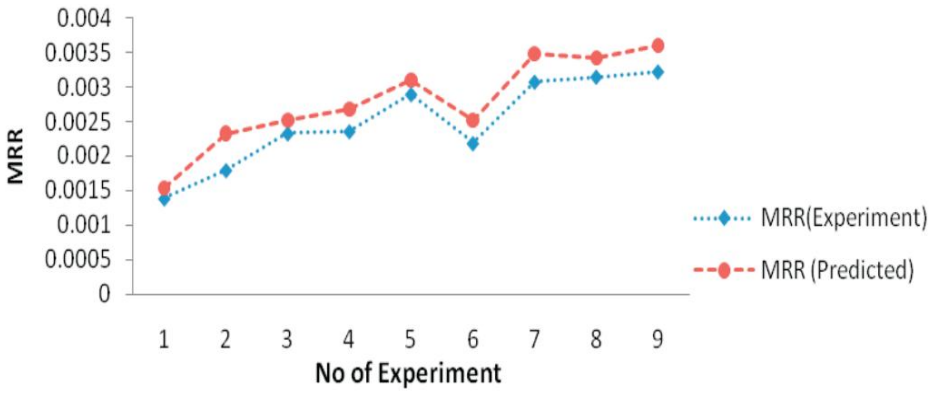

Figure 46. Comparison of results between experimental and simulation data [92].

Singh et al. [93] also adopted ANSYS software to propose a three-dimensional finite element model to predict the temperature distribution of titanium alloy samples under different pulse times and the stress distribution during machining. Related material properties have been used to study temperature distribution and stress distribution. The total heat flow distribution of the titanium alloy workpiece is shown in Figure 47. After the spark ends, thermal stress is generated, and then residual stress is generated after cooling. Through simulation, they found that the voltage and pulse interval have a significant effect on the processing time. The larger the current, the shorter the processing time.

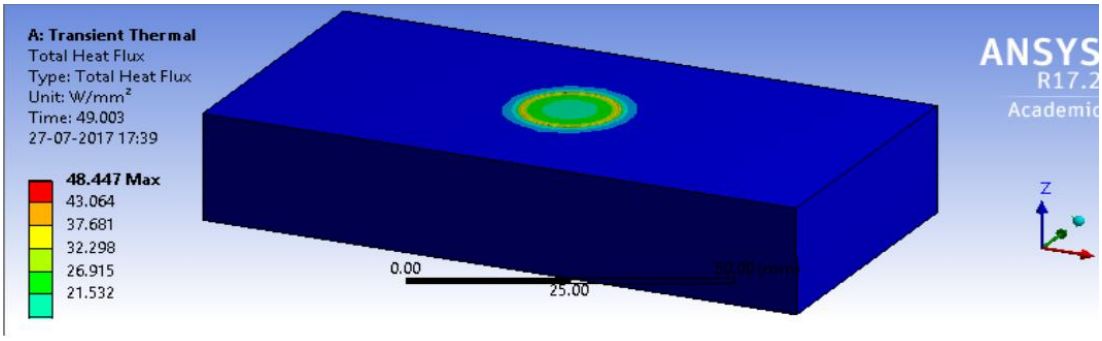

Figure 47. Total heat flow distribution of the titanium alloy workpiece [93].

For improving WEDM's ability to process complex contours and processing speed and avoid harmful surface damage, Hargrove and Ding [94] developed a FEM program to simulate the temperature distribution in the workpiece under different cutting parameters. They determined a set of optimal cutting process parameters for

workpiece manufacturing by minimizing the thickness of the temperature-affected layer and meeting a certain cutting speed. Finally, the validity of the parameters they obtained was verified through experiments.

In addition, for further learning the consecutive sparks in WEDM, Shahane and Pande [95] developed a transient thermophysical finite element model of the WEDM process to calculate the temperature distribution and material removal rate in the workpiece. As shown in Figure 48, they proposed and developed a thermal model of multiple sparks with overlapping craters by modifying the single-spark transient heat transfer model. In the end, they verified that the prediction result of the multiple spark model was close to the experimental value by about 50% by comparing the experimental data with the simulated data.

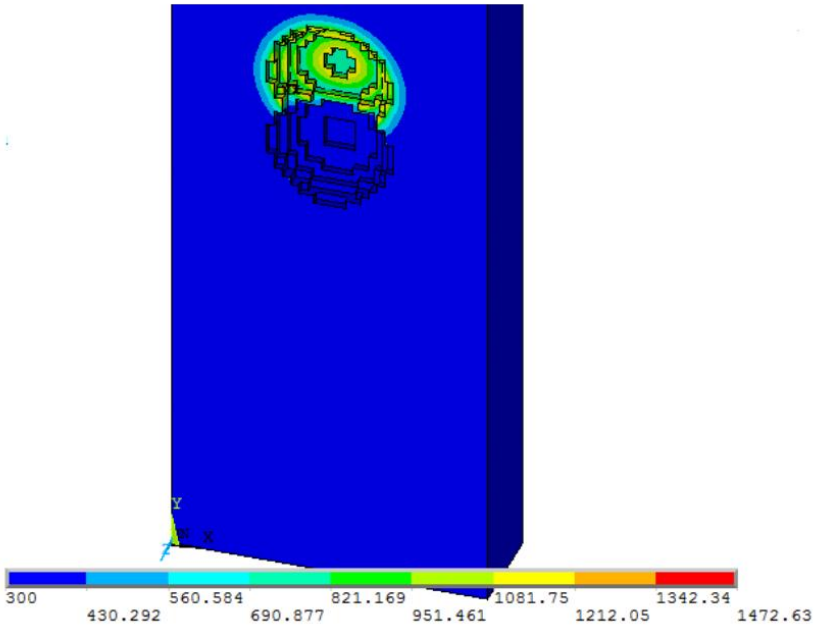

Figure 48. Overlapping craters of two consecutive sparks [95].

From the information gathered in this section, it can be concluded that the numerical model is a promising method to do research work in EDM. It is applied to the research of various fields of EDM such as SEDM and WEDM. This method can help to further understand the EDM process and at the same time, the numerical model can also be used to improve processing parameters to achieve the purpose of improving processing quality. However, when building a numerical model, there are still many aspects that need to be further clarified and improved.

II.4.3. Numerical model of wire breakage

In addition to experiments and observations, more researchers have begun to use the numerical model to simulate the wire internal change in the WEDM process to attempt

to gain more understanding of the cause of wire breakage. Rajurkar and Wang [96] proposed a WEDM spark frequency monitor to prevent wire breakage. In addition, they used thermal models to analyze wire breakage. In fact, relevant literature can be found dealing with the topic of thermal load on the wire in the WEDM process. Spur and Schönbeck [50] presented a reference paper to study the thermal problem on the wire. In their work, a theoretical model for anode erosion in WEDM was solved using FEM. Aspects such as the radius of the plasma channel and the dimensions of the crater produced by one discharge were analyzed in-depth, setting thus the fundamentals for later thermal studies.

Kumar et al. [97] proposed a 3D finite element model, and in the modeling, they used a Gaussian distributed heat source and considered the temperature-dependent material properties. As shown in Figure 49, by using ANSYS software and a static method to predict the influence of different pulse times on temperature distribution and stress distribution in the online cutting process, they found that thermal stress was generated after the discharge ended, and then residual stress was generated after cooling. At the same time, the peak temperature increases sharply with the pulse on time, which means that the increase of the pulse on time increases the probability of wire breakage.

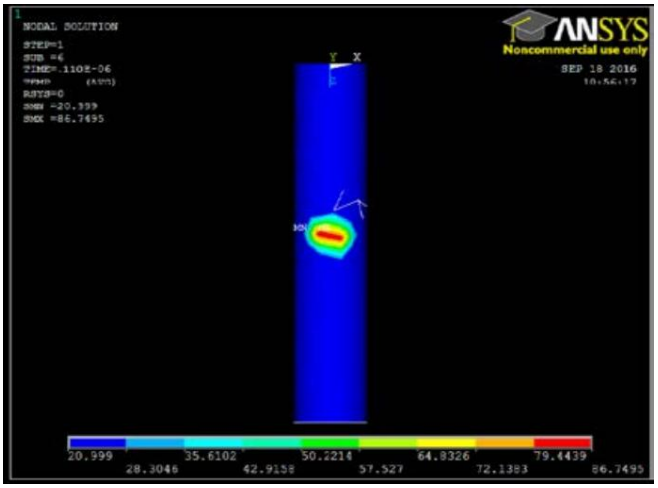

Figure 49. Temperature distribution on the wire [97].

In another work by Kumar et al. [98], they further verified the previous model by comparing the crater obtained by the numerical modeling with the experimental observations. At the same time, in order to further explore the reasons for wire breakage, they used this model to simulate the formation of the crater and used the crater volume to evaluate the erosion rate of the wire. By using different machining currents and voltages, as shown in Figure 50, they found that the temperature of the wire increases as the current and voltage increase during the machining. Therefore,

the increase in current and voltage is also an important cause of wire breakage.

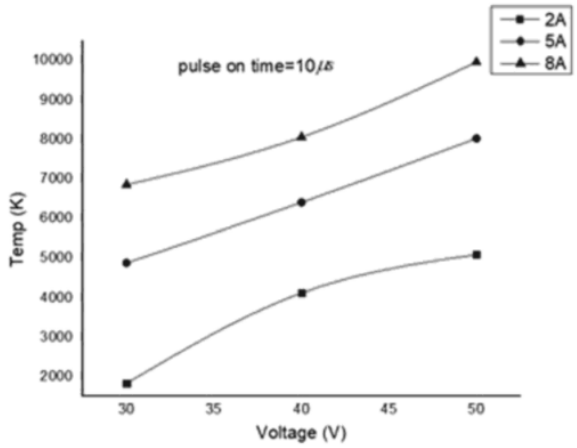

Figure 50. The maximum temperature under different currents and voltages [98].

In order to present the transient thermal and structural simulations of wire electrodes in the WEDM process, Singh et al. [99] used Ansys to perform FEM simulations. They used a three-dimensional finite element model to predict the temperature distribution, the total heat flux under different time pulses, and the stress distribution in the WEDM wire. The maximum and minimum transient heat flux distributions on the wire are shown in Figure 51. Eventually, they found that the peak temperature increased sharply as the pulse on time increased and it makes the wire breakage more likely to happen.

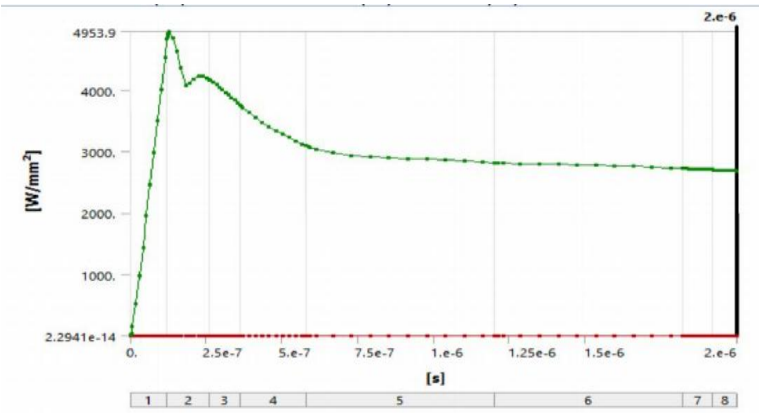

Figure 51. Graphical representation of the maximum and minimum transient heat flux distribution on the wire electrode [99].

Also, Boipai [100] used finite element analysis to determine the temperature distribution, displacement and stress distribution of the wire electrode tool of the wire cutting machine tool. He used ANSYS software to establish a three-dimensional finite element model. After the spark ended, thermal stress was generated as Figure 52, and residual stress was also generated after cooling. Finally, the finite element model of a

single spark with temperature-dependent material properties is carried out. He found that with the increase of pulse on time, the thermal stress increases and the molten part of the wire increases. This means that when a higher pulse on time is used the wire breakage occurs more frequently.

To predict wire breakage, Das and Joshi [101] analyzed the wire cross-section. They used the FEM to establish a two-dimensional nonlinear transient heat transfer model of the wire electrode. In their numerical model, they used Gaussian heat flux and considered the latent heat of brass wire melting. The model can predict the peak temperature after a discharge phenomenon occurs under different input parameters. According to the temperature curve, the shape and area of the wire affected by heat were estimated and the corrosion rate of the wire is calculated. In addition, they found that the peak temperature reached by the wire after a single discharge increased with the increase of voltage and current due to the increase of input power.

In another work by Das and Joshi [102], in order to further study wire breakage, they developed a three-dimensional FEM thermal model on wire (Figure 52) to calculate the temperature and induced stress and verified the calculation ability of the developed model through experiments. At the same time, they used X-ray diffraction techniques to obtain experimental values of residual stress. Finally, the safety index of wire is evaluated by calculating the ratio between the maximum value of the residual stress caused and the yield stress of the wire.

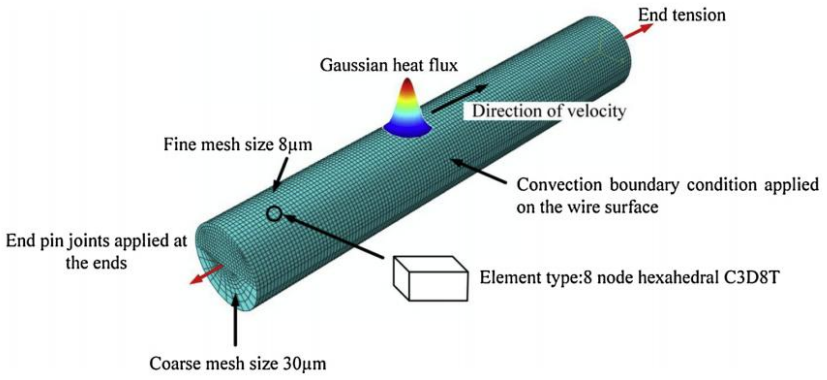

Figure 52. Three-dimensional FEM model on the wire [102].

Joshi et al. [103] considered the effect of plasma flushing efficiency in the modeling and optimized the numerical model. Through modeling, they found that the temperature of the wire and the size of the crater increased by increasing the voltage, current and pulse on time. At the same time, by increasing the diameter of the wire, the plasma width will also increase. It means that the same amount of energy was transferred to a larger contact surface, and the interface temperature decreased. The size of the

crater decreases with the increase in the wire diameter, which means that the diameter of the wire is inversely proportional to the probability of wire breakage.

Through the introduction of this section, it can be found that many researchers have begun to use a numerical model to study the reasons for wire breakage and explored the method for reducing the frequency of wire breakage. At the same time, this kind of model can also be used to predict wire breakage in WEDM. However, building a numerical model is not enough for realizing real-time monitoring of wire breakage, more work and research are still required.

II.5. Summary of research status in EDM

Since the manufacturing industry has increasingly high requirements for EDM processing technology, to improve machining accuracy, the basic research of EDM has continued research and it becomes more and more popular and essential. At present, there are a lot of results in the existing research that have been finished. Whereas, due to the complex machining process of EDM, in order to meet the development of a more precise EDM machine, it is necessary to conduct further research. The summary of the existing research and the direction that can be further explored is stated as follows:

- A large number of research works have been finished to explore the discharge characteristics in EDM. In that, the plasma channel generation was observed by spectroscopy and a high-speed camera. As the result, it is found that not only generated in liquid but also a bubble. This means that the plasma-generated environment needs to be considered carefully.

- The heat distribution in the EDM process has been studied by a lot of researchers. For detecting and simulating the process, the combination of the thermal model and the experimental result is seen as a good solution idea. Whereas, due to the various hypotheses of the heat source model, plasma channel radius, plasma flushing efficiency, latent heat and the setting conditions, there is still not a determined model. Therefore it is still a good topic to explore and it is worth improving a more accurate and credible thermal model to further understand the EDM process.

- The discharge delay time reflects the dielectric breakdown strength of the gap between the electrodes. As it is known that with the change of machining conditions in EDM, the delay time of discharge is also variable. Through the

review, it can be known that a large number of studies have been finished in the field of SEDM. Whereas in terms of WEDM, the work is still less than enough and more experiments and simulation work should be carried out to get a deeper understanding.

- Debris particles are generated by the recondensation of that molten metal by the dielectric liquid flushing during the EDM process. Many researchers have researched the debris produced in the EDM process to understand its influence on the machining process and results. In addition, for exploring the movement of debris during the EDM process, the corresponding simulation in the machining gap was also taken into account in some research. Whereas, the existing works in this field are far from enough. More studies of debris including but not limited to the observation in a range of nanometers and the study of debris composition still need to be researched.

- Wire plays a crucial role in WEDM and can decide the machining quality. But the occurrence of wire breakage will affect the machining accuracy. Therefore, wire breakage is a critical topic in WEDM Industry. A lot of researchers focused on this popular problem and did a huge number of experiments to further understand it. Since the concentration of discharge causes the accumulation of heat, it is considered to be an important cause of wire breakage. Therefore, for decreasing the frequency of wire breakage and improving machining quality, research on the discharge position becomes very important. The application of the monitoring of the discharge position in the WEDM field also has become more and more popular in the industry. However, in actual industrial applications, the accuracy and real-time monitoring are still worth studying and improving.

- Nowadays, numerical modeling is a promising approach for getting a better understanding of crater in EDM and it can also be used to improve processing parameters to achieve the purpose of improving processing quality. For that, a lot of fundamental studies become necessary to better define boundary conditions and reduce modeling uncertainties. In addition, there are still many aspects that need to be further clarified and improved in the process of numerical model building.

Chapter III: Exploration of discharge delay time in WEDM

III. EXPLORATION OF DISCHARGE DELAY TIME IN WEDM

The understanding of discharge delay time (t_d) is vital to understand the discharge quality in EDM. This topic has been extensively studied in SEDM, but the current research work in WEDM is not enough and it needs to be studied in depth. In this chapter, the study on t_d of single discharges was carried out to explore the influence of gap width (g), surface roughness and volume flushing flow rate (Q_f). After that, for further exploring t_d in the general machining process, the experiment about t_d of continuous discharges was also done and further discussed.

III.1. Introduction

In WEDM, when an open voltage is applied between the wire and the workpiece, the discharge does not occur until reaching the breakdown point. The time duration from starting application of open voltage to discharge occurrence is named discharge delay time (t_d). It is an important indicator used to distinguish the type of discharge or to judge the discharge situation. In this chapter, two aspects of single discharge and continuous discharge were both taken into account.

In Section III.2, the single discharge experiment was finished under different machining parameters to find the possible influencing factor on t_d. From the experimental result, it was learned that g, surface roughness and Q_f can affect t_d. Furthermore, it was found that an increase in g or a smoother workpiece surface made the discharge delay time larger. In addition, with a higher Q_f, the discharge delay time increased. Then, the reason for the influence of Q_f was further explored through the measurement of wire displacement. Finally, it was found that with higher Q_f, the average position of the wire is farther from the initial position. In other words, the higher Q_f made g larger, and it made t_d longer which has been already verified.

Then to investigate t_d in the general WEDM process, the continuous discharge experiment was introduced in Section III.3. During the experiment, the observation of the gap between the wire and the workpiece was also finished by a high-speed video camera. Through the analysis of experimental data, the relationship between discharge position and t_d was found that more discharges occurred in the process of bubble expansion. It verifies the influence of the bubble expansion on the discharge occurrence, and it can be explained by the effect of the debris particles concentrated at the bubble boundary that can make t_d shorter.

Finally, some conclusions are presented in Section III.4. The relative results in this chapter can help better understand the discharge conditions and at the same time, it can be useful for improving the configuration of machining parameters in future works.

III.2. Discharge delay time of single discharge in WEDM

Considering the single discharge experiment can better control the discharging parameters, for exploring the possible influencing factors on t_d, the single discharge experiment was finished first.

III.2.1. Experimental method

To collect t_d of a single discharge under different machining conditions, the wire length between the upper nozzle and the lower nozzle was set as H. The workpiece was fixed corresponding to the middle part of the wire which is shown in Figure 53 (a). The materials of the workpiece and wire are respectively Sverker 21 and brass. Moreover, CWT Rogowski current transducers and Tektronix ThDP0200 Differential Probe were respectively used for detecting the current and voltage, and a Tektronix 5034B Digital Oscilloscope was used for collecting signals with a sample rate of 10 MS/s. Then, as shown in Figure 53 (b), the wire swept over the workpiece surface with the set g. After that, only the information of the first discharge of each cutting was selected to do further study for ensuring that this discharge occurred under the setting condition. This process was repeated 30 times under each condition. In other words, t_d of 30 single discharges of each setting condition were obtained. Figure 54 shows the acquired voltage signal and current signal of one discharge from which t_d can be obtained.

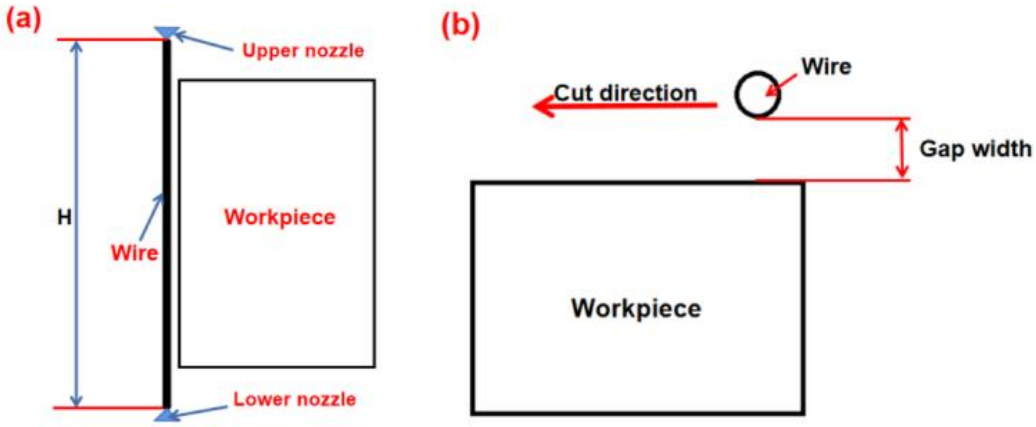

Figure 53. (a) Fixation of wire and workpiece; (b) Cutting method.

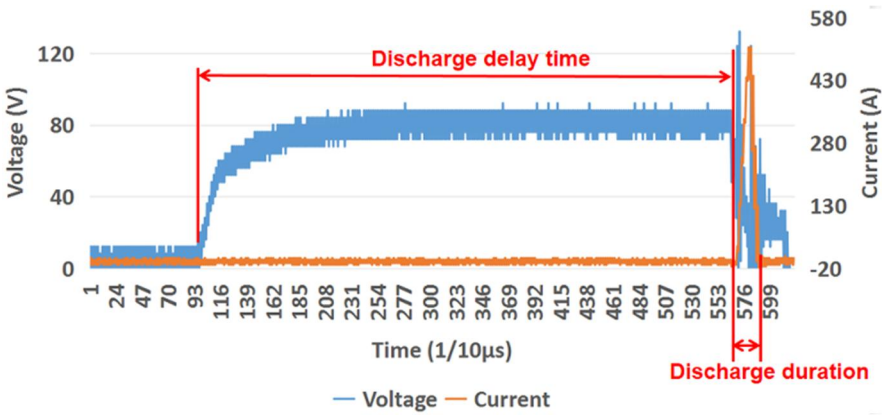

Figure 54. Voltage signal and current signal of one discharge.

III.2.2. Relation between gap width and discharge delay time

The gap width g is an important machining parameter in WEDM. In this section, the relative experiment will be introduced and the relation between g and t_d will be found through the experimental result.

III.2.2.1. Experimental set-up

For exploring the relation between g and t_d, in the following experiments, 3 kinds of g were selected to use and other machining parameters were kept the same. With the parameters shown in Table 2 and the measurement method introduced in the previous section, the experiments under different g were finished.

g (μm)	5	10	20
H (mm)	30		
Q_f (L/min)	16		
R_a (μm)	0.32		
R_z (μm)	1.84		
h (mm)	30		

Table 2. Machining parameters.

III.2.2.2. Experimental result

After cutting 30 times under each kind of g, t_d of every discharge under different gaps was obtained. Then, the average discharge delay time ($t_{d,ave}$) is calculated by Eq.18. In that, N is the total number of discharges. The result of $t_{d,ave}$ under different g is shown in Figure 55 (a). It is clear that $t_{d,ave}$ under 20μm of g is the longest, and $t_{d,ave}$ shows an increasing trend with the increase of g. Moreover, the probability p that discharge

does not occur until any t_d can be expressed as Eq.19, where n is the number of discharge that still does not occur. The relation between t_d and p was expressed with the Laue plot and it was plotted in Figure 55 (b). From the slopes of the curves, it can be learned that smaller g results in shorter t_d. This result verifies the influence of g on t_d in WEDM is the same as that in SEDM which was found in the work of Morimoto and Kunieda [57].

$$t_{d,ave} = \frac{\sum t_d}{N} \quad \text{Eq.18}$$

$$p = \frac{n}{N} = exp(-\frac{t_d}{t_{d,ave}}) \quad \text{Eq.19}$$

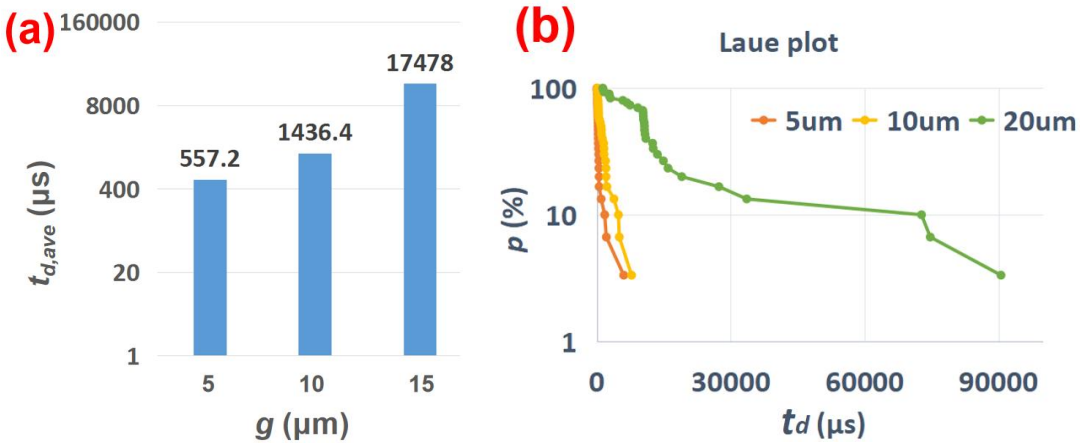

Figure 55. (a) $t_{d,ave}$ under different g; (b) Influence of different g.

III.2.3. Relation between workpiece surface roughness and discharge delay time

The influence of the workpiece surface roughness on t_d was also taken into account to do the investigation. In this section, there will be the t_d experiment on 2 prepared workpieces with different values of surface roughness, and the relation between workpiece surface roughness and t_d will be also explored through the corresponding result of $t_{d,ave}$ and the Laue plot.

III.2.3.1. Experimental set-up

For investigating the relation between workpiece surface roughness and t_d, two different surfaces with different roughness values were prepared. With the machining parameters in Table 3, the part of the surface that was cut with only one time of roughing cut is called a rough surface. Another part that was cut with one time of rough cut and two times of trim cuts is called a smooth surface. The mean surface roughness (R_a) and the maximum surface roughness (R_z) of each kind of surface are

shown in Table 4. To keep the *g* the same in the experiment with different surface roughness, a part of the smooth surface was reserved for doing the calibration as shown in Figure 56 (a). Through surface observation that was realized with Alicona optical 3D measurement system, the height difference was gotten as Figure 56 (b) and the relative *g* on the rough surface also can be defined. Finally, the experiment was realized under the parameters shown in Table 5.

Parameters	Rough cut	1st trim cut	2nd trim cut
U_o (V)	80	100	90
U_s (V)	52	48	10
f (mm/min)	12	10	10
t_{off} (µs)	12	9	1
F (N)	10	18	18

Table 3. Machining parameters for preparing different surface roughness.

Parameters	R_a (µm)	R_z (µm)
Smooth	0.32	1.84
Rough	2.41	12.17

Table 4. Surface roughness.

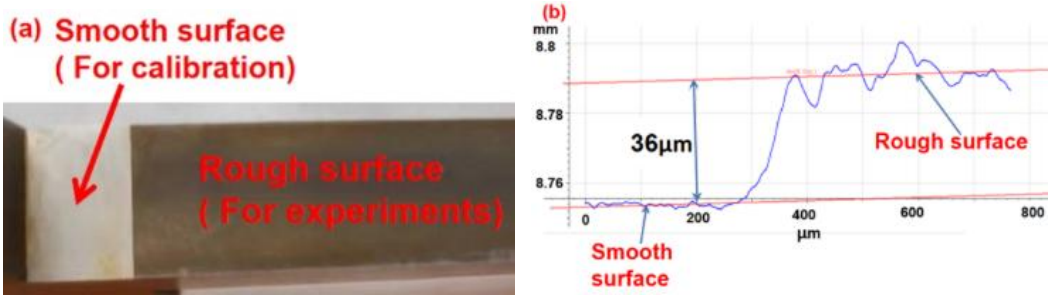

Figure 56. (a) Workpiece with two different surface roughness values; (b) Height difference between the smooth and the rough surface.

Surface roughness	Smooth	Rough
H (mm)	15	
g (µm)	14	
Q_f (L/min)	9	
h (mm)	15	

Table 5. Machining parameters.

III.2.3.2. Experimental result

With the described experimental method, t_d of 30 single discharges on each kind of surface was gotten. Firstly $t_{d,ave}$ was calculated by Eq.18 and they were 175.87μs and 87.99μs on the smooth surface and the rough surface, respectively. Consequently, it can be known that discharge occurs easier on the rough surface. Then, the Laue plot was also obtained in Figure 57. The slope of the curves verified that, with the same t_d, it is more difficult to discharge on a smooth surface.

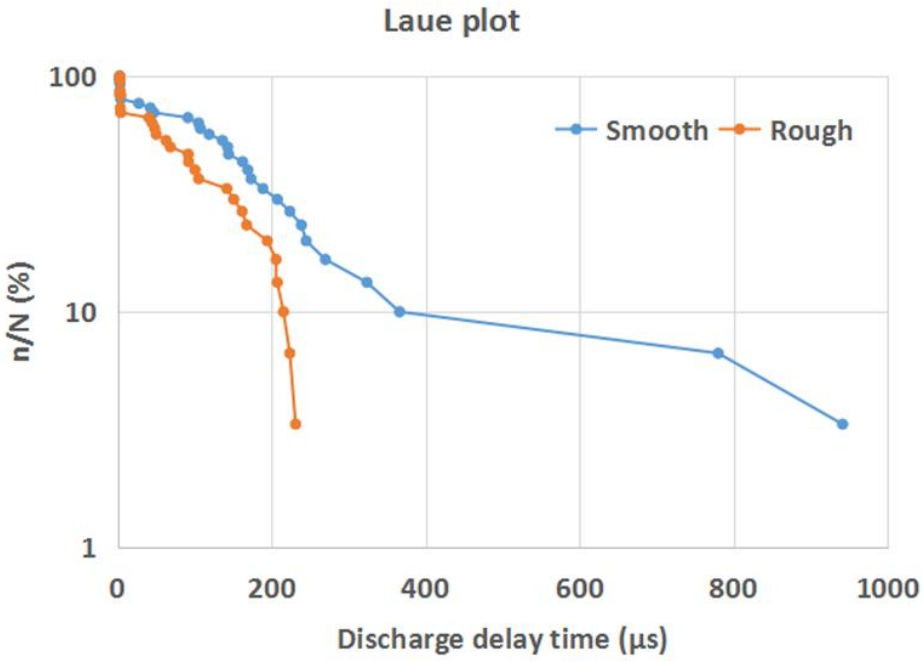

Figure 57. Influence of different surface roughness.

III.2.4. Relation between flushing flow rate and discharge delay time

Flushing flow rate (Q_f) was another machining parameter considered to do further research. In this section, experiments under different Q_f. were finished. Through the experimental result, the influence of Q_f on t_d was learned. Then, the reason for the influence of Q_f was assumed and the corresponding experiment was carried out to for verifying the assumption.

III.2.4.1. Experimental set-up

In the experiment, Q_f from the upper nozzle and the lower nozzle was always set as the same. Next, with the parameters shown in Table 6, 3 kinds of Q_f were set to do the corresponding experiments. Using the measurement method explained in Section III.2.2, the voltage signal and current signal of every single discharge were also collected to analyze t_d.

Q_f (L/min)	0	4	9
g (µm)	10		
H (mm)	30		
R_a (µm)	0.32		
R_z (µm)	1.84		
h (mm)	15		

Table 6. Machining parameters.

III.2.4.2. Experimental result

With the gotten t_d of 30 single discharges under each kind of Q_f, $t_{d,ave}$ was calculated as 51.20µs, 127.33µs and 185.93µs respectively corresponding to 0L/min, 4L/min and 9L/min of Q_f. The Laue plot is shown in Figure 58. It is obvious that discharge becomes easier with a lower Q_f and it shows an increasing trend of $t_{d,ave}$ with the increase of Q_f.

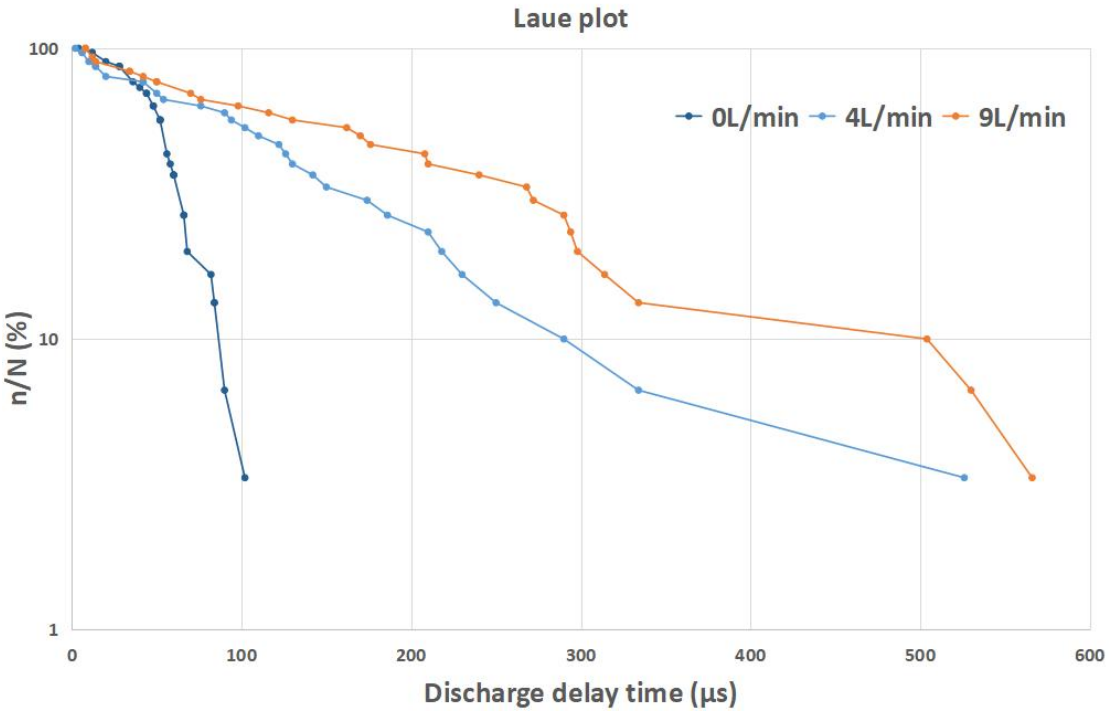

Figure 58. Influence of different Q_f.

Through the experimental result, it is known that with the change in Q_f, t_d changed. About the reason for this influence, it is assumed that the flushing flow may change the wire displacement and it may change the gap distance between the wire and the workpiece. For verifying the assumption, more experiments for studying the wire displacement need to be performed.

III.2.4.3. Exploration of the reason for the influence of the flushing flow rate on discharge delay time

For further understanding of the reason for the influence of the Q_f on t_d, the apparatus shown in Figure 59 which included plastic optical fiber and He-Ne laser was adopted to measure the wire displacement. After fixing the apparatus on the WEDM machine, the wire crossed through the center of the hole. Then, the two optical fibers on each axis were connected with the phototransistor and the data was collected through an oscilloscope under the sampling frequency of 50kS/s. For starting the experiment, the calibration of the sensitivity of the sensors is essential. As shown in Figure 60 (a) and Figure 60 (b), the calibration was carried out respectively on the x-axis and y-axis.

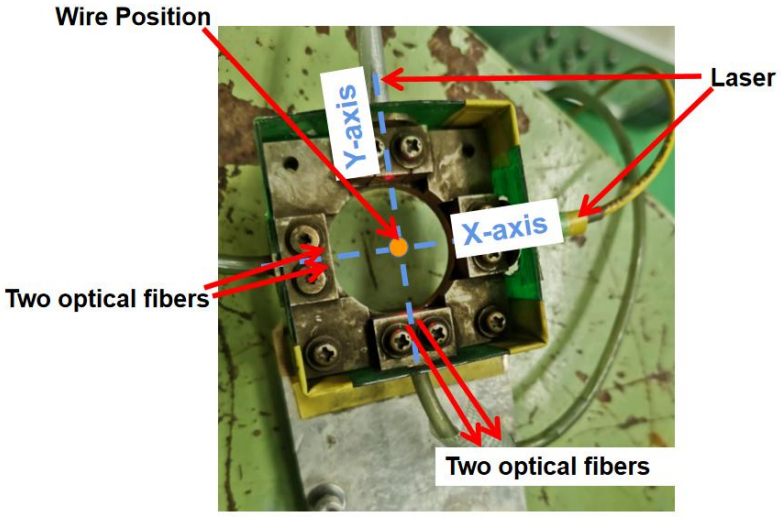

Figure 59. Apparatus for measuring the wire movement.

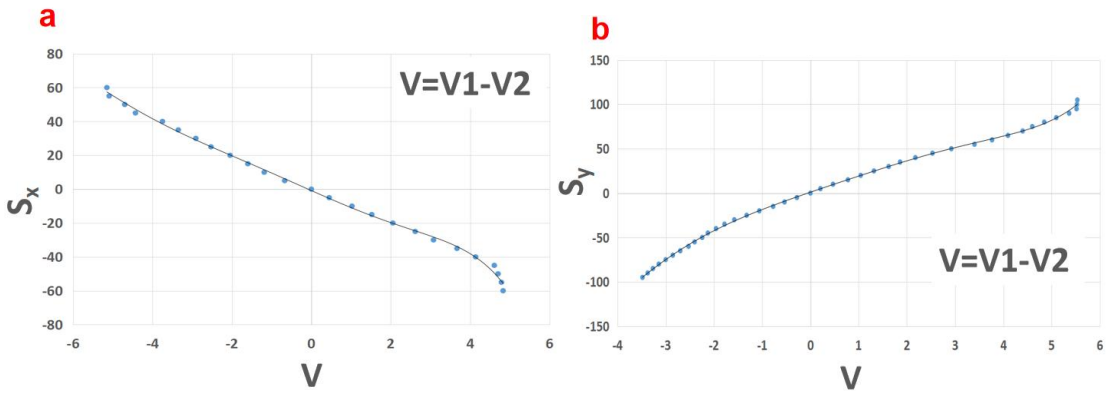

Figure 60. Calibration curve: (a) On the x-axis; (b) On the y-axis.

After data processing, the relation between the signal value and the wire displacement was found as shown in Eq.20 and Eq.21. In that, S_x and S_y are respectively the wire movement in the x-direction and the y-direction, a is the corresponding signal value.

$$S_x = -0.0009x^6 - 0.0083x^5 + 0.0097x^4 + 0.158x^3 + 0.2609x^2 - 10.358x - 1.2088 \quad \text{Eq.20}$$

$$S_y = 0.0028x^6 - 0.0004x^5 - 0.119x^4 + 0.2768x^3 - 0.6056x^2 + 18.583x - 8.8809 \quad \text{Eq.21}$$

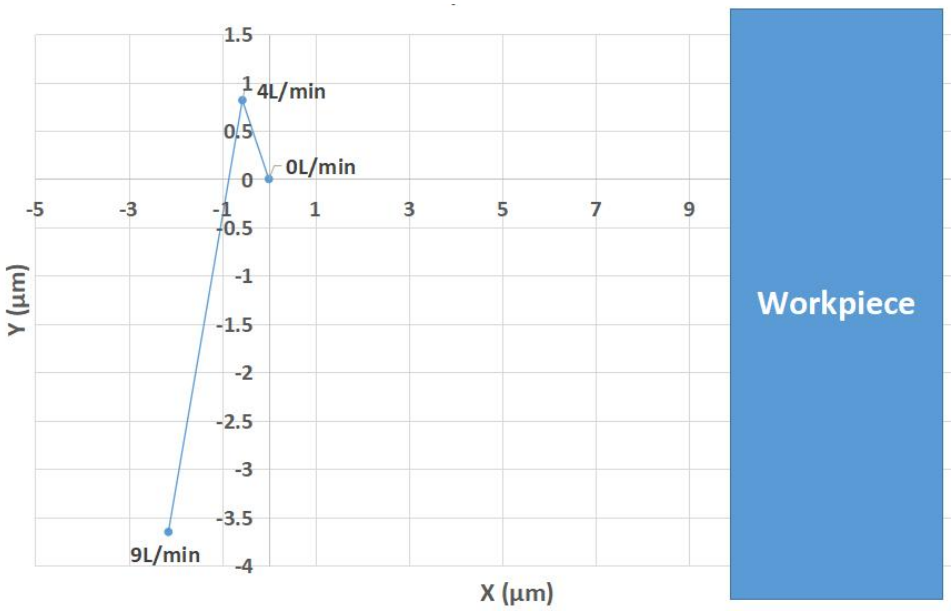

Figure 61. Displacement amplitude under different Q_f.

The displacement in the x-direction (S_x) and in the y-direction (S_y) was calculated with Eq.22 and Eq.23, in that, x_0 and y_0 is the coordinate of wire position without flushing flow, x_i and y_i is the coordinate of the current wire position, n is the data number. and then the result is shown in Figure 61. From that, it can be known that with the increase in fluid speed, the wire displacement increased. The trajectory under different Q_f is shown in Figure 62.

$$S_x = \frac{\sum_{i=1}^{n}(\sqrt{(x_i - x_0)^2})}{n} \quad \text{Eq.22}$$

$$S_y = \frac{\sum_{i=1}^{n}(\sqrt{(y_i - y_0)^2})}{n} \quad \text{Eq.23}$$

From the result, it was learned that with higher Q_f, the average position of the wire is farther from the initial position. In other words, the higher Q_f made g larger, and it made t_d longer which was verified in the previous section.

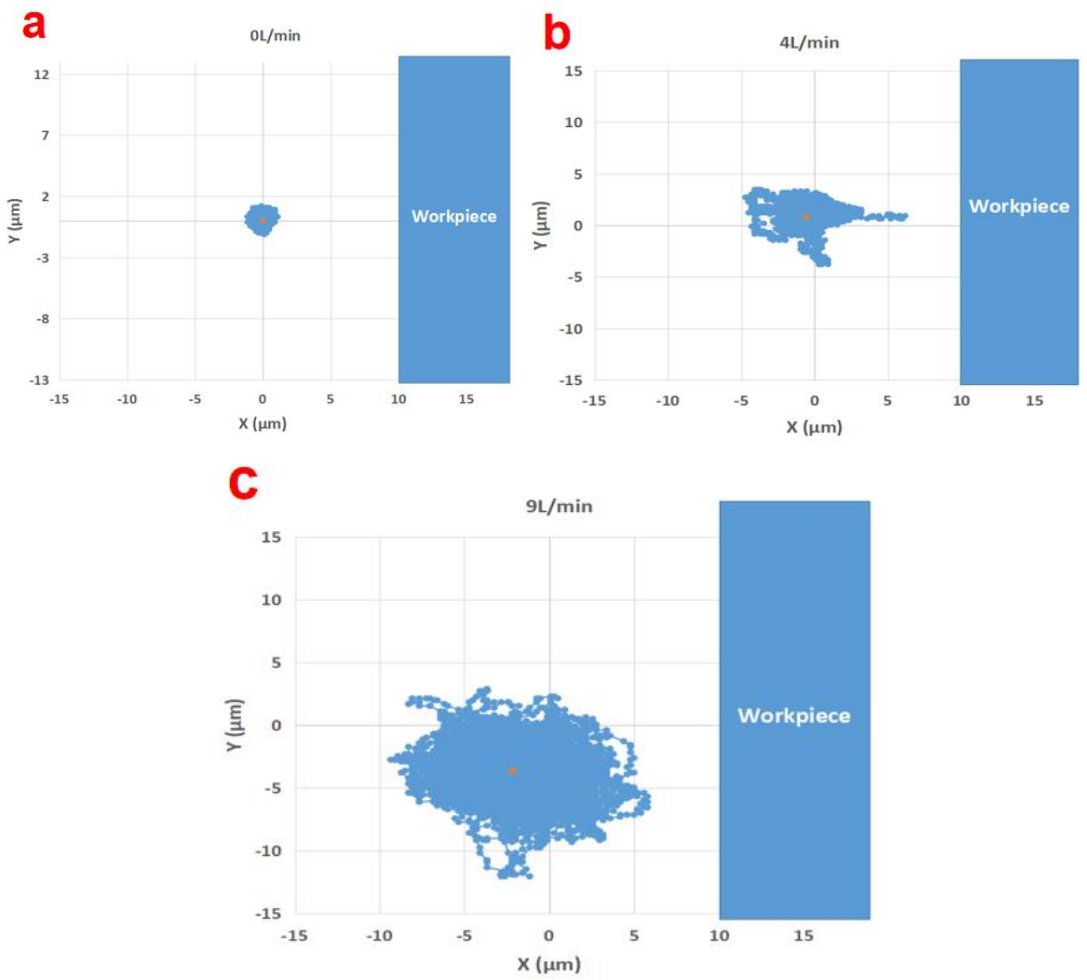

Figure 62. The trajectory of the wire: (a) 0L/min; (b) 4L/min; (c) 9L/min.

III.3. Discharge delay time of continuous discharges in WEDM

For further exploring t_d in the general WEDM process, the study on continuous discharges is essential. In this section, the experiment for collecting t_d of continuous discharges will be introduced. In addition, for further investigating the influencing factor of t_d, the observation of the gap phenomenon during the discharge occurrence using a high-speed video camera will also be presented in this section.

III.3.1. Experimental set-up

The WEDM process was observed using a NAC MEMERECAM x-3 high-speed video camera with a lens of NIKON Ai Micro-NIKKOR 55mm F2.8. The SUMITA metal halide lighting system LS-M250 was used as illumination. A workpiece of cold tool steel SKD 11 with a thickness of 10mm and a brass wire with 0.2mm of diameter was selected. Firstly, the workpiece surface was prepared by Sodick AP200 L WEDM machine with a

roughing cut and two times trim cut. The machining parameters are shown in Table 7. After that, R_a and R_z were measured with Mitutoyo C-3200. The result of R_a and R_z were respectively 0.41µm and 2.91µm.

WEDM Parameters	Roughing cut	1st trim cut	2nd trim cut
U_o (V)	80	80	80
U_s (V)	35	53	30
f (m/min)	10	10	10
t_{off} (µs)	15	23	1
F (N)	12	12	12

Table 7. Machining parameters for preparing workpiece surface

Then, the workpiece was fixed at the middle position between the upper nozzle and the lower nozzle, and the distance between the two nozzles was 30mm. From the initial wire position shown in Figure 63, cutting was finished along the prepared surface of the workpiece using the parameters shown in Table 8. To ensure that the observation of the gap phenomenon was made under a stable machining state, it was not started until the wire advanced 5mm along the cutting direction. Then, the observation was performed during the next 1mm of cutting. After that, g was measured as 11.3µm through the WEDM machine.

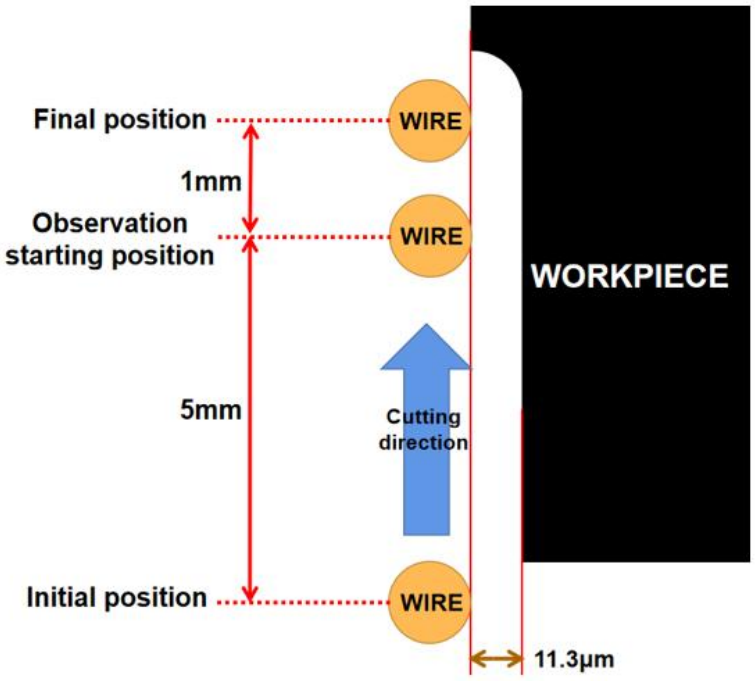

Figure 63. Schematic diagram of the experiment.

I (A)	150
U_o (V)	80
U_s (V)	35
f (m/min)	10
t_{off} (μs)	23
F (N)	12
Q_f (L/min)	9

Table 8. Machining parameters for the experiment.

The schematic diagram of the observation system is shown in Figure 64. In the observation system, the high-speed video camera was connected to a personal computer (PC) to save the image data. The Tektronix MDO3024 oscilloscope was adopted with a sampling rate of 10MS/s. The current was measured by Pearson current sensor and the voltage was measured by Tektronix TPP200 voltage probe. Moreover, a current value of 100A was set as the trigger threshold to activate the high-speed video camera to start recording. During the observation, the camera's framing signal was also saved using the oscilloscope for later synchronizing the photo and the discharge signal. In addition, the high-speed video camera setting is shown in Table 9. Notably, the discharge interval was considered to select the camera framing rate that aimed to make sure that only one discharge exists at most in each photo and make further analysis easier. Finally, 12,000 frames were gotten from the high-speed video camera and the corresponding signals from the oscilloscope in the experiment.

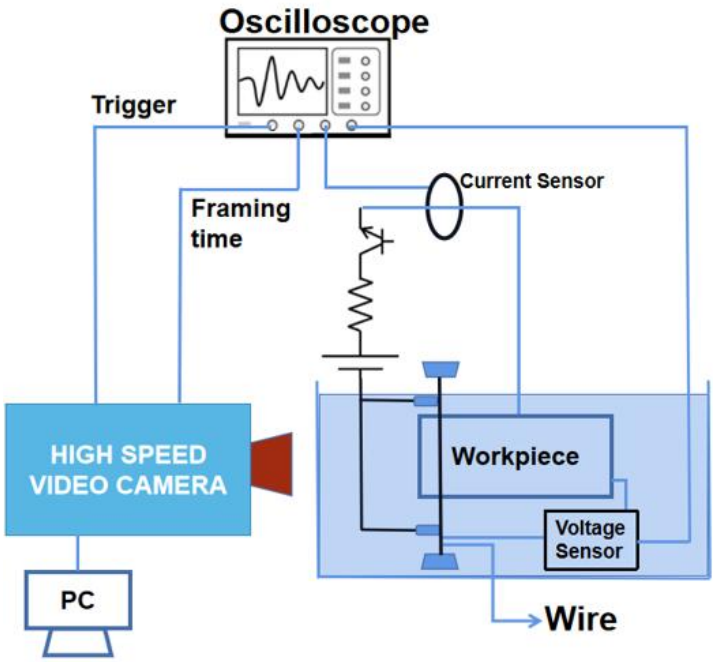

Figure 64. Construction of the observation system.

Resolution (pixel)	512*320
Framing rate (fps)	40000
Shutter speed (μs)	25

Table 9. High-speed video camera setting.

III.3.2. Experimental data processing

The frames gotten from the high-speed video camera were saved as photos for further processing. As shown in Figure 65, the discharge and the bubble can be seen in the photos. Next, a group of signals which was obtained from the oscilloscope is shown in Figure 66. With the signals, t_d can be obtained. Also, the combination of the framing signal and the current waveforms was used to find the corresponding discharges in the photos. Finally, the corresponding photos and t_d of 713 discharges were gotten for further investigation.

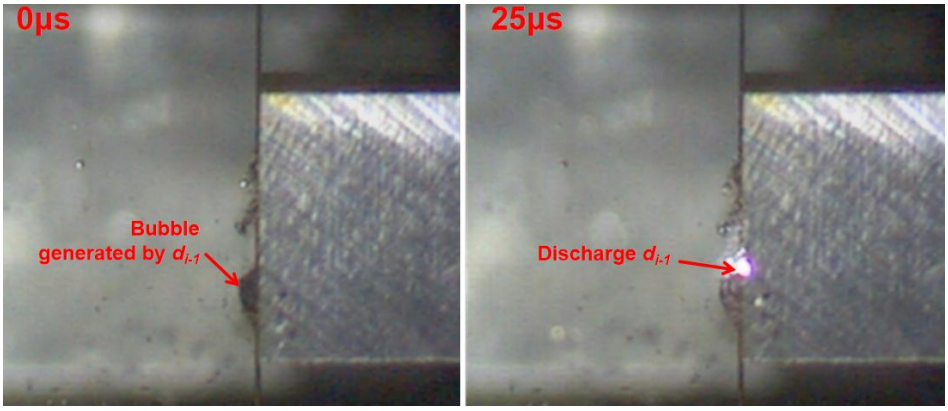

Figure 65. Photos obtained from the experimental observation.

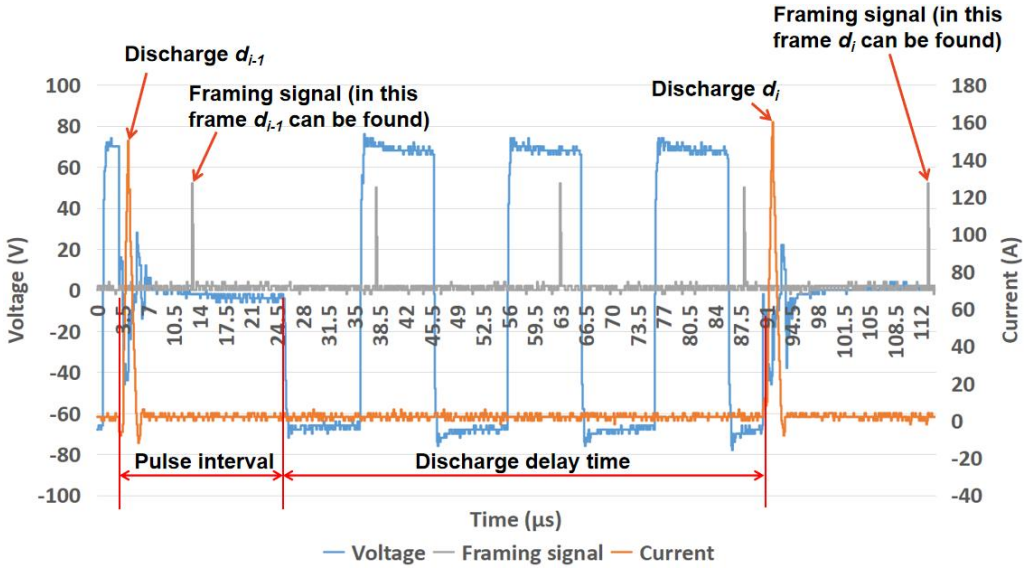

Figure 66. Recorded signals: gap voltage, discharge current and framing signal.

Then, MATLAB was adopted to analyze the photos for finding the discharge location. Through analyzing the grayscale of the photo with discharge, the pixel point whose grayscale is most different from that in the photo without discharge was found. As shown in Figure 67, the accuracy of this discharge location detection method was checked. By comparing with the discharge position in the photo, it is known that the discharge location detected through grayscale analysis overlaps with that observed from the photo and it verifies that this discharge location detection method is feasible.

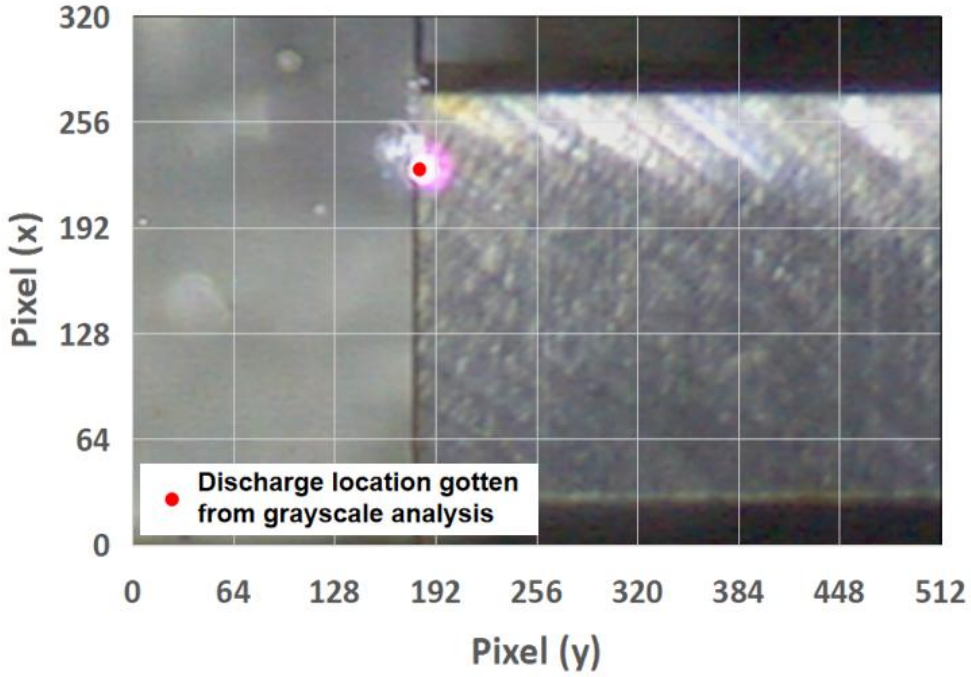

Figure 67. Discharge location obtained from the grayscale analysis.

III.3.3. Discussion on the relationship between discharge delay time and discharge position

With the discharge location detection method introduced in the previous section, the discharge locations of all the discharges were gathered. Then, the histogram of the distance between *i* th discharge (d_i) and *i-1* th discharge (d_{i-1}), *i-5* th discharge (d_{i-5}),and *i-20* th discharge (d_{i-20}) are shown respectively in Figure 68 (a), 68 (b) and 68 (c). In addition, a random distribution model was built through MATLAB assuming that the discharge location is determined at random. In the random model, the histogram of the distance between two consecutive discharges was obtained as shown in Figure 68 (d). In Figure 68 (a), it is obvious that the percentage of the distance between d_i and d_{i-1} shorter than 0.5mm is 24% and it is 14.1% higher than that of the random model which is shown in Figure 68 (d). Then, from the comparison between Figure 68 (a), Figure 68 (b) and Figure 68 (c), it is found that with more discharges between two discharges, the percentage shorter than 0.5mm decreases. Moreover, if there are a

sufficiently large number of discharges between two discharges, the distribution tends to be random. This means that the discharge d_{i-1} exerts the greatest influence on the location of d_i.

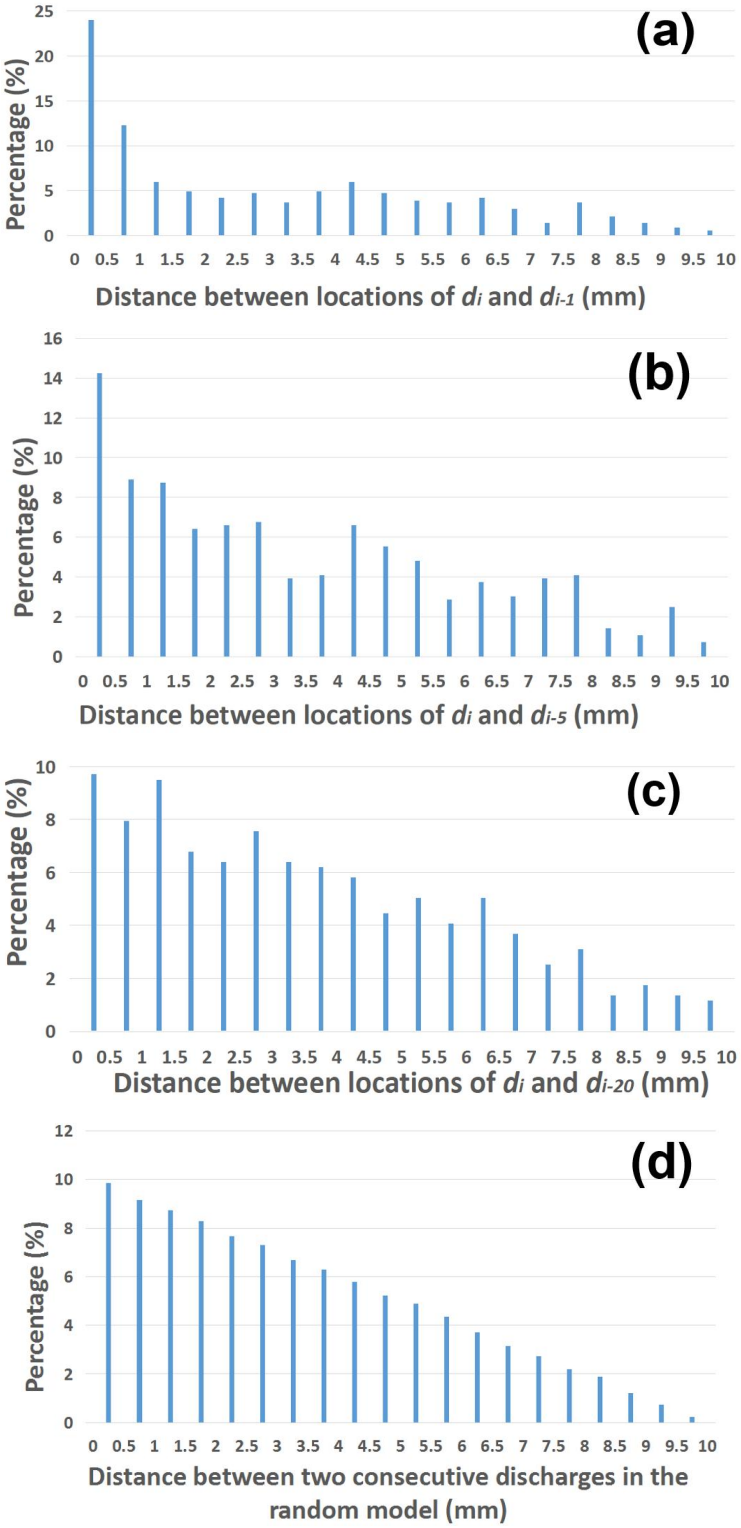

Figure 68. Histogram of the distance between discharges: (a) Between d_i and d_{i-1}; (b) Between d_i and d_{i-5}; (c) Between d_i and d_{i-20}; (d) Between two consecutive discharges in the random model.

As Yoshida and Kunieda [19] found that most of the debris particles concentrate at the boundary of the bubble generated by the discharge and it made t_d shorter, the influence of d_{i-1} on the occurrence of d_i is considered to be closely related to the bubble generated by d_{i-1}. To verify this assumption, the set of discharges d_i that occurred within 0.5mm from the location of d_{i-1} was selected to do further analysis. Furthermore, the bubble radius was measured using ImageJ which is an image processing software. The measurement results in Figure 69 show that the size of the bubble is almost uniform and so that the oscillation period of the bubble is similar. The first cycle of bubble oscillation is always about 200μs, and the bubbles disappear after about 500μs because of the reaction of hydrogen and oxygen in the gap [104].

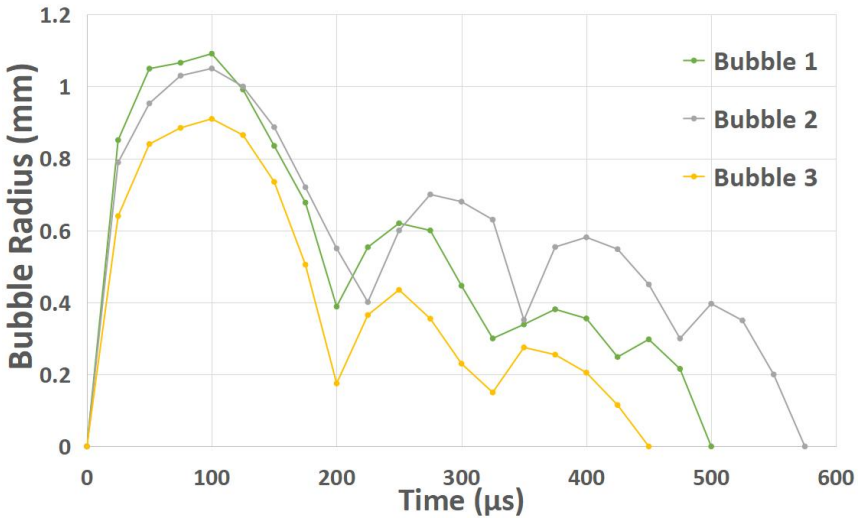

Figure 69. Oscillation of bubbles.

As it is known that with more discharge occurring more debris particles are generated, which makes the image too dark to find the accurate position of the discharge and the bubble. For getting a clear observation image, sufficient flushing flow was indispensable to clean the machining area. Whereas, due to the existence of flushing flow, the bubble generated by d_{i-1} was convective before d_i occurred and it means that there existed a slight movement of the bubble. Therefore, the distance (l_i) between the location of d_i and the center of the bubble generated by d_{i-1} was introduced as a new reference for studying the influence of the bubble generated by d_{i-1} on the occurrence of d_i. As shown in Figure 70, l_i was measured through ImageJ. Then, the relationship between the t_d and distance l_i was plotted as points which are shown in Figure 71. In addition, the change in the bubble radius due to oscillation is also shown in Figure 71 for comparison. It is found that between 0mm and 0.2mm of l_i there are few discharges, and the points of l_i are distributed around the radius of the bubble. It means that when a discharge occurred around the previous discharge, most discharges occurred near the boundary of the bubble generated by d_{i-1}, and few discharges

occurred inside the bubble. This result verifies the influence of the debris particles concentrated at the bubble boundary generated by d_{i-1} and it made t_d shorter.

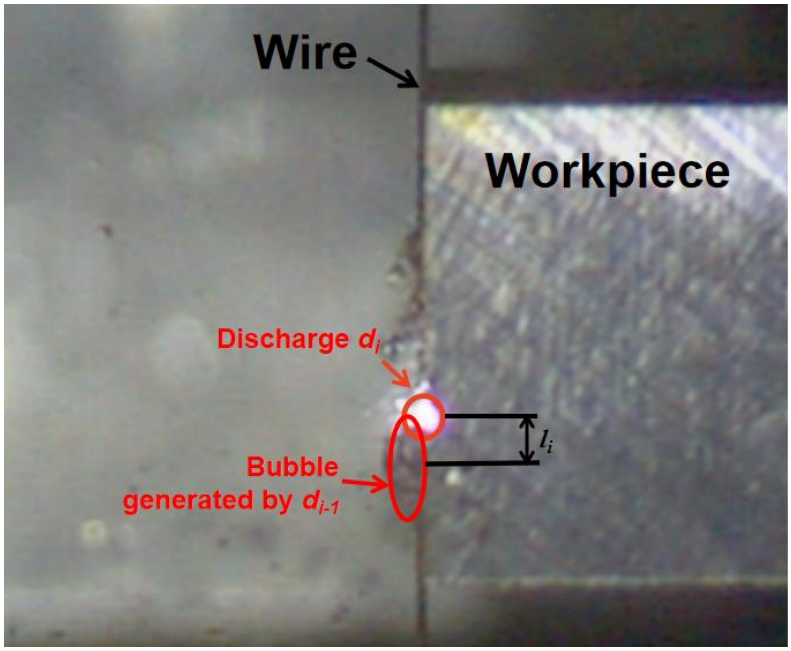

Figure 70. Distance between discharge location of d_i and the center of bubble generated by d_{i-1}.

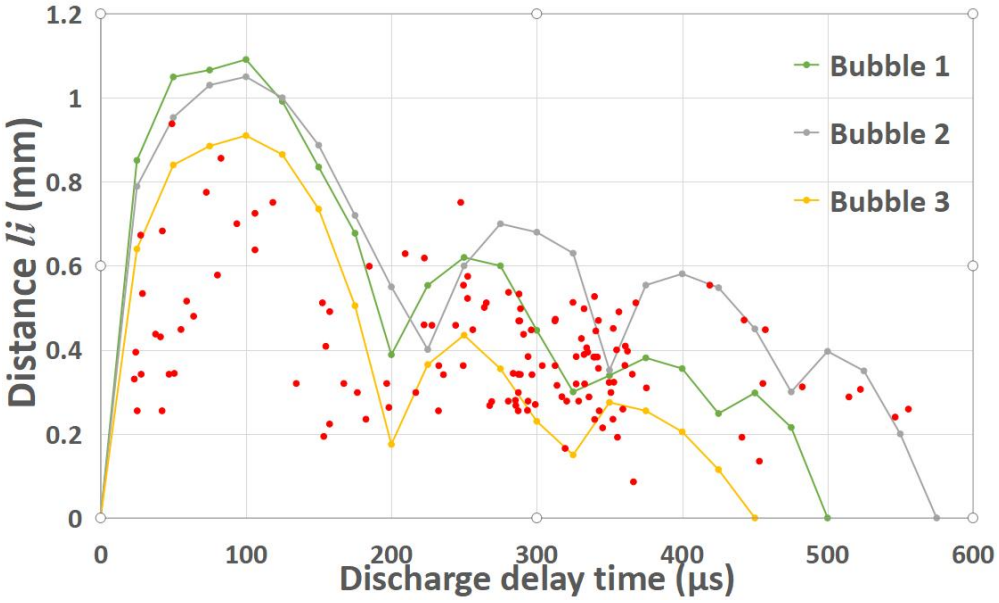

Figure 71. Comparison of Bubble radius and l_i.

The relationship between t_d and the discharge position was obtained in Figure 72. In that, all the discharges were divided into two groups. Group 1 is the discharges d_i which occurred within 0.5mm from d_{i-1}, and group 2 is the discharges d_i which occurred farther than 0.5mm from d_{i-1}. From Figure 72, it is found that in both groups, most

discharges occurred with a t_d between 200µs and 400µs and the percentage reaches about 65% because of the servo feed control. Moreover, it can be seen clearly that the percentage in group 1 was higher than that in group 2 when t_d was shorter than 200µs, coinciding with the first bubble oscillation cycle. On the contrary, when t_d was longer than 500µs the percentage in group 1 was lower than in group 2, which coincides with the time of the bubble collapse. In group 1, the percentage of discharges d_i with a t_d shorter than 200µs is 26.9%. Whereas this percentage of group 2 decreases to 12.9%. This means during the first oscillation of the bubble, some more discharges occurred under its influence. Then, in terms of the part of discharge whose t_d was longer than 500µs, the difference in percentage between group 1 and group 2 is 13.7%. It means when t_d was longer than 500µs, the discharge occurred mostly at a location farther than 0.5mm from d_{i-1}. It can be learned that after 500µs, with the disappearance of the bubble generated by d_{i-1}, its influence on d_i also disappeared.

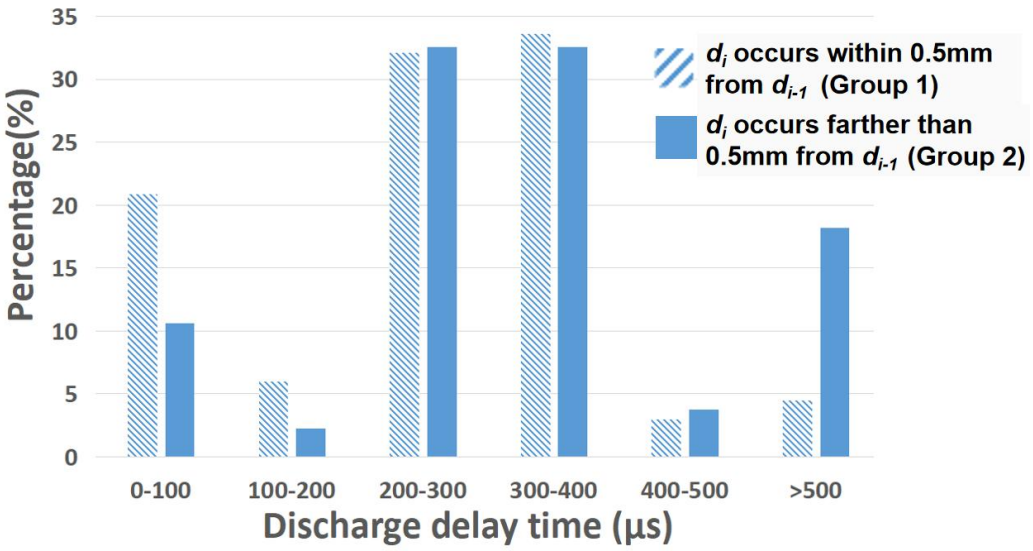

Figure 72. Comparison of t_d.

The relationship between t_d and the undischarged probability was plotted and as shown in Figure 73, the whole curve can be divided into 4 zones. In zone 1, the undischarged rate decreased very fast in the first 100µs, which is the duration of bubble expansion. The bubble expansion process generated more debris emitted from the working gap, and in this process, the discharge probability increased. When the bubble shrunk between about 100µs and 200µs as shown in zone 2, the influence of the bubble on discharge occurrence decreased. Then, most discharges occurred in zone 3 with a t_d between about 200µs and 400µs because of the servo feed control. After that, with the bubble dissipation, the influence of the bubble on discharge occurrence became less. As a result, the decrease of undischarged rate became very slow in zone 4.

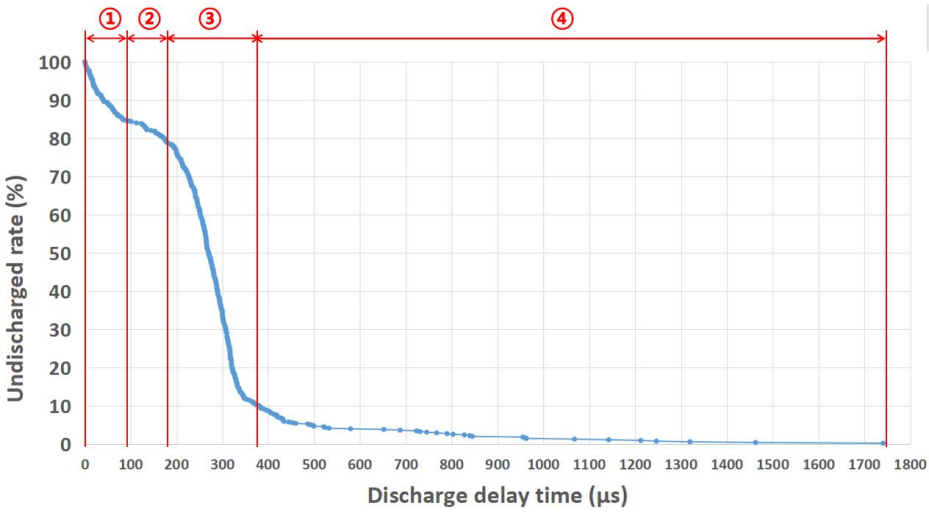

Figure 73. Relationship between the undischarged rate and t_d.

For further exploring the influence of bubble expansion on t_d, the same experiment was finished under peak discharge currents of 50A and 100A. After the image processing, the bubble oscillation process is shown in Figure 74 and the bubble oscillation of peak discharge of 150A was also plotted for comparison. It is found that with a lower peak discharge current the first bubble oscillation cycle is shorter, and the bubble size is smaller. In addition, under the peak discharge currents of 50A, 100A and 150A, the end times of the first bubble expansion are 50μs, 75μs and 100μs, respectively.

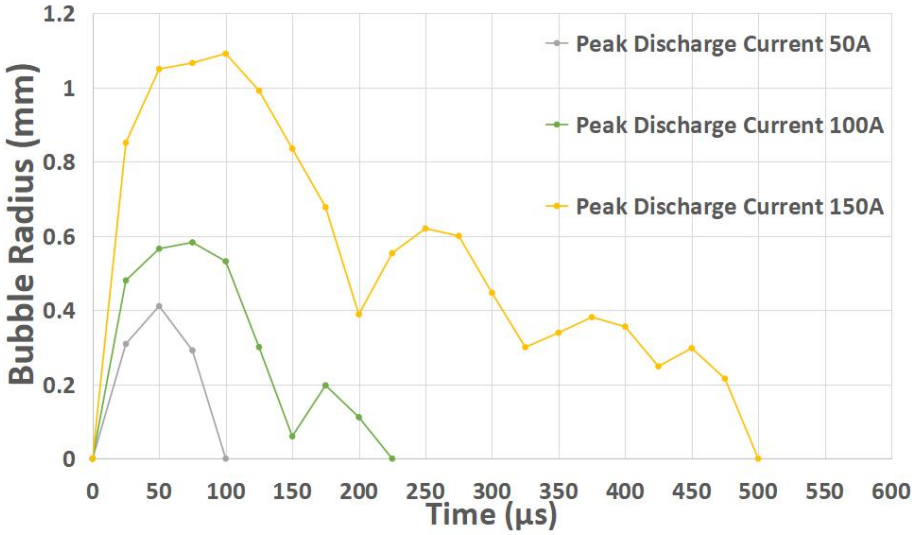

Figure 74. Oscillation of bubbles under different gap voltage.

Then, the relationship between t_d and the undischarged rate under each kind of peak discharge current was plotted in Figure 75. In that, the end time of the first bubble expansion was also marked out. It is found that, under all the conditions, in the period of the first bubble expansion the undischarged rate decreased very fast. In other words,

more discharges occurred in the process of bubble expansion. This result can verify again the influence of the bubble expansion on the discharge occurrence, and it can be explained by the effect of the debris particles concentrated at the bubble boundary that can make t_d shorter.

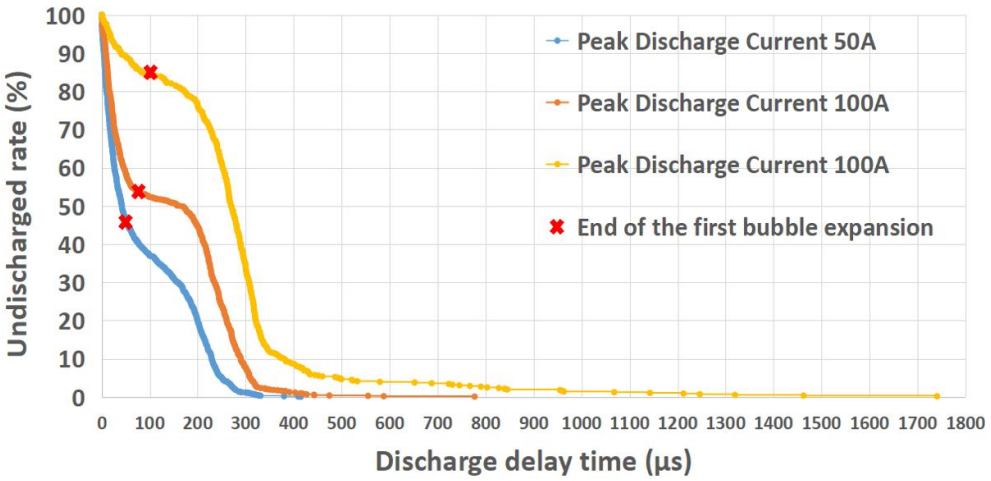

Figure 75. Relationship between the undischarged rate and t_d under different peak discharge currents.

III.4. Conclusions

For studying t_d in WEDM in-depth, several experiments on both single discharge and continuous discharges were carried out. Based on the experimental results, the following conclusions can be drawn:

- Through the single discharge experiment, it was learned that g, surface roughness and Q_f can affect t_d. It was found that an increase in g or a smoother workpiece surface made the discharge delay time larger. With a higher Q_f, the discharge delay time increased. With higher Q_f, the average position of the wire is farther from the initial position. In other words, the higher Q_f made g larger, and therefore longer t_d values were obtained.

- Through the observation by the high-speed video camera in the continuous discharges experiment, discharge location was successfully detected through grayscale analysis of photos gotten from the high-speed video camera. The probability that d_i occurs within 0.5mm from the location of d_{i-1} is the highest and is 14.1% higher than that of the random model. If there is a sufficiently large number of discharges between two discharges, the distribution tends to be random.

- When discharges occurred around the previous discharge, most discharges occurred near the boundary of the bubble generated by d_{i-1}, and few discharges occurred inside the bubble. This verifies the effect of the debris particles concentrated at the bubble boundary can reduce t_d.

- By comparing the bubble oscillation cycle and the relationship between the discharge delay time and the undischarged rate, it is found that more discharges occurred in the process of bubble expansion. This fact verifies the influence of the bubble expansion on the discharge occurrence, and it can be explained by the effect of the debris particles concentrated at the bubble boundary on t_d.

Chapter IV: Exploration of material removal in WEDM

IV. EXPLORATION OF MATERIAL REMOVAL IN WEDM

Material removal is an important aspect in the field of WEDM. Because of the uncertain position of the spark and the short ignition time, the details of the WEDM process are difficult to analyze. Among them, the understanding of material removal in WEDM is an interesting research topic. In WEDM, material removal is realized based on the huge number of craters forming on the workpiece. It is very important to understand the process of crater forming and the influence of parameters on this process. This chapter will do the exploration through collecting various data on different kinds of craters under different situations of surface roughness and gap width. Simultaneously, a thermal model of a single crater was developed for further understanding of the forming of a crater in detail.

IV.1. Introduction

Focusing on crater forming is a promising way to further understand material removal in WEDM. In general, the plasma channel between the wire and the workpiece takes shape after reaching the breakdown point in the process of machining. After that the produced heat transfers into the workpiece to make the material melt and even evaporate which leads to material removal. This process still needs to be studied including the heat partition and the influence of various machining parameters. Therefore, combining experiments and simulation with realistic experiments was selected as an approach to get a better understanding of this process.

In this chapter, several aspects will be introduced. In Section IV.2, for exploring the generation of the single crater and consecutive craters, various experiments were finished to obtain single craters and consecutive craters under different machining conditions. Through the observation of these gotten craters, it is known that the percentage of continuous craters on a rough surface is lower than on a flat surface. In addition, it was found that on a flat surface, the center of consecutive craters always appears on the rim of the previous crater. Furthermore, according to the observation results of single craters, it was observed that some roughness peaks appeared around the first crater. This surface profile made the consecutive discharge easier to take place on the rim of the first crater. Whereas for the single crater on the rough surface, it made not evident those roughness peaks. So the consecutive craters did not often appear on the rough surface.

In Section IV.3, the dimension of the single crater was further explored. Under different surface roughness and gap width, several experiments were finished to collect the

single crater, and then the observation of crater dimension was done. As a result, it was found that a rougher surface makes the crater volume smaller. In addition, in terms of gap width, results showed that the crater volume drastically reduced with the increase in gap width.

Next in Section IV.4, to better understand heat conduction and try to provide a deeper insight into crater formation, numerical models were built with the different surface situations and different machining parameters. Simultaneously, by relating the simulation results and the data of the real crater, some important parameters were gotten. According to that, with the reduction of surface smoothness, both the radius of the plasma channel and the fraction of total heat transfer to the workpiece decreased. Finally, some conclusions were presented in Section IV.5.

IV.2. Exploration of single crater and consecutive craters

For obtaining the clear single crater and consecutive craters, a fundamental experiment was built on ONA AV35 Wire EDM machine (CuZn37 0.25mm diameter brass wire). In that, AISI D2 was chosen as workpiece material and the property of this material is shown in Table 10. To produce individual craters, finding the critical point of the first few of sparks becomes indispensable. As the experimental principle that is shown in Figure 76(a), firstly, the gap between the wire and the workpiece was controlled at 1mm, and then gradually the wire approached the workpiece until the first few sparks occur. Figure 76(b) and Figure 76(c) respectively show some craters on flat and rough surfaces. In addition, the whole experiment included two parts, one was realized on a flat surface, and the other one was on a rough surface (Table 11).

T (K)	293.15	473.15	673.15
T_m (K)	1694.15		
ρ (kg/m^3)	7700	7650	7600
MOE (Mpa)	210000	200000	180000
λ (W/m·K)	2000	2100	2300
C (J/kg·K)	460		

Table 10. The property of AISI D2.

Flat (ground) surface	Roughing cut
R_a(μm): 0.46	R_a(μm): 2.60
R_z(μm): 3.59	R_z(μm): 15.27

Table 11. Initial part surface roughness for the experiments.

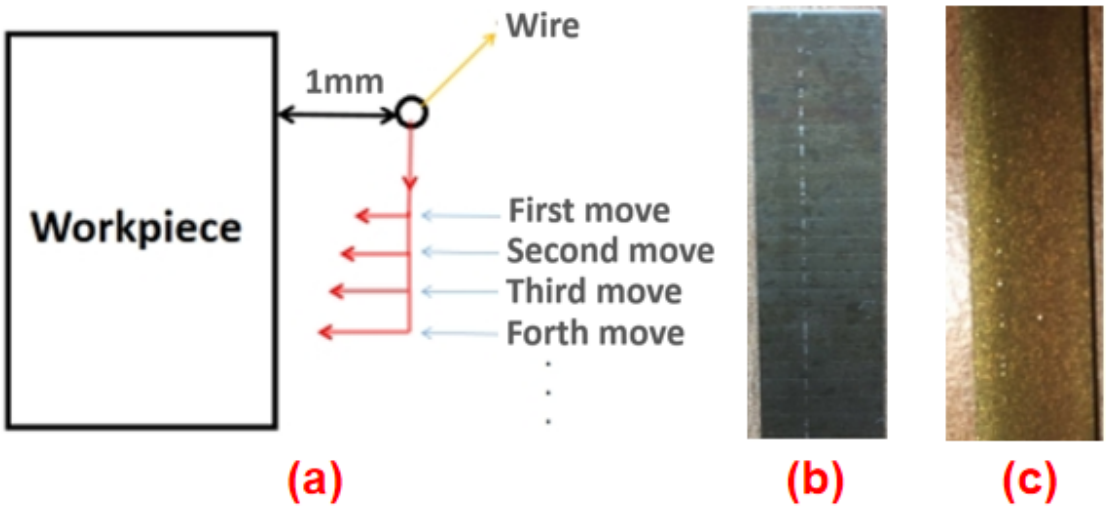

Figure 76. (a) Top view of the experimental principle; (b) Crater on flat surface; (c) Crate on rough surface.

Firstly, in the condition of the flat surface, the thickness of 20mm, 50mm, 150mm and 250mm of the workpiece was adopted in this experiment. The parameters used for these experiments are shown in Table 12.

h (mm)	20	50	150	250
I (A)	5	5	5	5
t_{off} (µs)	7	12	21	30
F (N)	18	18	18	18
U_o (V)	80	80	80	80
U_s (V)	52	52	52	52
g (µm)	51	62	69	78
f (mm/min)	10	12	13	13
Q_f (L/min)	16	16	16	16

Table 12. WEDM parameters as taken from the table of the ONA AV35 WEDM machine.

After that, the surface which includes a few craters was observed by the Leica DCM 3D machine (Figure 77). Finally, the craters were classified into 4 kinds: the single crater (Figure 78), two consecutive craters (Figure 79), three consecutive craters (Figure 80), and a few cases of more than three consecutive craters. Through the observation of these measurements, the profile geometry of the crater was always rendered as a circle or oval. Therefore, the craters can be marked out approximately in red. The number of different kinds of craters was also respectively counted in Table 13.

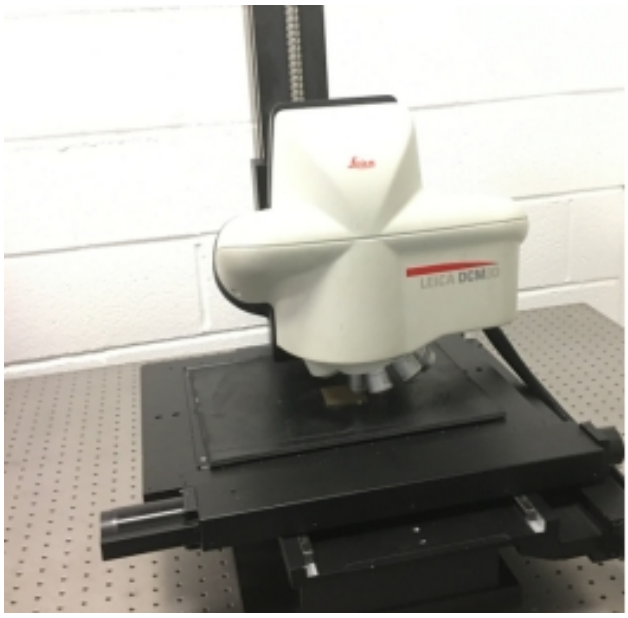

Figure 77. Leica DCM 3D.

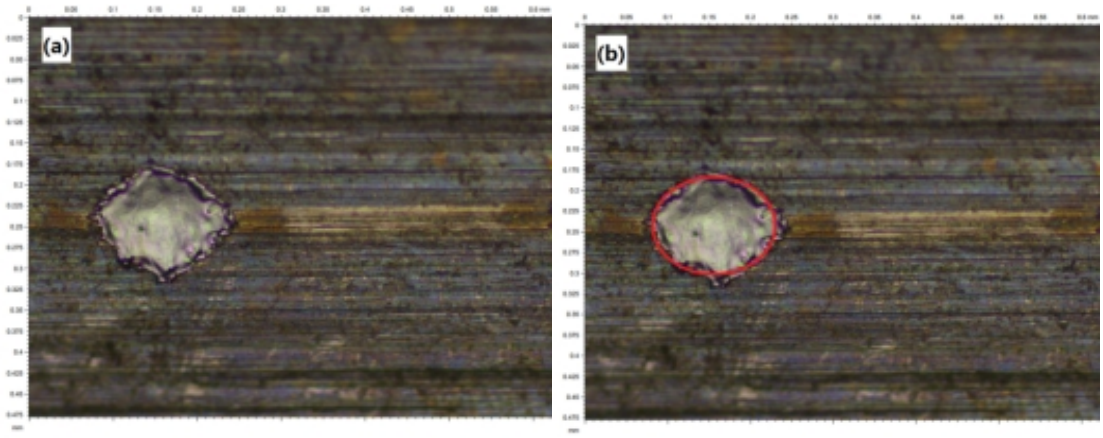

Figure 78. The single crater: (a) Original image; (b) After marked out.

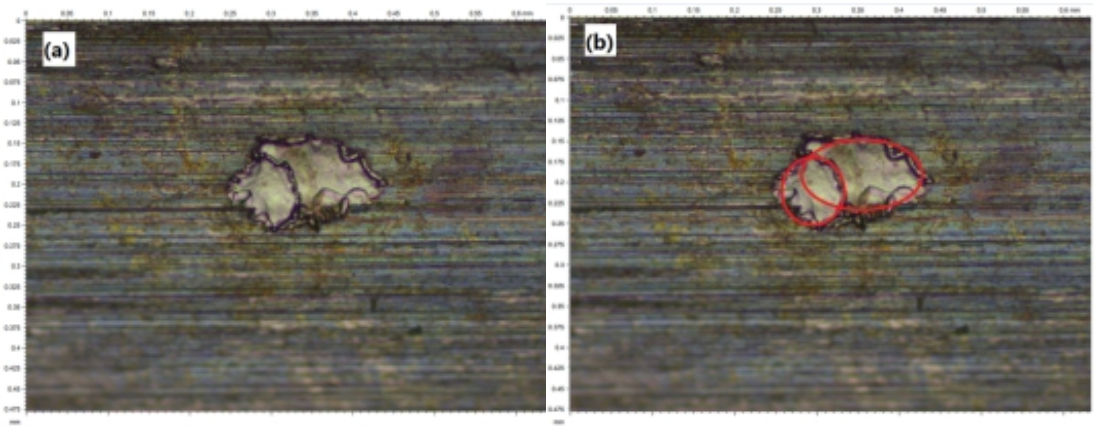

Figure 79. Two consecutive craters: (a) Original image; (b) After marked out.

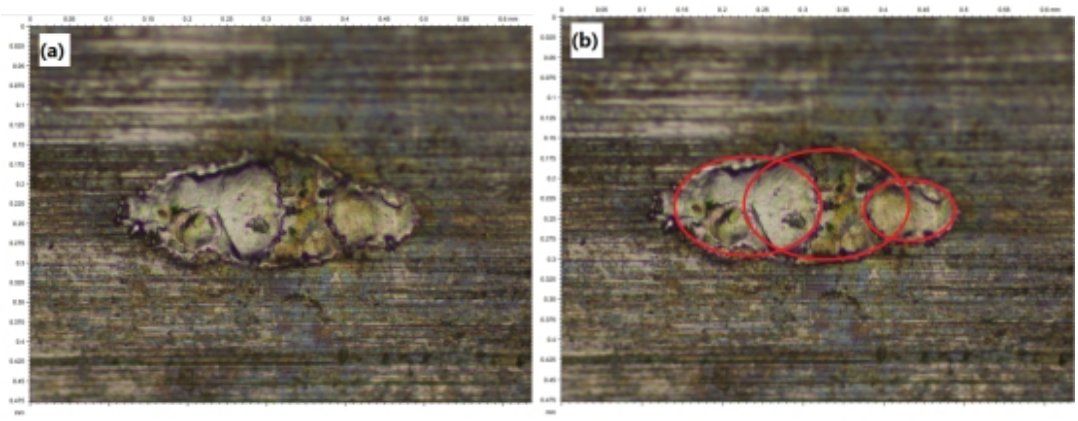

Figure 80. Three consecutive craters: (a) Original image; (b) After marked out.

***h* (mm)**	20	50	150	250
Total crater	21	52	112	196
Number of times of 2 consecutive craters	2	1	13	18
Number of times of 3 consecutive craters	2	3	6	13
Number of more than 4 consecutive craters	0	3	2	6
Percentage of consecutive craters (%)	47.6	46.1	46.4	52.0
D_c (μm)	101-131	97-169	74-177	144-153

Table 13. Crater statistics on the flat surface.

For getting the corresponding rough surface, firstly, the workpiece was cut horizontally with the same technology as in the previous experiment (Table 12). After that, the rough surface was cleaned with alcohol, and then the same procedure which was used for getting craters on the flat surface was repeated. Same as before, the crater was observed with the Leica DCM 3D. In this case, there were only two kinds of craters, one was the single crater (Figure 81) and the other one was two consecutive craters (Figure 82). The statistics of different thicknesses are recorded in Table 14.

***h* (mm)**	20	50	150	250
Total crater	43	31	74	105
Number of times of 2 consecutive craters	2	2	2	4
Percentage of consecutive craters (%)	9.3	6.45	5.4	7.6
D_c (μm)	50-110	72-128	76-111	78-113

Table 14. Crater statistics on the rough surface.

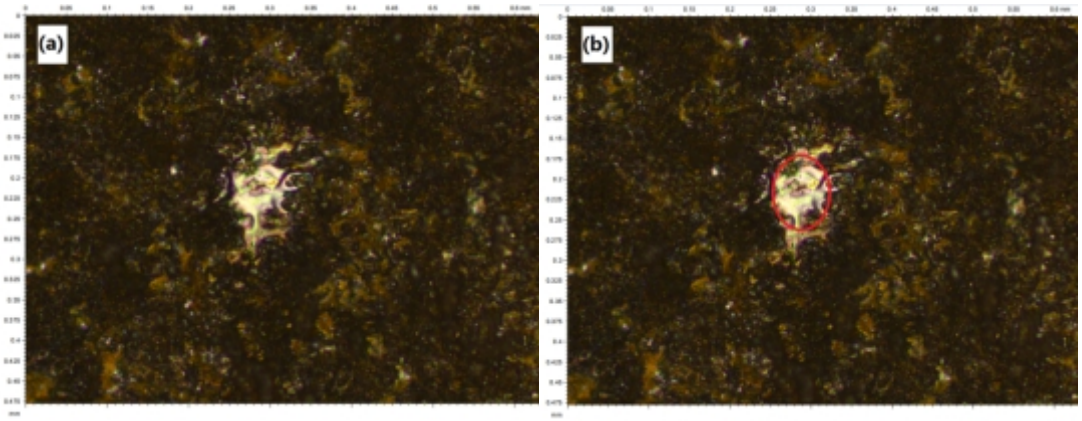

Figure 81. The single crater: (a) Original image; (b) After marked out.

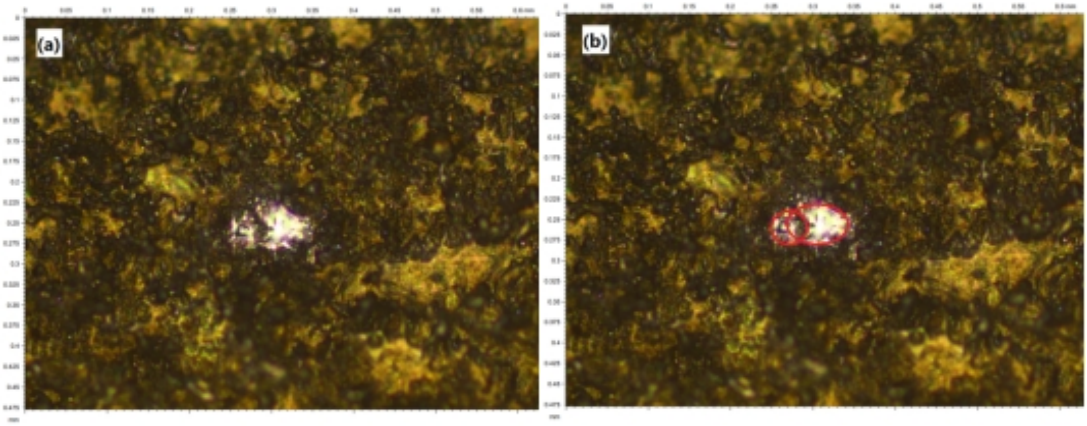

Figure 82. Two consecutive craters: (a) Original image; (b) After mark out.

By contrasting craters on the flat surface and the rough surface, the crater diameter on the rough surface was generally smaller than that on the flat surface. Moreover, on the flat surface, existed three consecutive and four consecutive even more than four consecutive craters, but on the rough, they can not be found. And also, the percentage of the consecutive crater was further lower on the rough surface than on the flat.

Further insight into the role of roughness peaks can be gained by looking at the cause of the formation of consecutive craters. For doing so, a single crater was scanned as shown in Figure 83. The experiment corresponded to a single discharge on the flat (ground) surface. A rim of melted and not removed material was clearly present on the periphery of the crater. The rim height can be as much as 8µm in the experiments, which is a value similar to measured crater depth. Figure 84 shows the morphology of two consecutive single craters when occurring on a flat surface. The diameters of the craters in this example are 127µm (first crater) and 114µm (second crater) respectively. Consecutive craters are, in all cases, smaller in diameter than the first single crater on the flat surface.

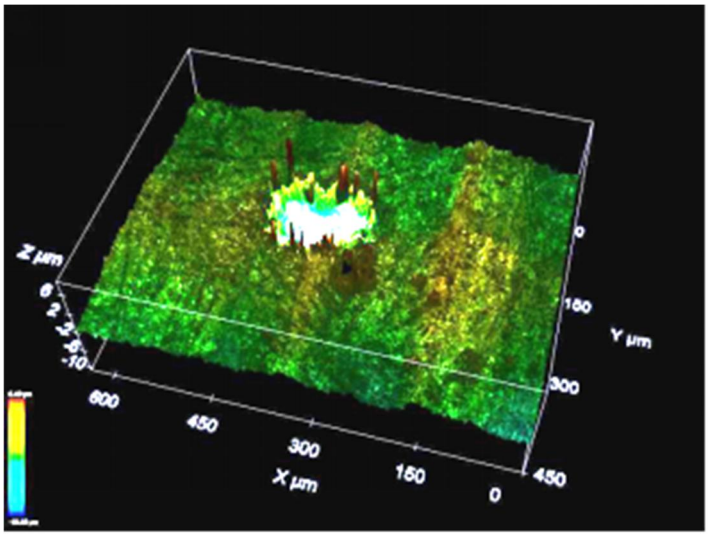

Figure 83. The rim generated by the single discharge on a ground surface (R_a 0.46µm, R_z 3.59µm). Rim height can be as much as 8µm.

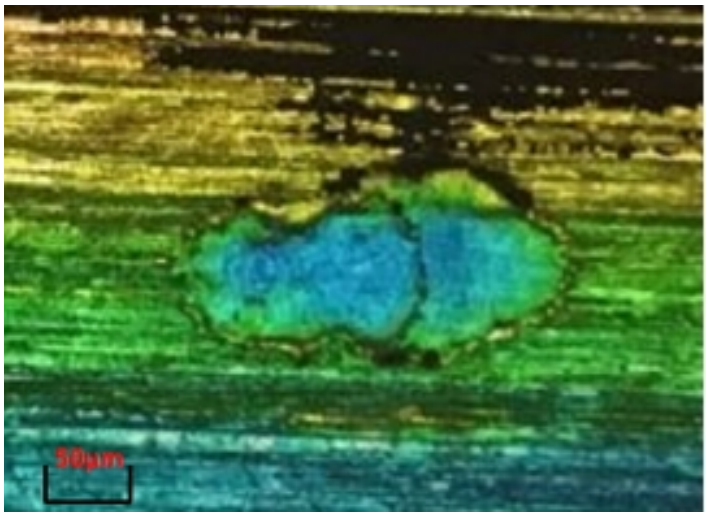

Figure 84. The occurrence of two consecutive single craters on a ground surface.

Figure 85 shows the crater generated by a single discharge occurring on a surface WEDM'ed in conditions of roughing cut. The occurrence of consecutive discharges on the flat and the rough surface was measured. In the case of a flat surface, in 47% of the cases, consecutive discharges concentrated on the rim of a previous crater were observed. In the case of the rough surface (WEDM roughing cut), the percentage decreases to 18%. Although these values are higher than those provided by Kitamura [21], the observed trend is similar, probability of discharge concentration being clearly lower when discharge occurs on a rough surface. Through the 3D scanning of a single crater on a rough surface, the rim of the crater is not so obvious as that on a flat surface. As said above, the rim of a previous crater affects largely the single discharge location in WEDM on a flat surface, but this effect becomes less important on a rough surface because of the presence of multiple peaks and valleys on the surface.

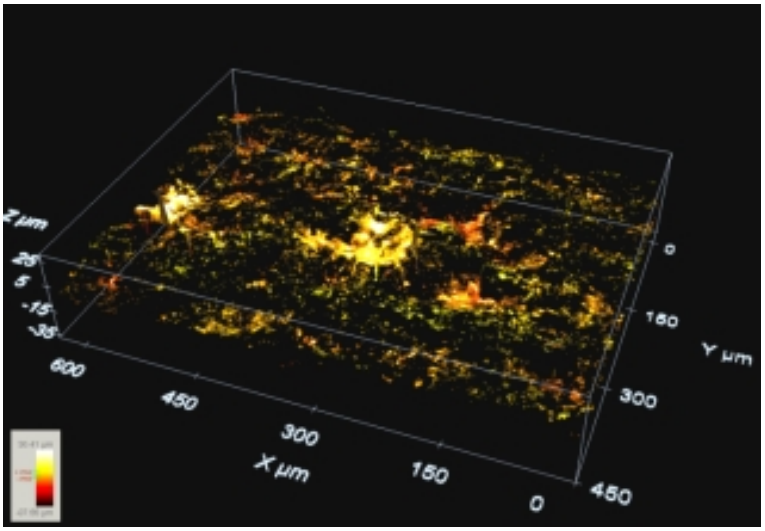

Figure 85. Single crater on a WEDM'ed surface (roughing cut, R_a 2.60µm, R_z 15.27µm).

IV.3 Experimental observation of single crater dimension

IV.3.1 Experimental set-up

Because the removal capacity of the WEDM process is largely influenced by gap contamination and width, single discharge experiments can be used to clarify some aspects that cannot be directly obtained from the continuous WEDM process. As explained in the literature review, little or no information is available about the single discharge experiments. A set of experiments involving the single discharge was carried out to achieve a deeper insight into crater geometry and removal capacity per discharge. The objective of the experiments was to obtain data about the influence of gap width, part surface roughness and discharge current on crater diameter and depth (d_c). Experiments, therefore, occur under conditions in which flushing is excellent and gap contamination is very low because the wire is not surrounded by the machined kerf.

Table 15 shows the WEDM settings used in the experiments. Part material was AISI D2 tool steel. CuZn37 wire of diameter 0.25mm was used. Conditions correspond to the first roughing cut (h=50mm) in the ONA AV35 WEDM machine where experiments were conducted. Using the parameters of the first roughing cut, single discharge experiments varying theoretical gap width (g) and part surface roughness as described in Table 16 were carried out. In all and each of the experiments, at least 10 craters were machined. Three different parts with increasing surface roughness were prepared: a ground flat surface; a WEDM'ed surface using parameters of with twice trim cut (parameters given also in Table 15); and a WEDM'ed surface using the

parameters of roughing cut. The values of R_a and R_z for each surface are given in Table 16. Two levels of theoretical gap width (as given by the position of wire guides) were used, which means a total of 6 experiments. Craters were studied following the same method in the previous section.

WEDM Parameters	Roughing cut	1st Trim cut	2nd Trim cut
***I* (A)**	5	5	3
U_o (V)	80	100	90
U_s (V)	52	48	10
***f* (mm/min)**	12	10	10
t_{on} (ms)	2	2	2
t_{off} (ms)	12	9	1
***h* (mm)**	50		
Q_f (L/min)	16		

Table 15. Electrical parameters for single discharge WEDM experiments.

Flat (ground) surface	Trim cut	Roughing cut
R_a(µm): 0.46	R_a(µm): 0.81	R_a(µm): 2.60
R_z(µm): 3.59	R_z(µm): 5.92	R_z(µm): 15.27
***g* (µm)**		
10	20	

Table 16. Gap width and initial part surface roughness for the experiments.

IV.3.2 Influence of part surface roughness

Table 17 collects the results of single discharge crater measurement for the different values of part surface roughness (as given by R_z) and different theoretical gap width values, in terms of crater diameter (D_c), depth (d_c) and crater volume (V_c) (assuming spherical cap crater). Average values and standard deviations are presented in Table 17.

A first look at the results reveals a noticeable influence of part surface roughness on crater dimensions. A flat surface on which the presence of peaks is scarce produces larger crater diameters. A similar trend is observed in the experiments with theoretical gap widths of 10µm and 20µm. In both cases, the average crater diameter is larger than 100µm.

g (µm)	R_z (µm)	D_c (µm)		d_c (µm)		V_c (µm^3)
		average	STD	average	STD	average
10	3.59	106	16.2	7.7	1.3	35648.49
10	5.92	105.7	27.7	4.8	0.7	23168.42
10	15.27	97.5	21.6	5.1	1.2	21255.18
20	3.59	104	21	6.8	0.9	34725.21
20	5.92	102	21.8	5.4	0.9	23603.25
20	15.27	87	16.1	6.3	1.6	20505.93

Table 17. Crater dimensions vs part initial roughness and theoretical gap width.

For the same gap width, an increase in R_z from 3.59µm to 5.92µm leads to a reduction in crater depth (d_c), and therefore to a considerable reduction in crater volume, about 35% no matter the value of gap width. The crater diameter shows no variation in this case. However, when further increasing peak height up to 15.27µm, crater diameter is reduced by approximately 18% (97.5µm in the case of gap width 10µm, 87µm in the case of gap 20µm). This trend is observed both with gap widths of 10µm and 20µm. As a consequence, when comparing the single discharge on the flat surface and the single discharge on a WEDM'ed surface obtained using conditions of roughing cut, crater volume is reduced by as much as 40%.

IV.3.3 Influence of gap width

From the results in Table 17, it can be deduced that, on one hand, an increase from 10µm to 20µm does not produce a relevant variation in crater dimensions. On the other hand, surface roughness imposes stronger boundary conditions on heat partition than those imposed by gap width. However, as explained by Kojima [25], a larger gap width results in a larger plasma channel diameter, and therefore in reduced heat flux to the electrodes. A longer plasma channel can also increase energy losses toward the dielectric, reducing thus heat conduction toward workpiece and wire electrodes.

As explained before, the above experiments have been performed under conditions in which flushing is excellent and gap contamination is very low, because the wire is not surrounded by the machined kerf. This is the reason why very small values of theoretical gap width can be set (10µm and 20µm). These values are very far from the realistic values of WEDM industrial practice. Therefore, in this section analysis of the influence of gap width will be addressed. Since during actual practice discharges occur on a surface where WEDM craters have already been generated, the comparison will be carried out using the experiments corresponding to WEDM roughing cut (this is, the initial surface roughness R_a 2.60µm, R_z 15.27µm). Using the same electrical

parameters as given in Table 15, different values of gap width can be achieved by cutting different part thicknesses. Table 18 collects the values of part thickness and the corresponding values of gap width (as given by machine tables) during the new set of experiments.

***h* (mm)**	***g* (µm)**
NA (Single discharge, rough surface)	10
NA (Single discharge, rough surface)	20
20	51
50	62
150	69
250	78

Table 18. Theoretical gap width values in the experiments.

Because the WEDM process is stochastic, results from single discharge experiments were compared with the average removal capacity per discharge during WEDM under industrial conditions. This can be obtained by using Eq.24, where $V_{discharge}$ (µm ^{3}/discharge) is the average removal capacity per discharge, *h* is the part thickness (mm), *w* is kerf width (µm), *l* is the cutting length (mm) and *N* is the total number of discharges, all these variables directly measured during the experiments. Figure 86 shows the evolution of average removal capacity per discharge as a function of gap width.

$$V_{discharge} = \frac{h \cdot w \cdot l}{N} \qquad \text{Eq.24}$$

The results confirm and quantify for the WEDM process the findings by Kojima [25] in terms of a drastic reduction of crater volume (average removal capacity per discharge) associated with the increase in gap width. Within the range of industrial WEDM conditions (gap width between 50µm and 80µm), the differences are not so noticeable, the reduction in average crater volume between these conditions being no larger than 11%. However, when comparing crater volume for a gap width of 10µm (single discharge experiments) and a gap width of 80µm (continuous WEDM, *h*=250mm), the reduction in average crater volume becomes as high as 36%. It must be taken into account that surface roughness and electrical settings are similar in this set of

experiments, and therefore, the variation can only be attributed to gap width variation.

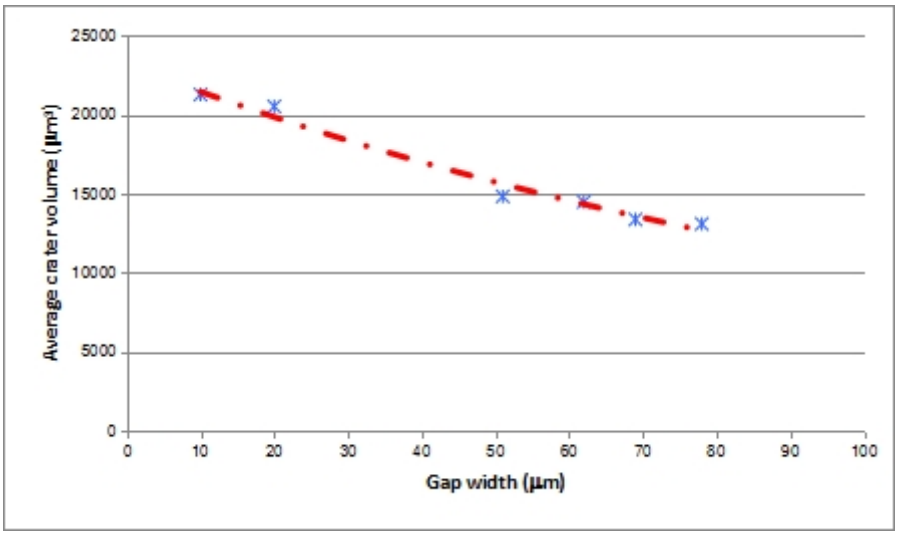

Figure 86. Average removal capacity per discharge vs gap width (discharge surface roughness corresponding to roughing cut, R_a 2.60µm, R_z 15.27µm).

At the sight of the results, it can be concluded that both gap width and part surface roughness impose strong boundary conditions on heat partition that must be taken into account in any fundamental study of the process. In order to better understand heat conduction and try to provide a deeper insight into crater formation, in the following section thermal numerical simulation of a single discharge on the different types of surfaces is presented.

IV.4 Numerical simulation of single discharge in WEDM

To better understand heat flux conditions in the workpiece a transient thermal model for single discharge in WEDM was developed in ANSYS®. The actual rough surface (as WEDM'ed using conditions of roughing cut) was imported and meshed (Figure 87). Then, the thermal transient problem was solved on it to quantify the effect of part geometry on heat transfer.

Actual voltage and current signals were measured using a Tektronix 5034B high-frequency Digital Oscilloscope, a Tektronix ThDP0200 Differential Voltage probe and a PEM CWT1xR current probe. The assumption of a Gaussian heat source [37] as described by Eq.4 was adopted. In that, f_c is the fraction of heat to the workpiece (40% after Xia [37]), r determines the point of application, as given by Eq.25:

$$r = \sqrt{(x - x_0)^2 + (y - y_0)^2} \qquad \text{Eq.25}$$

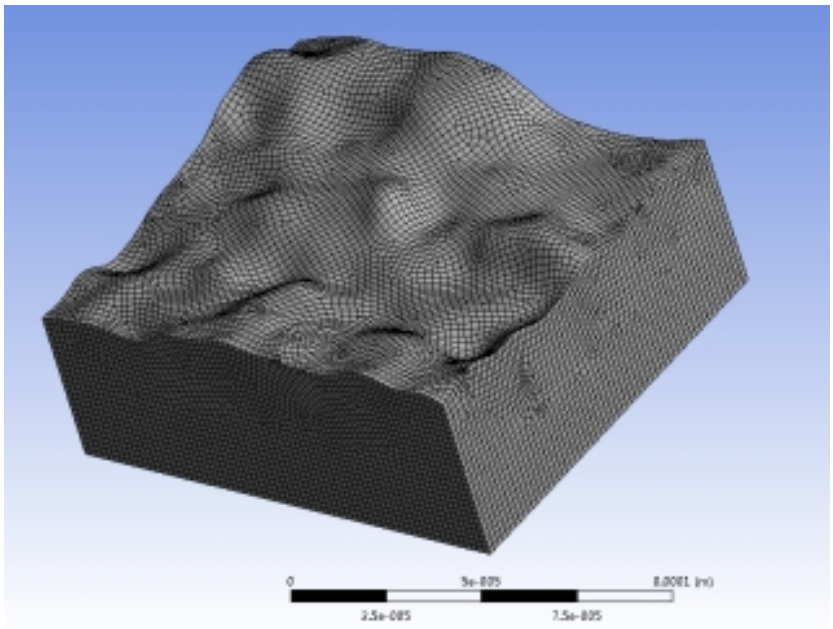

Figure 87. Meshing of the WEDM'ed rough surface for solving the thermal model.

The radius of the plasma channel is a difficult part of the simulation. Compared with others, the equation proposed by DiBitonto [30] is the only equation (Eq.6) that is based on the time change. Therefore, as a first approach, this time-dependent equation is used in the model. For a pulse time of 2µs, as taken from the machine table look-up, this equation yields a radius of plasma channel of 47.78µm. The latent heat of melting and evaporation has also been considered in the model. The properties of the AISI D2 steel used in the experiments are collected in Table 19 and were provided by the manufacturer of the steel.

T (K)	T_m (K)	ρ (kg/m3)	λ (W/m·K)	C (J/kg·K)
293.15	1658.15	7700	2000	460
473.15		7650	2100	
673.15		7600	2300	

Table 19. Thermal properties of AISI D2 tool steel.

Since flushing conditions during single discharge experiments were excellent, and following observations by Kitamura [21], who stated that it was assumed that most of the discharges occurred in liquid, water is chosen as the convection environment in the simulation of a single crater. Since in single discharge experiments flushing efficiency was very high, it was assumed that all the material above the melting temperature is removed from the workpiece during the simulations.

Figure 88 shows the geometry of the volume of material removed in the case of

simulation with the heat source applied on the flat (left) and rough (right) surfaces. Numerical results allowed quantifying the influence of the peaks over the spherical cap. Thus, the volume of the crater on the flat surface was 17438.98µm ^{3}, and the volume of material removed from the rough surface was 17910.52µm ^{3}. The difference was 2.6%. Crater dimensions were very similar in both cases, the diameter was 68µm in both simulations and the depth was 8µm on the flat surface and 7µm on the rough one. This means that, in terms of heat conduction, surface roughness did not impose noticeable differences on crater dimensions.

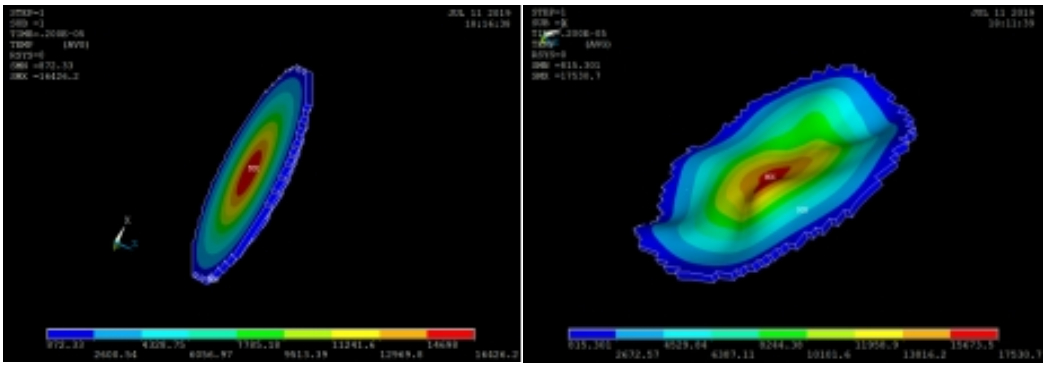

Figure 88. Simulation of the volume of part material removed. Heat source applied on flat (left) and rough (WEDM roughing cut, right) surfaces.

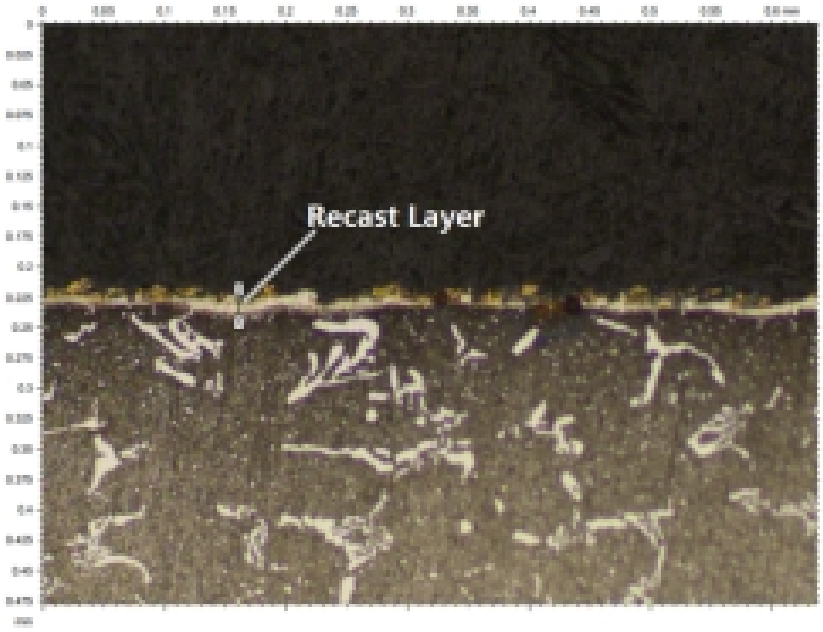

Figure 89. Recast layer after WEDM under the conditions of Table 15.

Simulation results can be compared with the experiments described in Section IV.2. Thus, when comparing numerical results with the actual removal capacity of the WEDM machine (Figure 86, gap width between 50µm and 80µm), it was noticed that simulation slightly overestimates crater volume (17910.52µm^3 in simulation, 13080-

14820µm^3 in actual WEDM). However, flushing efficiency in actual WEDM was far from 100%. The thickness of the recast layer was used to estimate flushing efficiency. Figure 89 shows a micrograph of a WEDM'ed surface (after polishing and metallurgical preparation) machined with the conditions of Table 15. Through Table 20, the average volume of recast parts produced by each discharge was calculated. The value was about 911.63µm^3.

***h* (mm)**	50
***l* (mm)**	6.77
N_{dis}	9211280
Thickness of the recast layer (µm)	12.4
Number of recast layer	2

Table 20. Measurement result of the recast layer.

Using this result, the actual crater volume from the simulation became 16998.89µm^3, which was very near to the value from the actual process. Therefore, it was concluded that reference values found in the literature for heat partition and radius of the plasma channel fitted very well with the actual conditions of discharge on a rough surface with gap width values of practical WEDM operation.

Surface	***g* (µm)**	**V_c(single discharge experiments, µm^3)**	**Deviation**
Flat (ground) R_a(µm): *0.46;* R_z(µm): *3.59*	10	35648.49	52.3%
WEDM, trim cut R_a(µm): *0.81;* R_z(µm): *5.92*	10	23168.42	26.6%
WEDM, roughing cut R_a(µm): *2.60;* R_z(µm): *15.27*	10	21255.18	20.0%

Table 21. Deviations between the results from the numerical model and single discharge experiments.

However, when comparing simulation results with single discharge experiments discrepancies became evident. Table 21 collected the results from the experiments and the deviations when compared with simulation results (rough surface as a reference, crater volume 16998.89µm^3). The deviations increased with a reduction of surface roughness and a reduction of gap width. In the case of single discharge experiments on a flat surface with a gap width of 10µm, crater volume as provided by

simulation was as much as 52.3% smaller than the actual average crater generated during the experiments. The deviation reduced to 26.6% in the case of discharges on the surface generated by two trim cuts, and a further reduction to 20% was observed when compared with discharges on the rough surface (WEDM roughing cut). By looking at Table 17, it can be seen that deviations were of the same order when the gap width increased to 20µm.

In order to get a deeper insight into the influence of surface roughness and gap width on the numerical values of the boundary conditions, simulations with different values of heat partition ratio f_c and radius of the plasma channel R_p (after 2ms) were performed using the numerical model. For simplicity, and since as shown above, the heat conduction problem was very similar on rough and flat surfaces, this latter was selected for the simulations. Table 22 gathers simulation results for combinations of values of R_p (after 2ms, 60µm, 70µm and 80µm) and f_c (60%, 70% and 80%).

		40% (Xia)	50%	60%	70%	80%
47.78um (Dibitonto)	V_c (µm³)	17438.98	20574.15	23461.97	25933.81	28621.36
	R_c (µm)	34	36	38	38	40
	d_c (µm)	8	8	10	10	10
60um	V_c (µm³)	17983.14	22238.79	26047.1	29566.88	32382.7
	R_c (µm)	38	40	42	44	46
	d_c (µm)	6	8	8	8	10
70um	V_c (µm³)	17831.4	22567.91	26982.95	31286.72	35063.42
	R_c (µm)	40	44	46	48	48
	d_c (µm)	6	6	8	8	8
80um	V_c (µm³)	16287.59	22392.08	27391.51	31398.87	35886.4
	R_c (µm)	42	46	48	50	52
	d_c (µm)	4	6	6	6	8
90um	V_c (µm³)	15288.13	20288.68	26590.71	31750.41	36190.89
	R_c (µm)	42	46	50	52	54
	d_c (µm)	4	4	6	6	6

Table 22. Crater dimensions from numerical simulation for different combinations of heat partition ratio (f_c) and radius of the plasma channel (model of discharge on a flat surface).

The results show that when single discharge experiments took place on a flat surface (values of gap width between 10-20µm), large increases in f_c and R_p explained the dramatic increase in crater volume. A good agreement was found for values of f_c between 70-80% and R_p between 70-90µm. For exploring the interrelation, a

polynomial surface fitting was carried out with Matlab. Finally, the following 3 equations (Eq.26, Eq.27, Eq.28) were obtained for expressing respectively the relation between V_c, R_c, d_c and f_c, R_p.

$$V_c = 7165 - 20540 \cdot f_c + 133.1 \cdot R_p + 9229 \cdot {f_c}^2 + 1380 \cdot f_c \cdot R_p - 5.169 \cdot {R_p}^2 - 7244 \cdot {f_c}^3 - 212.2 \cdot {f_c}^2 \cdot R_p - 3.771 \cdot f_c \cdot {R_p}^2 + 0.01429 \cdot {R_p}^3 \quad \text{Eq.26}$$

$$R_c = 8.02 + 47.51 \cdot f_c + 0.04237 \cdot R_p - 91.99 \cdot {f_c}^2 + 0.9016 \cdot f_c \cdot R_p + 0.002721 \cdot {R_p}^2 + 66.67 \cdot {f_c}^3 - 0.8134 \cdot {f_c}^2 \cdot R_p + 0.003045 \cdot f_c \cdot {R_p}^2 - 0.00004264 \cdot {R_p}^3 \quad \text{Eq.27}$$

$$d_c = 3.136 + 40.9 \cdot f_c - 0.1239 \cdot R_p - 69.38 \cdot {f_c}^2 + 0.3503 \cdot f_c \cdot R_p - 0.001185 \cdot {R_p}^2 + 33.33 \cdot {f_c}^3 + 0.01161 \cdot {f_c}^2 \cdot R_p - 0.002633 \cdot f_c \cdot {R_p}^2 + 0.0000133 \cdot {R_p}^3 \quad \text{Eq.28}$$

After refining the range of f_c (40%-80%) and Rp (47.78µm-90µm) with an interval of 0.01% and 0.01µm respectively all of the corresponding V_{ceq}, R_{ceq}, d_{ceq} were calculated with these 3 equations above. Apart from that, a useful parameter of error (E) (Eq.29) was adopted. In contrast with the data of the actual crater result (g=10µm) in Table 17, selected the minimal error (E(min)) and found out the corresponding f_c and R_p. The result of the calculation and the result of the comparison were shown in Table 23.

$$E = \sqrt{(V_{ceq} - V_c)^2 + (R_{ceq} - R_c)^2 + (d_{ceq} - d_c)^2} \quad \text{Eq.29}$$

From the data above in Table 23, it could be observed that the equation deviation was controlled at about 10%, therefore, the f_c and R_p can be used for further research. About the f_c and R_p comparison between different machining surface situations, through observing the change of f_c and R_p, with the worse surface situation, the change of plasma channel radius was 6.06µm but f_c reduced from 78.90% to 49.30%. In the preliminary conclusion, with the reduction of surface smoothness, the radius of the plasma channel did not make a big difference. Whereas the fraction of total heat

transfer to the workpiece presented a sharp decrease.

Surface situation	Flat (ground) surface	Trim cut	Roughing cut
f_c (%)	78.90	54.00	49.30
R_p (μm)	83.84	89.90	84.36
E(min)	0.91897	0.42412	0.00501
V_c (μm^3)	35648.49	23168.42	21255.18
V_{ceq} (μm^3)	35690.58	23169.38	21247.65
DEV_v (%)	0.11	0.004	0.04
R_c (μm)	53.00	52.85	48.75
R_{ceq} (μm)	52.61	47.90	45.92
DEV_R (%)	0.74	9.37	5.81
d_c (μm)	7.70	4.80	5.10
d_{ceq} (μm)	6.88	5.01	5.10
DEV_d (%)	10.65	4.38	0

Table 23. The calculation result of f_c and R_p and the equation deviation.

IV.5 Conclusions

For getting a deeper insight into the influence of surface roughness and gap width on crater dimensions in WEDM, a few experiments and thermal models were carried out in this chapter. Therefore, the following conclusions can be drawn:

- The diameter of the crater on the rough surface was typically smaller than that on the flat surface. Moreover, on a flat surface, the situation of three consecutive and four consecutive or even more than four consecutive craters was observed. Whereas, in terms of rough surface, there were few consecutive craters. Simultaneously, the percentage of continuous craters on a rough surface was lower than on a flat surface. In addition, on a flat surface, the center of consecutive craters always appeared on the rim of the previous crater. It was because around the first crater, there were some roughness peaks. And then, it made the consecutive crater easier to take place on the rim of the first crater. Whereas, as the roughness of the rough surface, it made not evident those roughness peaks around the first crater. As a consequence, the consecutive craters did not often appear on the rough surface.

- By increasing the R_z from 3.59μm to 5.92μm, compared to the same condition of gap width, the crater depth is reduced by approximately 35%. In this case, there was not a lot of change in crater diameter. However, when the peak

height further increased to 15.27μm, the diameter of the crater reduced by about 18%. Thus, when comparing a single discharge on a flat surface with that on a rough surface which was obtained by WEDM, the crater volume reduced by as much as 40%.

- The crater volume drastically reduced with enough increase in the gap width. Within the range of industrial WEDM conditions (gap width between 50μm and 80μm), the difference was not noticeable, and also, the average crater volume reduction under the change of these conditions was no more than 11%. However, through the comparison of the crater volume with a gap width of 10μm and a gap width of 80μm, the average crater volume changed clearly and the reduction can reach up to 36%.

- After building a thermal model to simulate the crater formation process in WEDM, comparing the numerical values of the boundary conditions between flat surface (R_a=0.46μm; R_z=3.59μm) and rough surface (R_a=2.60μm; R_z =15.27μm), the change of plasma channel radius was not more than 6.06μm. Whereas the fraction of total heat transfer to the workpiece occurred a sharp decrease from 78.90% to 49.30%.

Chapter V: Exploration of wire breakage in WEDM

V. EXPLORATION OF WIRE BREAKAGE IN WEDM

Wire breakage during WEDM has been a research topic of considerable interest for decades. Both the scientific literature and industrial patents proposed that the discharge accumulation could cause wire breakage in the WEDM process. For verifying this view, in this chapter, a complete thermal model considering both latent heat and flushing efficiency was developed. With this model, several simulations were performed, and by comparing the experimental result and simulation result, the heat partition to the wire was obtained. Then, the effect of heat accumulation in the wire was studied. Furthermore, the sparks before wire breakage were located and based on their location, the simulation of wire with craters was carried out. These findings allow for a more in-depth understanding of the effect of discharge accumulation on wire breakage.

V.1. Introduction

Special interest is focused on the heat flux towards the wire in order to further understand the wire breakage. During the WEDM processing process, wire breakage will reduce processing efficiency and affect the quality of processing. The study of wire breakage is essential in WEDM processing. Generally, the heat accumulation and the damage caused by the craters caused by continuous discharge on the wire are considered as the reason that causes the breakage.

In this chapter, the reason for wire breakage will be explored and further understood. Firstly, in Section V.2, the numerical model for the part of the wire is presented. By summarizing the models of researchers and exploring other essential elements of the thermal model, a more comprehensive and complete model was established. In this model, the heat source, the plasma channel radius, and the latent heat were taken into account.

In Section V.3, the precise heat partition to the wire was found based on the thermal model that was built in Section V.2. First of all, the wire with craters gotten after WEDM machining was capsuled and observed. From that, the damage percentage around the contour of the wire was calculated. Furthermore, the white layer also was studied through observation and the flushing efficiency was calculated. After this, the simulation of the single crater on the wire was carried out and the removal volume was obtained depending on different possible heat partitions to the wire. After comparing it with the real removal volume which is gotten from the experimental data, the precise heat partition to the wire was finally determined.

In Section V.4, the reason for wire breakage was discussed from two aspects. Firstly, heat accumulation in the wire was studied. Through comparing two kinds of t_{off}, it was found that, if all continuous discharges are adjacent, with a shorter t_{off} the heat accumulation in the wire is faster and the wire breakage occurs earlier. Then, with the aim of locating the position of several discharges just before wire breakage, a spark location method was presented and verified. With this, a wire breakage experiment was conducted and the position of 50 sparks just before wire breakage was obtained. Based on the numerical model that was introduced before, a simulation that can simulate the removal crater on the wire was done to restore the process of wire breakage. From the simulation results, the wire cross-section area reduction caused by the continuous adjacent craters was simulated. This kind of reduction makes the stress higher than the UTS of the wire and causes the wire breakage. Finally, the conclusions that gotten in this chapter were presented in Section V.5.

V.2. Numerical model

When studying the nature of the heat flux, it is important to consider the generation and growth of a plasma channel inside the dielectric medium, which will be addressed later in this chapter. Provided that the nature of the heat source is known, the heat flow can be essentially expressed as a three-dimensional transient heat transmission problem (Eq.17, given in partial derivatives), that needs to be solved, taking into account the boundary conditions of the problem. The solution of the equation implies certain assumptions, which have already been validated by previous researchers:

(1) Wire material properties are temperature dependent [48].
(2) Plasma channel can be considered a cylindrical column [48].
(3) Wire materials can be considered isotropic and homogeneous[44], [48].
(4) In the process of heat transfer, heat radiation is neglected [101].
(5) Despite the intrinsic stochastic nature of the WEDM process, all pulses are assumed as equal. In other words, pulse duration, voltage, and current are the same for all the discharges, and the occurrence of abnormal pulses is ignored[101].

As stated previously, modeling the Gaussian heat source which is shown in Eq. 4 was selected. R_p was assumed to be dependent on time. The previously mentioned work by Spur and Schönbeck [50] provides evidence to suggest that a time-dependent model could be more accurate for short on-times (about 2µs) such as those used in WEDM. Their results can be expressed using Eq.30:

$$R_p = (2e - 5) + 30.5t \qquad \text{Eq.30}$$

Figure 90 illustrates graphically the fundamentals of the thermal model, including the coordinate reference system and boundary conditions.

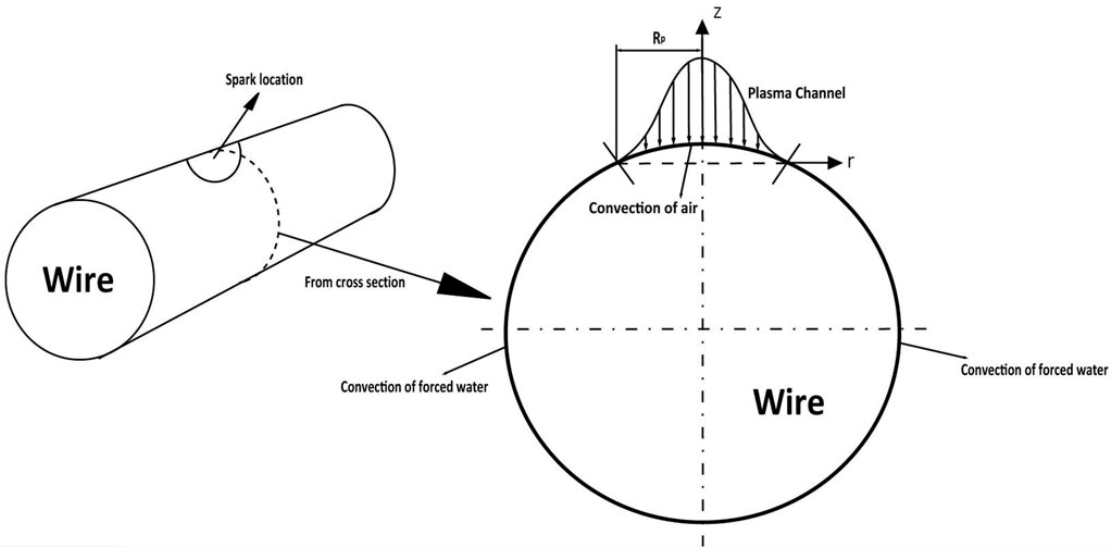

Figure 90. Heat transfer to the wire.

During the discharge process, boundary conditions are time-dependent: i) During on-time (which is approximately 2μs in commercial WEDM machines), part of the energy is transferred toward the wire through the plasma channel. Eq.31 expresses mathematically this part of the problem:

$$K_t \frac{\partial T}{\partial z} = Q(r) \qquad \text{Eq.31}$$

Hayakawa et al. [105] found that although the working gap was immersed in the dielectric liquid, it was mostly occupied by air bubbles. Therefore, during on-time inside the plasma channel, the assumption of convection in the air will be used. Outside the plasma channel, forced convection due to flushing of deionized water can be considered; ii) During off-time (as much as 5 times longer than on-time), forced convection acts over the complete modeling region. As explained above, the effect of heat loss by radiation is negligible. Eq.32 expresses heat transfer by convection:

$$\lambda \frac{\partial T}{\partial z} = h(T - T_0) \qquad \text{Eq.32}$$

Where λ is the thermal conductivity, h is the convection transfer coefficient (that depends on the described boundary conditions) and T_0 is the initial temperature.
Finally, attention must also be paid to the properties of the material. It is known that in the process of WEDM, the maximum temperature will be higher than the melting

point of the metal, and sometimes it could also even exceed the boiling point. Chen et al. [48] pointed out that the latent heat during the state change from solid to liquid and from liquid to vapor cannot be ignored. Therefore, in this work, the equivalent specific heat capacity of the material is optimized by Eq.33 and Eq.34, where C_p is the specific heat capacity in solid state, C_m and C_{ev} are respectively the equivalent specific heat capacity when the material is in the state of solid to liquid and the state of liquid to vapor. T_m and T_{ev} are the melting point and the boiling point respectively, T_{ref} is the ambient reference temperature, and L_m and L_{ev} are the latent heat in the process of fusion and evaporation.

$$C_m = C_p + \frac{L_m}{T_m - T_{ref}} \quad \text{Eq.33}$$

$$C_{ev} = C_m + \frac{L_{ev}}{T_{ev} - T_m} \quad \text{Eq.34}$$

V.3. Heat partition to the wire

V.3.1. Experimental and simulation set-up

Controlled experiments allow the extraction of relevant information from the numerical model. The experiments were carried out on an industrial ONA AV35 WEDM machine and the brass wire (Cu63%/Zn37%, UTS 960N/mm^2), with a diameter of 0.25mm was adopted. The workpiece material was Sverker21 tool steel which is widely used in the industry because of its high wear resistance [106] and the chemical composition is shown in Table 24. WEDM parameters were selected by machine table look-up and are those for roughing cut with a part thickness of 50mm. The complete set of parameters is listed in Table 25.

Element	Weight percentage
C	1.55
Si	0.3
Mn	0.4
Cr	11.8
Mo	0.8
V	0.8

Table 24. Chemical composition of Sverker 21.

Numerical simulation was then programmed in ANSYS. The thermal transient problem with the boundary conditions described in Section V.2 is solved using APDL, which was

also used to filter and calculate the elements whose temperature was higher than the melting point. For the simulations, the thermal properties of the wire are required, as displayed in Table 26.

WEDM Parameters	
U_o (V)	80
U_s (V)	50
f (mm/min)	12
t_{on} (µs)	2
t_{off} (µs)	12
F (N)	20
Q_f (L/min)	16

Table 25. Electrical parameters for single discharge WEDM experiments.

ρ (kg/m^3)	8160	
λ (W/m·^{o}C)	121	
C (J/kg·^{o}C)	at 20^{o}C (T_{ref})	377
	at 800^{o}C (T_m)	503.05
	at 1187^{o}C (T_{ev})	49156.90

Table 26. Thermal properties of brass.

V.3.2. Results of the experiment and simulation

WEDM experiments using the industrial conditions given in Table 25 were conducted to measure the average crater volume removed from the wire surface. After machining, the wires were collected for measuring their length. In order to increase the accuracy of the experiment, the procedure was carried out three times. The wire length of each experiment is shown in Table 27 and in that, the discharge number (N_{dis}) was recorded by the ONA AV35 WEDM machine. Furthermore, it is known that in the process of WEDM, each of the two electrodes melts, and the debris fills the gap. When the flushing stream takes away the debris it will also form part of that which adheres to the surface of the wire and workpiece, which is known as the recast layer.

For measuring the thickness of this layer, the cross-section of the wire with the crater needs to be observed. In this work, the used wire collected previously is fixed vertically and constructed as a resin capsule which is shown in Figure 91 (a). After polishing, the chemical attack is conducted with liquid ferric nitrate. For observing the capsuled wire with SEM, the surface of the sample should be converted to a conductor. Therefore, the Emitech K550X Sputter Coater was used to make an Au coat on the surface of the resin capsule.

	Experiment No.		
	1	2	3
N_{dis}	459671	507313	795565
l (mm)	6165	7191	10607

Table 27. Discharge number and collected wire length.

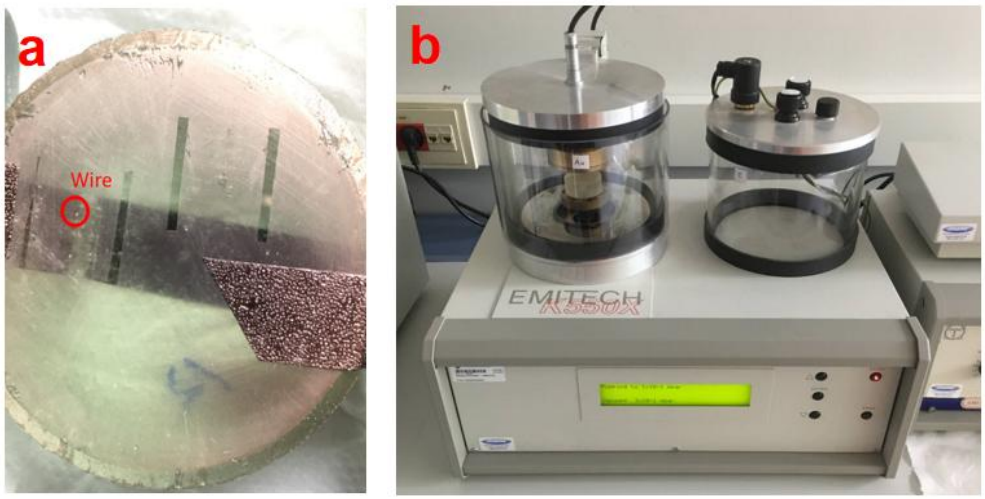

Figure 91. (a) Capsule for observing the cross-section of the wire; (b) Emitech K550X Sputter Coater.

The observation is then completed with the Hitachi S-3400N SEM. In Figure 92 the recast layer can be clearly recognized. Also, the composition of the recast layer was analyzed by X-ray diffraction and the result is shown in Table 28. From this result, it is known that in the composition of the recast layer on the wire, there are few elements from the workpiece and this result coincides with the research work on the recast layer on the workpiece in WEDM which was finished by Newton et al. [107]. They found that in the composition of the recast layer on the workpiece, there was only 0.06% of copper and no zinc which are the elements from the wire. Therefore, in the study of the recast layer on the wire, the impact of the workpiece can be ignored.

In addition, the profile of the wire is obtained as shown in Figure 93 (a). According to the part without craters, the original profile of the wire was marked as Figure 93 (b). It is clear that discharge occurs at approximately 68% of the total wire perimeter. Further, the area without damage is obtained with the ImageJ software tool. Using this, the removed area (A_{remove}) and the recast layer area ($A_{recastlayer}$) can be measured as shown in Table 29. Furthermore, in each experiment, the removal volume of each discharge ($V_{discharge}$) can be established using Eq.35. In addition, the flushing efficiency (PFE) was calculated as 44.98% through Eq.36.

$$V_{discharge} = \frac{A_{remove} \cdot l}{N} \quad \text{Eq.35}$$

$$PFE = \frac{A_{remove}}{A_{remove} + A_{recastlayer}} \quad \text{Eq.36}$$

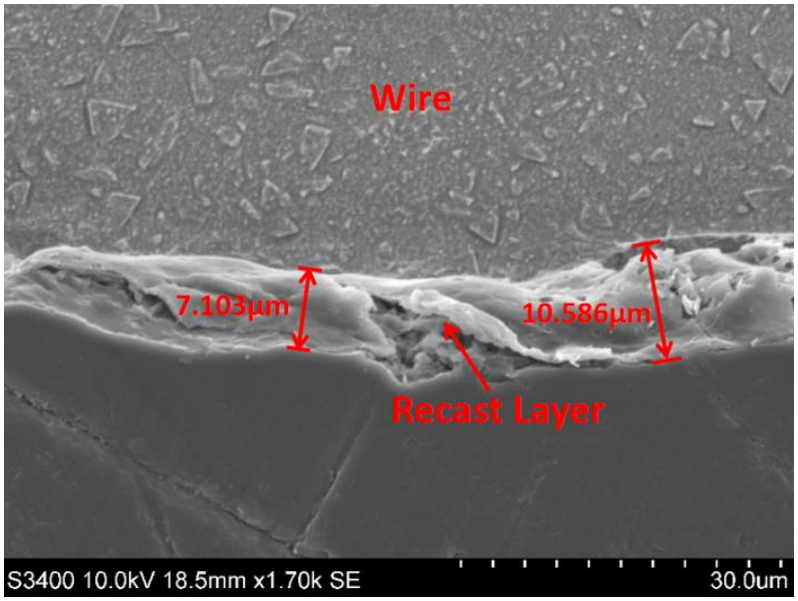

Figure 92. SEM observation of the recast layer on the wire.

Composition of recast layer	
Cu	62.76%
Zn	34.67%
O	2.46%
Fe	0.11%

Table 28. Composition of recast layer on the wire.

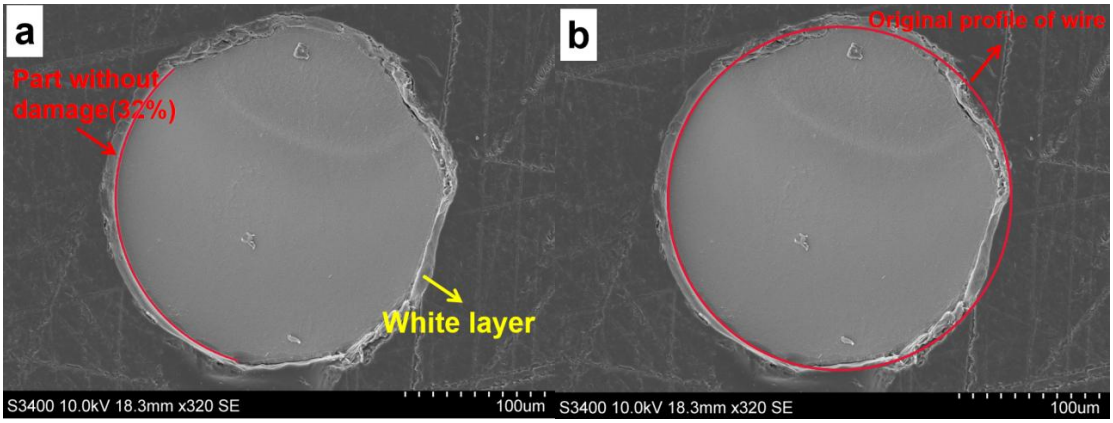

Figure 93. (a) Observation of the wire cross-section; (b) Marked original profile of wire according to the part without crater.

	Experiment No.			Average	STD
	1	2	3		
A_{remove} (µm²)	4906.25	4708.50	4880.18	4831.64	107.44
$A_{recastlayer}$ (µm²)	6136.79	5730.32	5860.34	5909.15	111.55
$V_{discharge}$ (µm³)	65801.48	66741.49	65065.80	65869.59	839.92

Table 29. Result of measurement and crater volume.

Once the value of crater volume on the wire is known, the experimental results can be compared with numerical simulations, so that it is possible to obtain a value of heat partition ratio to the wire. The transient thermal problem was then solved on the wire using ANSYS. Under the assumption of a cylindrical plasma channel, a similar value of R_p can be used for both the heat source on the workpiece and the wire electrode. Following experimental results by Spur and Schönbeck [50] a value of R_p of 81µm after 2µs will be used. In addition, a value of heat partition to the workpiece of 40% was taken from Xia et al. [37]. This latter value helps set the feasible variation range of f_c, which was established below 60%. The validity of the above values for WEDM conditions reported in the literature has recently been confirmed in the previous chapter. Mathematical simulations were then carried out using the numerical model described in Section V.2. The results for crater volume removed from the wire per discharge were plotted in Figure 94 for the different values of f_c. It can be observed that in the range of 40% to 50% of f_c, the volume of the crater increases from 51933.21µm³ to 72441.65µm³. To obtain a more precise estimate of this value to match the real crater obtained previously, the curve fitting tool in Matlab was applied. The inverse fitting allows for achieving a precise value for the heat partition ratio to the wire. The value obtained is 46.74%. After this, a verifying simulation was conducted with this percentage and the error was 0.53%, as calculated by Eq.37. In that, $V_{simulation}$ is the removal volume obtained from the simulation.

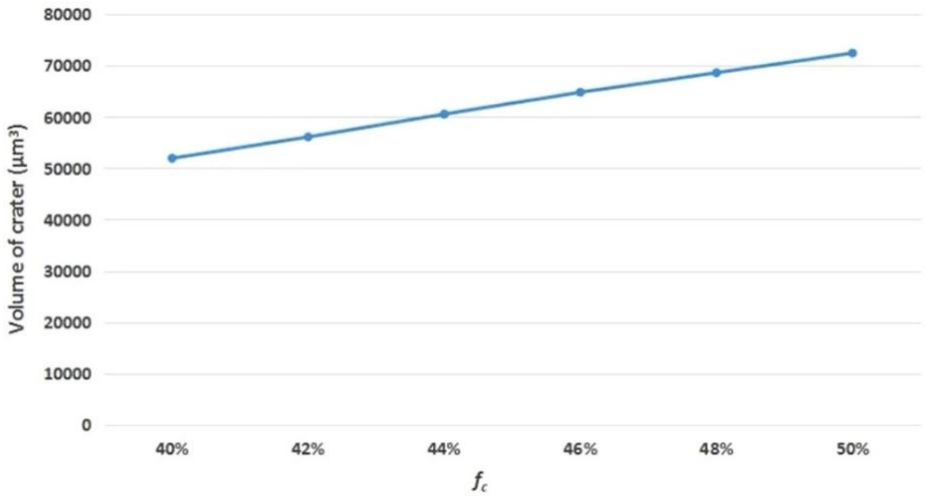

Figure 94. Simulation of crater volume on the wire.

$$E = \left| \frac{V_{discharge} - V_{simulation}}{V_{discharge}} \right| \cdot 100\% \quad \text{Eq.37}$$

V.4. Exploration of the reason for wire breakage

For exploring the reason for wire breakage, the local accumulation of discharges must be taken into account. Local accumulation of discharges is attributed to the impossibility of effectively removing the debris generated by one or several previous discharges. The origin of this effect can be related to causes such as too short t_{off}, which hinders debris removal and wire cooling. Thus, local conductivity in a region close to the previous discharges then becomes higher, and the probability of a new discharge occurring in that region increases. The hypothesis is that, if discharge accumulation in a region is sufficiently high, the local thermal load on the wire increases in such a way that the active cross-section of the wire is reduced. If this reduction is sufficiently high, the section of the wire cannot withstand the axial force, and, consequently, ductile failure of the wire occurs. For verifying this hypothesis study on thermal accumulation and wire damage after continuous adjacent discharges were studied.

V.4.1. Study on the thermal accumulation in wire

To study the thermal acclimation in the wire, two kinds of experiments were finished. Firstly, the experiment was done with t_{off}=4µs while keeping constant the other electrical parameters shown in Table 25. This experiment led to wire breakage and it has been named Case 1. Then, another kind of experiment under the conditions presented in Table 25 (t_{off}=12µs, stable cutting) was carried out and it has been named Case 2. In both experiments, the occurrence of trains of short circuits was measured by the ONA AV35 WEDM machine.

As the result, in Case 2, from the total number of trains of short circuits, only 11.5% corresponded to more than 3 consecutive short circuits. Whereas in Case 1, it was found that the percentage of trains with more than 3 consecutive short circuits increased up to 38%, which is 3.3 times larger than that of Case 1. In view of the above considerations, it was decided to use the thermal model described in Section V.2 to analyze the temperature evolution inside the wire in two different unstable WEDM situations:

- Case 1: simulation of the extreme reduction of t_{off}=4µs (remaining parameters as shown in Table 25). In this case, local discharge accumulation is due to too short pulse interval.

- Case 2: simulation of roughing cut in non-sealed conditions using machine-table parameters (that is, conditions given in Table 25, t_{off}=12µs), local discharge concentration being due to inefficient flushing. Many users avoid wire breakage in this case by increasing the pulse interval.

To explore the thermal accumulation caused by consecutive and adjacent discharges, supposing all continuous discharge is adjacent, a total number of 24 and 32 discharges on the periphery of the wire were simulated respectively for Case 1 and Case 2, that is, a total of 188µs for Case 1, and 324µs for Case 2. As shown above in Figure 93 (a), in both cases discharges are simulated on approximately 68% of the total wire perimeter and it was decided to apply the heat source consecutively at these locations, which are explained in Figure 95 (a) and Figure 95 (b). Clearly, other hypothesized locations could be used, but this was selected as a representative estimation. Finally, as shown in Figure 96, a 3D thermal model on wire has been defined.

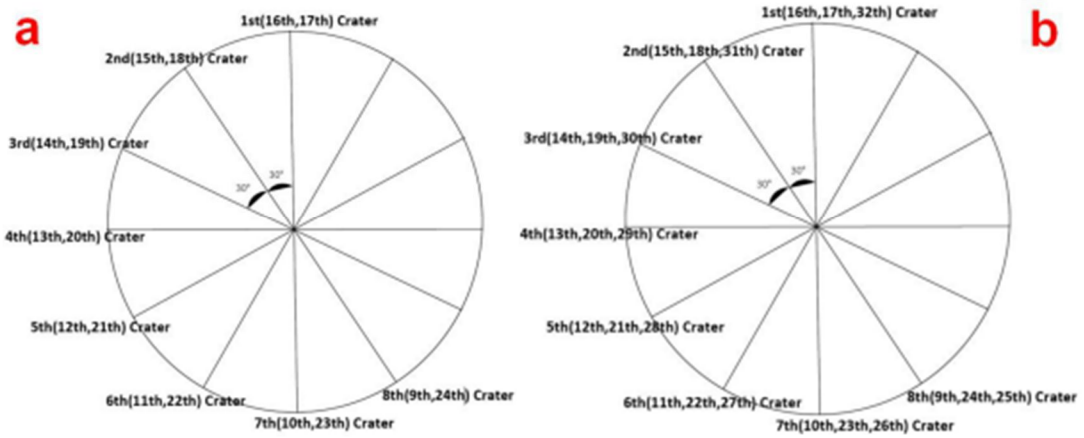

Figure 95. Hypothesis used for discharge location in thermal simulations. (a) Case 1; (b) Case 2.

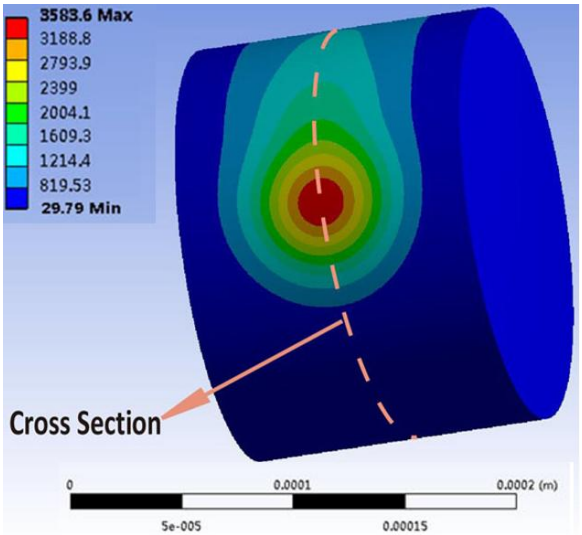

Figure 96. 3D thermal model on the wire.

Figure 97 represents the thermal field inside the wire for Case 1. The isotherm of 800°C is represented, and the area of the cross-section always below that temperature is represented in dark blue color. The simulation results for 10 and 32 accumulated discharges were plotted. After 10 consecutive discharges, only 22.42% of the total cross-section was damaged. Continuing with the simulation, it can be observed that after 188µs (32 discharges), as much as 93.95% of the total cross-section has endured temperatures of over 800°C.

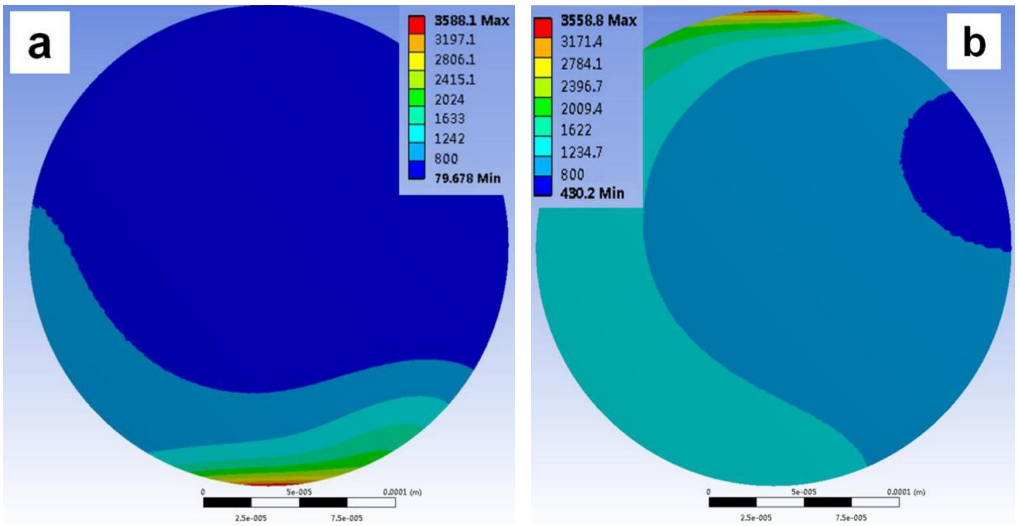

Figure 97. Under t_{off}=4µs, thermal field on the cross-section of the wire after accumulation of (a)10 consecutive discharges; (b) 32 consecutive discharges.

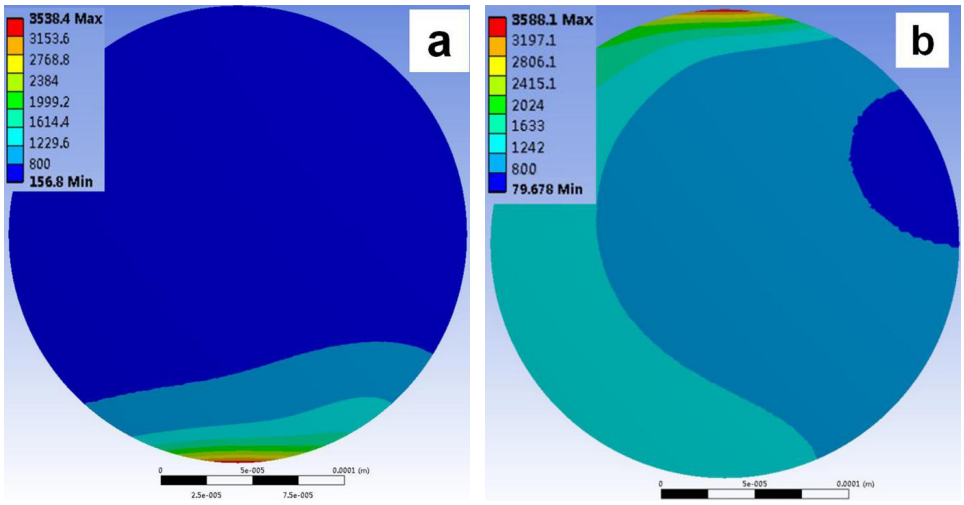

Figure 98. Under t_{off}=12µs, thermal field on the cross-section of the wire after accumulation of (a)10 consecutive discharges; (b) 24 consecutive discharges.

Regarding Case 2, Figure 98 shows the cross-section of the wire after 10 discharges and 24 discharges respectively. As in the previous case, the area of the cross-section below the isotherm of 800°C is also represented in dark blue color. It can be observed

that 14.69% of the total cross section was damaged after 10 consecutive discharges, which then increases to 89.89% after 24 discharges so that the whole process lasts 324µs.

Figure 99 shows the plot of the damaged area (%) as a function of time for both cases. For a tensile force of 20N applied on the wire, and the ultimate tensile strength of the wire of 960MPa, the percentage of damaged area that produces ductile failure is 42.46%. This is represented in Figure 76 by the horizontal line.

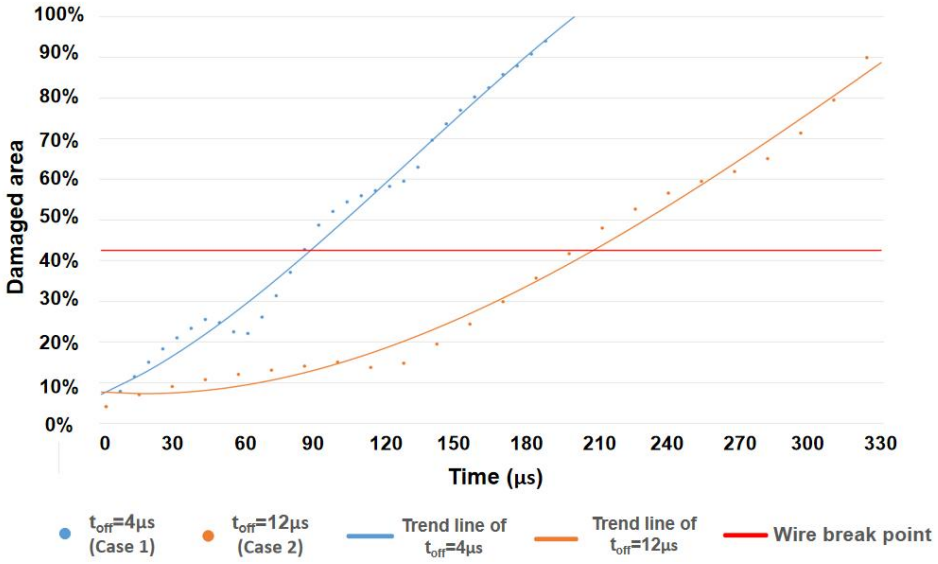

Figure 99. Damaged area of case 1 and case 2.

As expected, in both cases the damaged area increases rapidly and in Case 1 (t_{off}=4µs, blue plot), this area exceeds the limit break point after approximately 90µs. For Case 2 (t_{off}=12µs, orange plot) this situation occurs after more than 200µs, which is over two times more than that in Case 1. This clearly implies that in the same given unit of time, a higher number of craters will lead to a more rapid accumulation of heat. To further verify the influence of heat accumulation on wire breakage, the position of several discharges just before wire breakage needs to be found.

V.4.2. Experimental set-up for wire breakage and determining spark position

For further exploring the effect of discharge accumulation on wire breakage, the position of the sparks that cause the wire breakage should be located. In the work of Kunieda et al. [81], they proposed that with the change of spark position, the part of wire included in the upper circuit and lower circuit respectively will also change. Since the wire is modeled as the resistance in the circuit, it means that the current value is distinct depending on the spark position. Also, later in the work of Boccadoro et al. [15] they used this method for monitoring the machining contour. As shown in Figure 100

when the discharge occurs the wire can be seen as divided into two parts (upper part & lower part). Meanwhile, two closed circuits (upper circuit & lower circuit) are formed which include respectively relative parts of the wire.

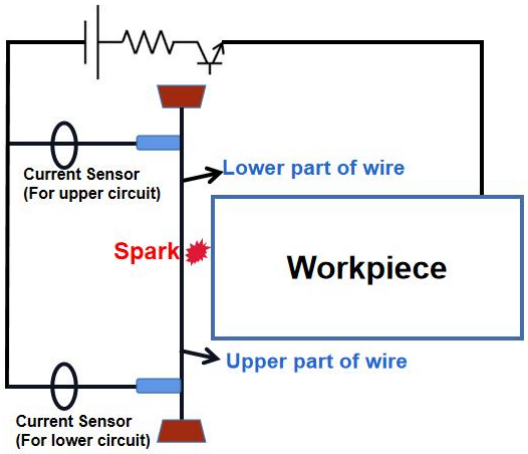

Figure 100. Schematic diagram of spark position.

In order to verify the feasibility of this method, several experiments were carried out on the ONA AV35 WEDM machine with the machining parameters listed in Table 30. In this experiment, a Sverker21 sheet workpiece of 2mm thickness was selected. As shown in Figure 101 (a), the distance between two nozzles (H) was 70mm and 7 values for placement heights of the sheet workpiece (H_1) were chosen. Meanwhile, two CWT Rogowski current transducers were used for detecting the current of the upper circuit and the lower one (Figure 101 (b)), and a Tektronix 5034B Digital Oscilloscope for collecting current signals.

WEDM Parameters	
I (A)	10
U_o (V)	80
U_s (V)	50
f (mm/min)	12
t_{on} (µs)	2
t_{off} (µs)	50
H (mm)	70
H_1 (mm)	0, 10, 20, 30, 40, 50, 60
F (N)	20
Q_f (L/min)	16

Table 30. WEDM machining parameters for spark locating experiment.

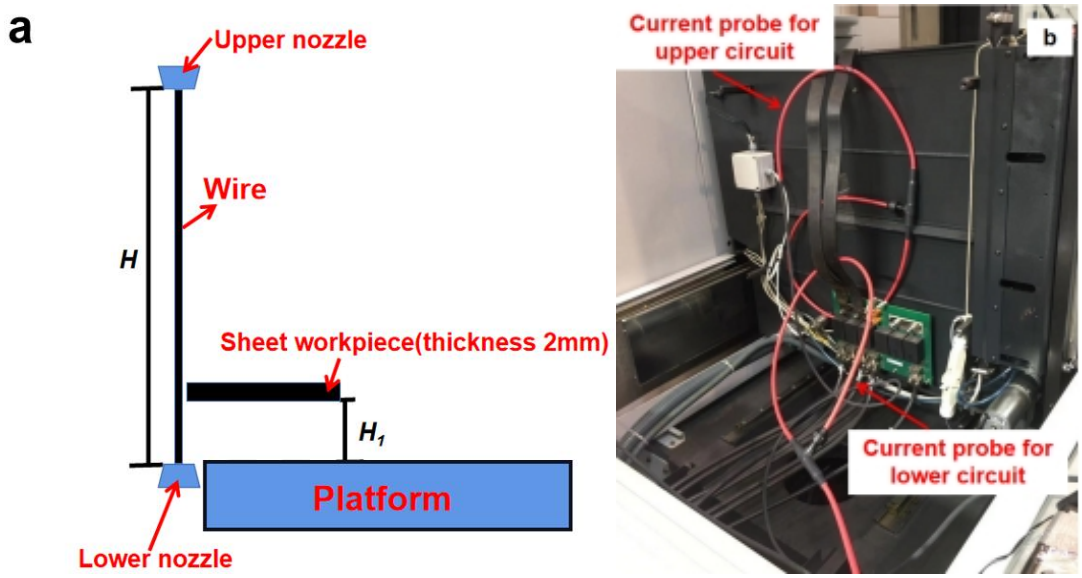

Figure 101. (a) Schematic diagram of experiment; (b) Current probes set on WEDM machine.

After the measurement of 400 discharges at each height, the relation (k) between the upper circuit current (I_{upper}) and the lower circuit current (I_{lower}) was calculated by Eq.38. As shown in Figure 102, the relation between k and H_1 is relatively close to linear. Therefore, the linear tendency equation is obtained as Eq.39. For further verifying the accuracy of this equation, another two kinds of H_1 (28mm & 42mm) were selected to do the same experiment and for each H_1 the relation k of 100 sparks was obtained. With Eq.39, the prediction of H_1 is calculated and the result is shown in Table 31. Finally, it can be estimated that the accuracy of this method is about 2mm.

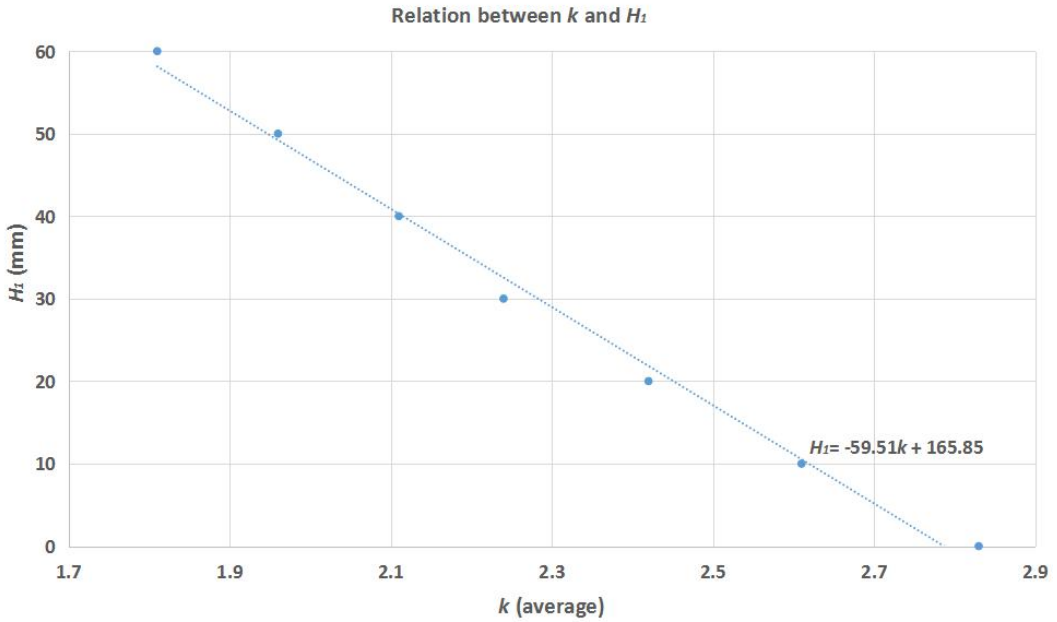

Figure 102. Experiment result of the relation between k and H_1.

$$k = I_{lower}/I_{upper} \quad \text{Eq.38}$$

$$H_1 = -59.51 \cdot k + 165.85 \quad \text{Eq.39}$$

H_1 (mm)	Average prediction of H_1 (mm)	STD
28.00	29.80	1.79
42.00	41.50	1.06

Table 31. Result of prediction.

Then another experiment with the workpiece thickness of 50mm was finished and for easier getting the wire breakage, 2μs of t_{off} was adopted. In the process of cutting, I_{upper} and I_{lower} were also measured. Finally, the last 50 sparks before the wire breakage were picked out to further process. The relation k was calculated by Eq.38 and then H_1 was predicted by Eq.39. As a result, the position of the last 50 discharges before wire breakage is shown in Figure 103. These results show that 34% of discharges concentrated between 2mm and 4mm.

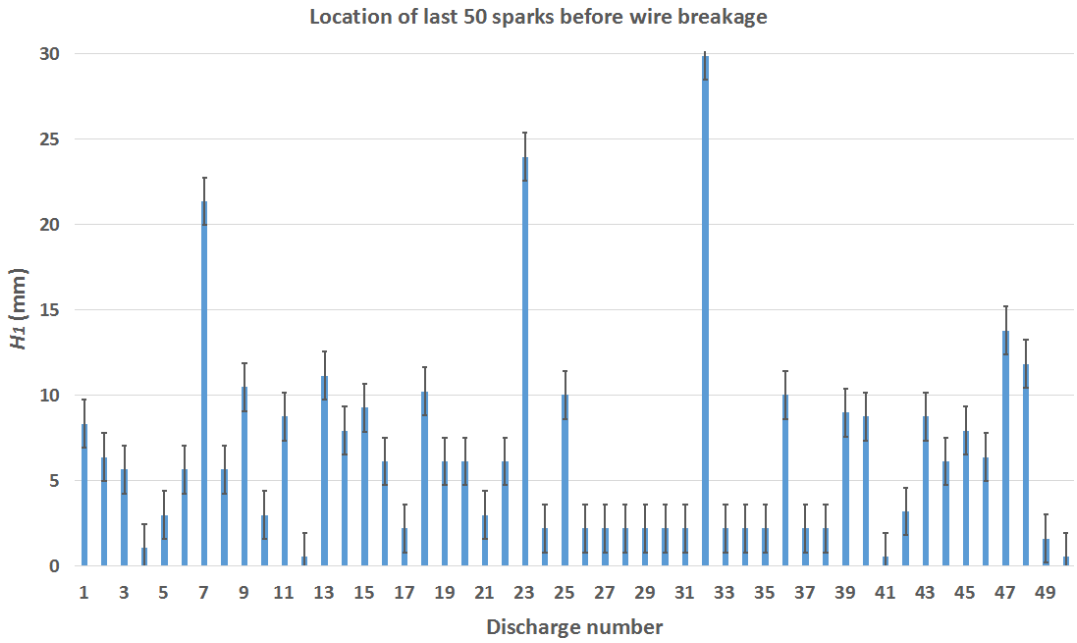

Figure 103. Position of last 50 sparks before wire breakage.

In addition, the broken wire was also observed with Hitachi S-3400N SEM (Figure 104), the result is shown in Figure 105. The failure mode is clearly that of a ductile failure and the cup-and-cone shape which is typical of ductile materials can clearly be observed. The fast fracture region occurs at 45° to the plane of the tensile load, the angle at which the largest shear stress appears. Considering the proposal of Bredgauer et al. [108], this kind of ductile failure is possibly caused by a decrease in the cross-

section area of the wire. For further exploring the reason, finite element simulation was considered to further understand the influence of discharge accumulation on the decrease of wire cross-section area.

Figure 104. Hitachi S-3400N SEM.

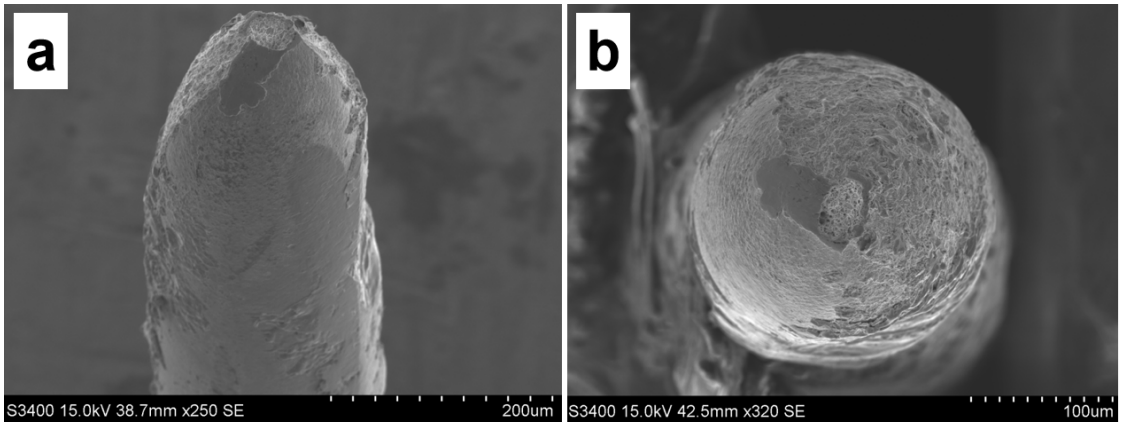

Figure 105. SEM observation on broken wire: (a) Side view; (b) Top view.

V.4.3. Simulation of crater accumulation

Through the experimental result in the previous part, the position with the STD range of the last 50 sparks before wire breakage was obtained. For realizing the simulation of consecutive sparks, COMSOL was selected to do the corresponding work. Firstly, according to the spark position result, the coordinate of the center of each spark was generated by MATLAB randomly in the range of STD. Then, based on the thermal model obtained in the previous section and the setting experimental parameters, the simulation was finished on the wire. As the result shown in Figure 106 (a), after each

spark, the part material whose temperature is higher than the melting point was removed. The craters on the wire are not uniform because of the overlap of craters. For the workpiece, a similar result was gotten by Liu and Guo [87]. It could be determined that concentrated discharges cause a local temperature to increase to make a removal volume increment.

Next, the minimum area of the cross-section of the wire was obtained, as shown in Figure 106 (b). It is observed that after the continuous discharges before wire breakage, the remaining area was measured as 20549μm^2 and it was only 41.88% compared with the original wire cross-section area. The decrease in cross-section area made the stress higher than the UTS of the wire and the ductile failure which is shown in Figure 105 happened. This simulation result matches the experimental result. It further reveals the wire damage from the discharge accumulation and the caused decrease of the area in cross-section is the essential reason for the wire breakage.

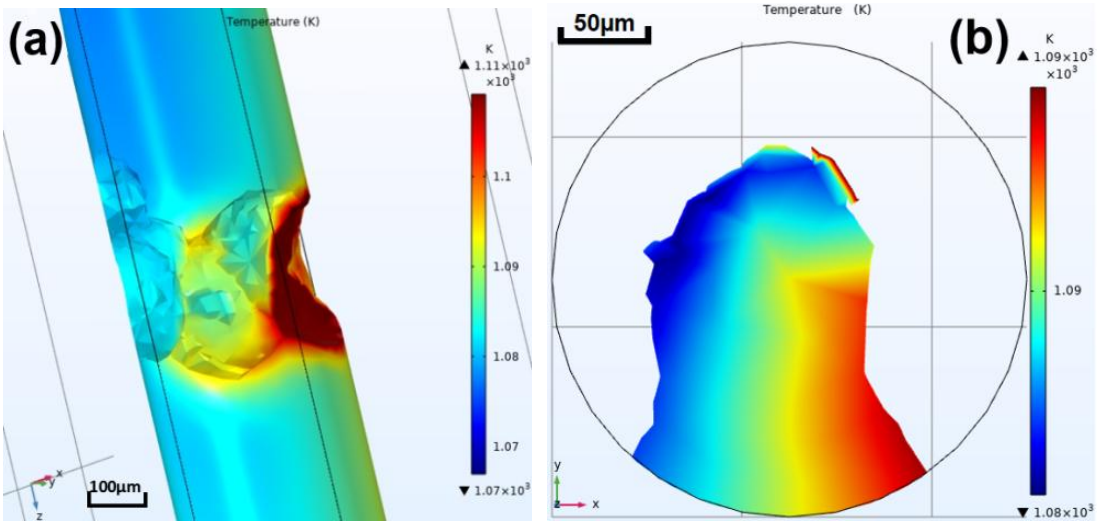

Figure 106. (a) Simulation of consecutive craters on the wire; (b) Minimum cross-section of wire in simulation.

V.5. Conclusions

In this chapter, the principle of thermal transfer to the wire in WEDM was studied and at the same time, a complete thermal model was built. For detecting the effect of accumulative discharges on wire breakage in the WEDM process, several experiments and simulations were conducted in this study. Based on the results obtained, the following conclusions can be drawn:

- Complete observation of the wire after discharges was carried out. The recast layer can be clearly identified, and discharge occurs at 68% of the total wire

circumference. In addition, the flushing efficiency is learned as 44.48%.

- Numerical simulations considering latent heat and flushing efficiency were conducted using the finite element method with different values of f_c. The inverse fitting allows for achieving a precise value for the heat partition ratio to the wire. The value obtained is 46.74%, with a calculated error of 0.53%.

- The damaged area on the cross-section of the wire was simulated for two different values of t_{off} and supposing all continuous discharges are adjacent to each other. From the simulation results used to detect internal thermal changes, it is clear that under t_{off}=4μs, the increase in heat accumulation is faster than that under t_{off}=12μs. Furthermore, with t_{off}=12μs the wire break will occur within 200μs, whereas with t_{off}=4μs, this time will be reduced by more than half.

- Spark locating was carried out based on the current ratio of the upper circuit and lower circuit. The tolerance range of this scheme was verified as 2mm. Based on this, with the workpiece thickness of 50mm, the position of the last 50 discharges before wire breakage was found and as the result, 34% of discharges were located within a range of 2mm.

- A novel 3D finite element model for studying the craters of consecutive discharge on the wire was developed. From simulation results of consecutive discharges before wire breakage, it is found that the minimum area in the wire cross-section only remained at 20549μm^2 and it was only 41.88% compared with the original wire cross-section area. This kind of decrease made the stress higher than the UTS of the wire and ductile failure happened. It further reveals the wire damage from the discharge accumulation and the caused decrease of the area in cross-section is the essential reason for the wire breakage.

Chapter VI: Study on debris particles in WEDM

VI. STUDY ON DEBRIS PARTICLES IN WEDM

It is well known that in WEDM, during the machining process, a huge amount of debris particles are ejected from the gap between the wire and the workpiece. It is an important field that is sometimes ignored. In addition, because of the continuous movement of wire in the machining process, the collection of debris is also a difficult question for resolving. In this chapter, some novel ideas for WEDM debris particle collecting devices were proposed, and the selected design was printed out by a 3D printer. Using the mentioned system, debris particles were collected in various WEDM experiments under different processing parameters. Through analysis and contrast, it was found that in the working gap the material from the wire electrode occupied the dominant part. Moreover, through the observation with SEM and TEM, a complete volume distribution of particles was obtained.

VI.1. Introduction

Debris is an important topic for understanding material removal in WEDM. Whereas, the gap width makes debris collection very difficult. For getting a deeper insight into WEDM debris some works that include debris collection, debris separation, debris observation, and analysis were proposed and carried out in this chapter. In Section VI.2, first, some preliminary designs for debris capitation systems will be shown. Through analysis, the advantages and disadvantages of each plan were detailed. Through comparison, an original debris collection device was designed and manufactured. Also, this device was able to be fixed on the WEDM machine. In addition, a particle collecting system that contains the collecting debris device, conveying debris device, and storage part was also built.

In Section VI.3, first, the method for separating the debris from the collected liquid by rotary vacuum evaporator was introduced. After that, Energy Dispersive X-Ray Fluorescence Spectroscopy and laser diffraction were adopted. As the result, a dominant presence of material from the wire electrode in the working gap was found. The relative percentage of wire material with respect to workpiece material increased when the workpiece thickness increased. Especially noticeable was the increase in the relative amount of Zn. After that, SEM and TEM were used to characterize WEDM debris. Based on that a histogram of size distribution obtained by image processing showed that 98% of the particles were of a diameter smaller than 1µm. A large number of particles showed diameters below 100nm. However, micrometric-size particles occupied most of the volume. In addition, most of the particles corresponded to material from the wire, the relative percentage of wire material with respect to

workpiece material increased when the workpiece thickness increased. Finally, in Section VI.4, some conclusions are presented.

VI.2. Design and manufacture of a device for collecting debris particles

VI.2.1. Preliminary tentative designs

Building an individual filtration system was seen as the first possible plan. This idea was introduced in the work finished by Gatto et al. [109] and M. Tanjilul et al. [110]. In their work, an external circulation system was built and set under the workpiece. For verifying the possibility of building an external circulation system in the ONA AV35 WEDM machine to collect debris particles, a special method was proposed. During the machining process, the water with debris particles flowed through the outfall of the working area which is shown in Figure 107 (a) and Figure 107 (b). Around the outfall, a box with filter paper was placed as shown in Figure 107 (c). To avoid particles settling on the bottom of the machine tank rather than flowing out with water, as shown in Figure 108, two layers of filter paper were laid on the bottom of the tank. And then, the waterproof tape was used to fix the filter paper on the inner wall of the tank. As the debris particles were left on the filter papers with the water flow during the machining process, after the collection of the debris particles from the filter papers, some further analysis and observations of the size and distribution could be carried out.

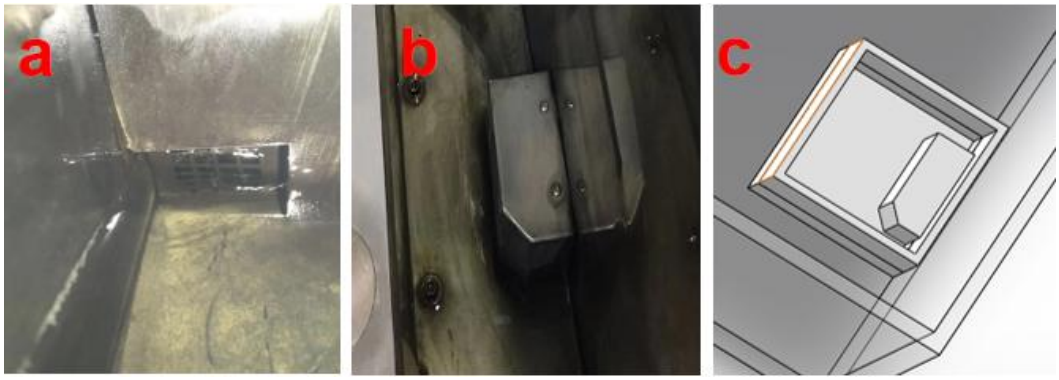

Figure 107. (a) Outfall of WEDM machine; (b) Profile of outfall; (c) Designed part for fitting the outfall.

After several experiments, it was found very difficult to make sure that all the particles were collected from the current experiment because some of the particles in the bottom of the working tank remained from other experiments. Moreover, the flushing flow during the WEDM process sometimes made the filter paper move o even fall from the tank. In addition, it was indispensable to collect the debris particles from the filter

paper, whereas, the concentration of the collected debris particles was very difficult to meet the requirements of the measuring machine. As a result, this design was not adopted.

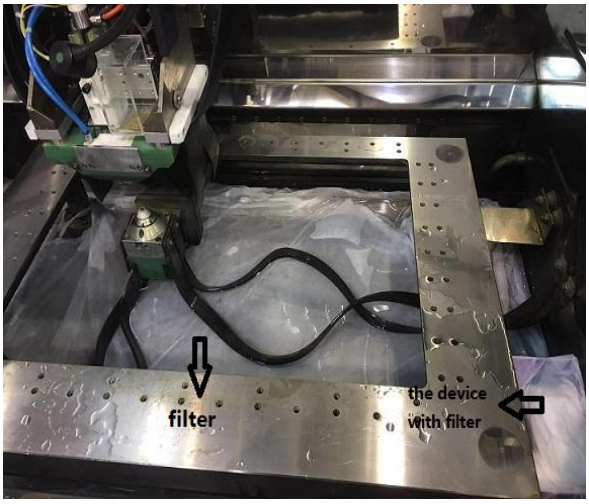

Figure 108. ONA AV35 WEDM machine tank.

Next, another design for a wholly enclosed box around the wire and workpiece area was proposed. The water with debris particles can be pumped out from the bottom part of the box. Considering the wire always moves following the programmed path and the workpiece is fixed on the platform of the machine in the WEDM process, the enclosed box must be fixed on the stationary part of the machine according to the specific situation. After analyzing the WEDM machine construction, the enclosed box can be fixed to the inner wall of the tank. Therefore, removing firstly the platform of the machine becomes necessary to install the enclosed box. This method has the advantage of being able to make sure that most of the debris particles are collected. But at the same time, it is very tough for realizing. As the sample survey method was seen as a more efficient method for the experiment of debris particle analysis, this design was not adopted either.

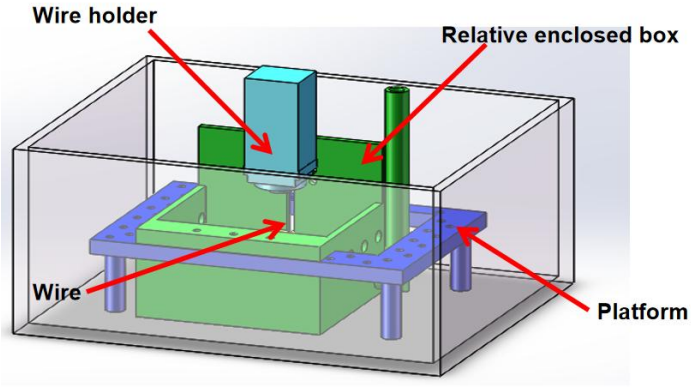

Figure 109. Model of the relatively enclosed box.

Based on the idea of the wholly enclosed box, next, a plan including a relatively enclosed box was proposed. Considering that the wire moves relative to the platform during the general machining process, and there exist many threaded holes on the platform, the relatively closed box can be fixed on the platform as shown in Figure 109. According to the construction of the platform, if the box is made of hard materials, it is indispensable to remove the platform. So the materials such as iron or aluminum were not selected. Then, the relatively enclosed box was considered to be made of soft materials such as rubber and plastic. Furthermore, rubber was seen as a better option than plastic because of its stability. The model was designed using Solidworks which is a 3D modeling software and it is shown in Figure 109. There exist two gaps, one is the gap between the box and the wire holder, and the other one is the gap between the box and the platform. The box can be fixed on the upper half of the wire holder by screws, and the other end can be fixed on the platform. Since the material of this box is rubber and it is fixed by screws, waterproof tape will be used to cover the possible gap.

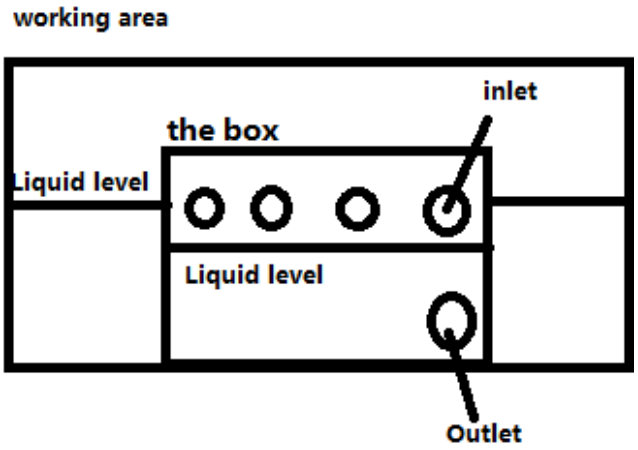

Figure 110. Liquid level diagram.

The principles for collecting debris and the liquid level diagram are shown in Figure 110. When the liquid level around the wire reaches the specified height, the WEDM machine starts to work. The relatively enclosed box height is higher than the specified liquid level, and air intake holes are opened on the sidewall of the box above the specified liquid level. There are a few outlet holes in the lower part of the sidewall of the box. When the machine starts working, the liquid level in the working area outside the box is set higher than the height of the inlet hole, so that the water in the working area outside the box always flows into the box, and the polluted water is under the action of the pump. It is sucked out from the box, which is a dynamic circulation system. This method can not collect all particles in one experiment theoretically, but it can collect most of the particles produced in one experiment and it is enough for the following experiment. This experiment requires the collection of representative

particles for analysis. The manufacturing process of the device is complicated and various special materials are required to be fixed on the machine. Water leakage prevention after connecting various components is not guaranteed and because the box moves with the wire and the table is fixed, the gap between the box and the platform is still not able to be eliminated. This option is only a theoretical model, and there is still a long way to go to realize this type of model.

The next idea for a device for collecting water with debris particles is to design a relatively enclosed box with a smaller size. A model drawn with Solidworks is shown in Figure 111. The device will be fixed on the wire holder. There are two openings in this relatively closed box. One is between the box and the workpiece, because the box is fixed on the wire holder, the box moves with the machining path during the machining process while the workpiece is stationary. So the size of this gap is relatively large. The other one is the opening hole on the top of this box, this hole is used for threading the wire. The size of this hole can be small, but under the condition that the flushing flow can enter the relatively enclosed box in time during the actual machining process, the size of the opening should not be too small. In addition, in the machining process, the debris particles always move in the direction of the flushing flow and accumulate in the lower portion of the tank. Therefore, the outlet was designed at the bottom of the box.

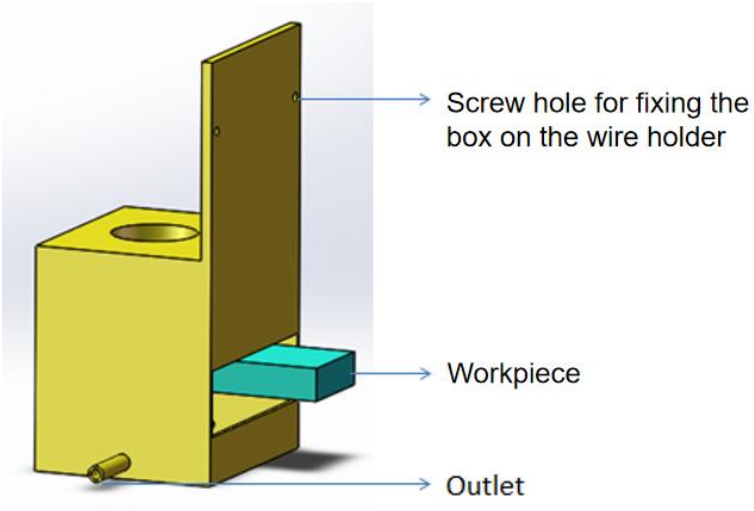

Figure 111. Device model.

Because of the small size of the box, it can be produced by a 3D printer and it is easy to install on the machine before every time experiment. However, disadvantages also exist. For example, in the case of ensuring a small gap between the workpiece and the box, different-sized boxes are required in experiments with different workpiece thicknesses. More importantly, the relatively closed box is placed around the wire. As

the size of the box is very small, it may have a vital effect on reducing the efficiency of the flushing flow in cleaning the debris during the actual machining process, which may result in a reduction in processing efficiency. It may also cause unstable discharge states such as arcing and short-circuit discharge conditions. Therefore, the design still needs to be improved.

Since the purpose of this experiment is to collect some debris as the sample in the WEDM process for analysis, rather than collecting all the water with debris particles, collecting debris only around the wire during the machining was next considered a better method. In the process of machining, the wire always moves according to a predetermined trajectory. So if design a device that can be fixed on the wire holder, the device also can move as the wire moves. Then a pump can be used to pump water out from the working area. To collect debris particles in all directions around the wire, the area where the device is in contact with water should be increased. Therefore, considering the convenience of device manufacturing, 3D printing technology is applied to new device manufacturing processes. Taking into account all of the above factors, the device schematic is shown in Figure 112.

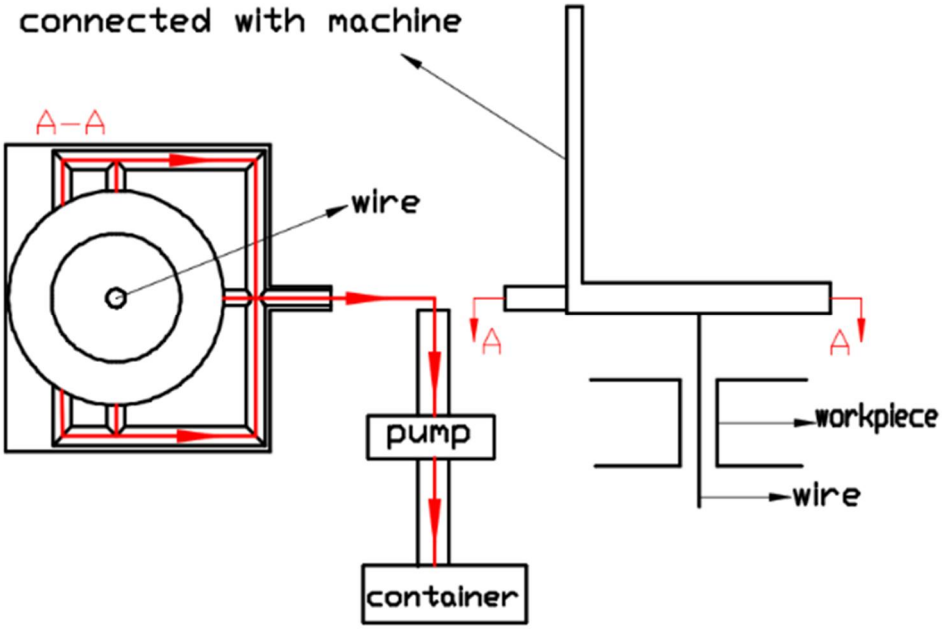

Figure 112. Device schematic.

Then, the device as shown in Figure 113 was printed by a 3D printer and it was connected to the WEDM machine. In the actual process, under the action of the pump, the water containing debris was pumped out of the work area according to the red trajectory shown in Figure 112. To collect the water with debris in all directions around the wire, five inlets were placed around the wire and the water was collected into one outlet. In addition, as this device just needs to be fixed on the wire holder, it is easy to

install and it makes the experiment easy to implement. However, the principle of collecting water with debris was full of contingency, and it can not be guaranteed that debris particles have been collected in each discharge state. Therefore, in the actual experiment, water was collected multiple times using this device in order to improve the accuracy of the obtained sample.

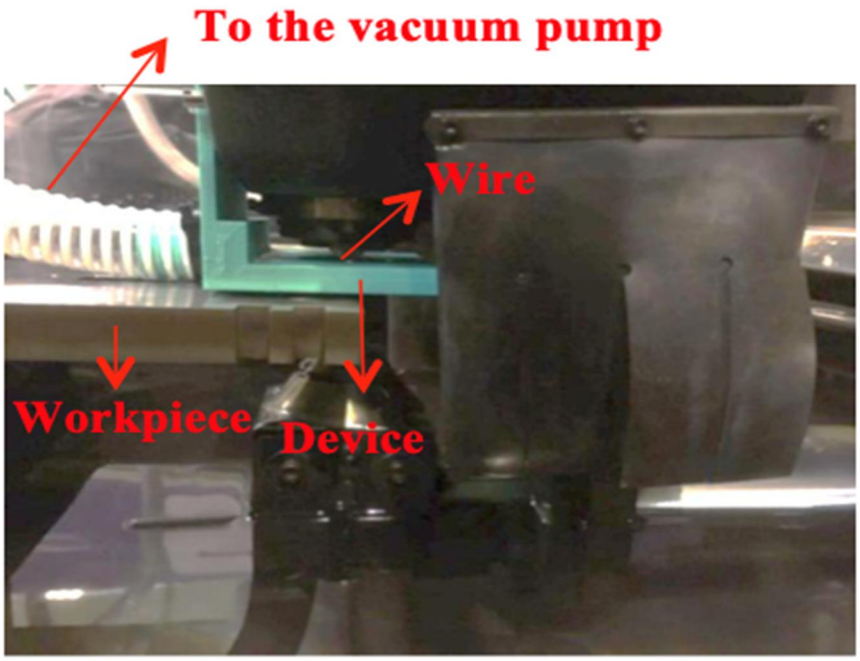

Figure 113. Device and installation diagram.

VI.2.2. Adopted solution

As the method used to collect the particles in this experiment is a sample survey, some of the debris produced in the actual treatment is sufficient for the preliminary analysis of the fragments. In the experiment, the device should be as close as possible to the wire. If a relatively enclosed box or a completed enclosed box is selected, an external circulation system must be established that includes extracting water with debris particles and simultaneously inputting the clean water during the whole machining process. However, it is very difficult to realize the external recycling system without affecting the processing. Hence, the last plan referred to in the previous section is the best choice for preliminary experiments. As the vacuum pump can not be used to pump water out directly, a novel debris particle collecting system is presented. The schematic of this system is shown in Figure 114. In that, the water around the wire is sucked into the container under the pressure differential caused by the vacuum pump. And then, it enters the enclosed container along the red line in Figure 114. The collected liquid contains a large amount of water and a small number of particles.

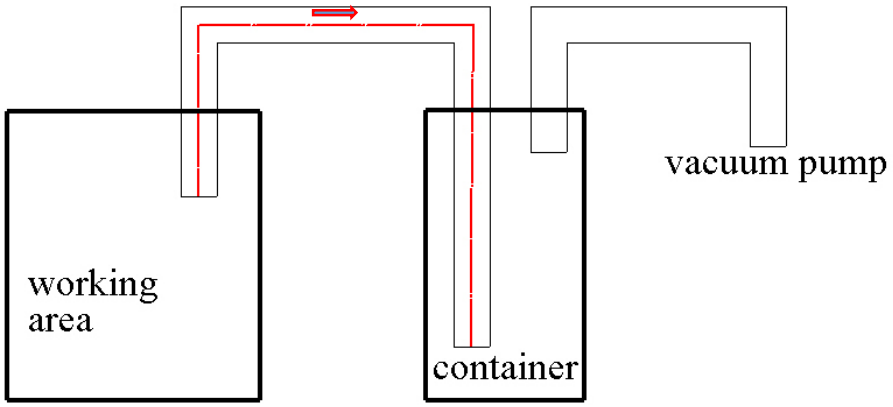

Figure 114. Debris particles collecting system.

In detail, the selected debris particles collecting system consists of the following three parts: the collecting debris device, conveying debris device and the storage debris device. The collecting debris device which is shown in Figure 115(a) was printed by the Leon-3D printer and it was made of PLA Ingeo 850 which is an environmentally friendly material. PLA has a melting point of 155-185^{o}C and it is suitable for practical machining conditions. The conveying debris device was made up of a vacuum pump with a hose. As shown in Figure 115(b), the Bosch sphere 27 vacuum cleaner was used as the vacuum pump because it is convenient to control the start and end timing. The enclosed container consisted of a water bottle and a special bottle mouth for the connection. The special bottle mouth was also printed by the Leon-3D printer to connect. The storage device of water with debris particles was a 500ml plastic bottle. In addition, the engineering drawing of the collection debris device is shown in Figure 116.

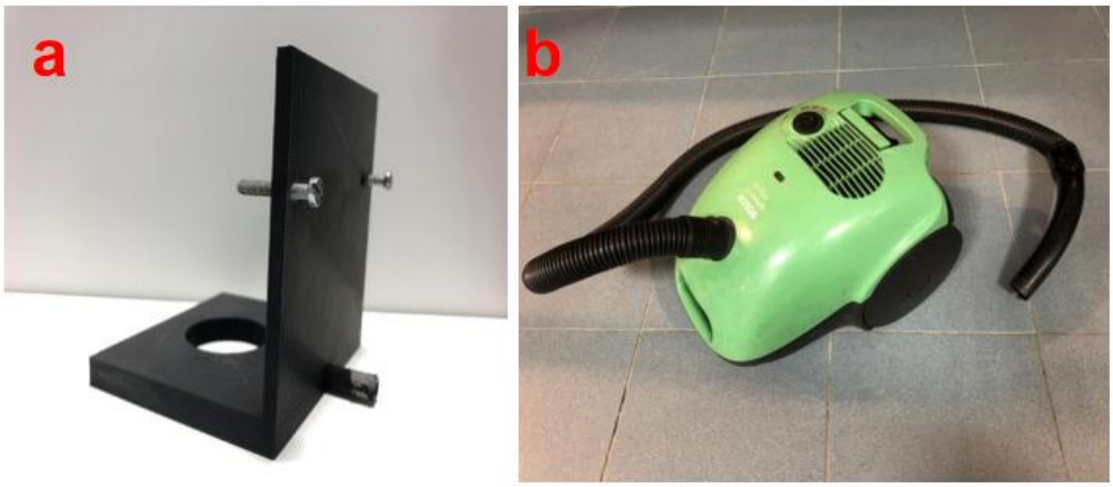

Figure 115. (a) Collecting debris device; (b) Vacuum Pump.

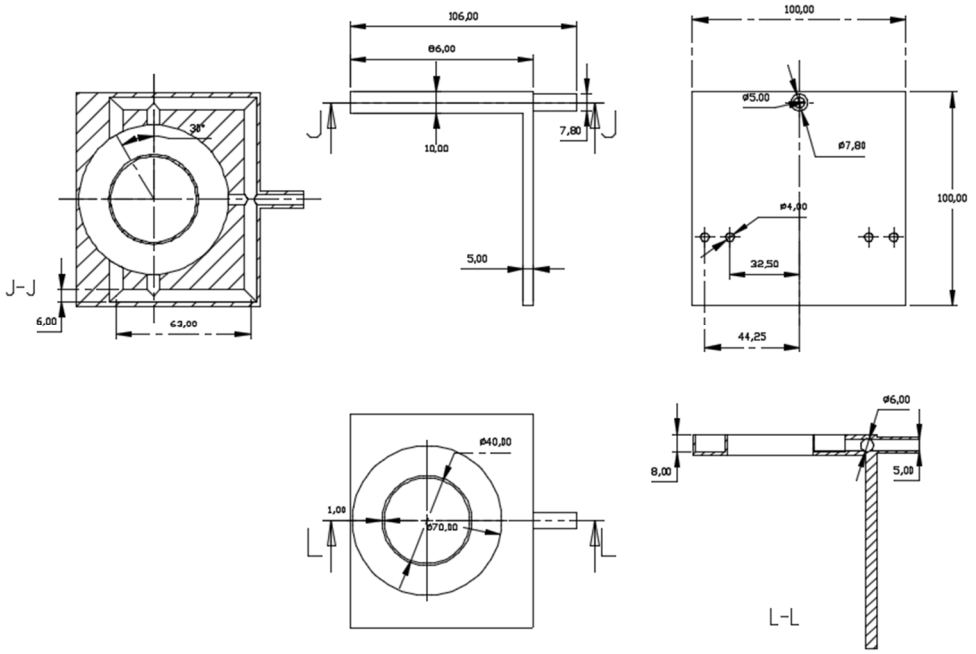

Figure 116. Engineering drawing of collecting debris device.

VI.3. Observations on debris composition and size distribution

VI.3.1. Experimental set-up

WEDM experiments were carried out on ONA AV35 WEDM machine. The workpiece material was AISI D2 tool steel, and 0.25mm diameter CuZn37 wire was used. Experiments involving different part thicknesses, gap widths, and discharge currents were performed as presented in Table 32.

Experiment number	h (mm)	I (A)	t_{on} (µs)	t_{off} (µs)	U_o (V)	g (µm)
1	20	5	2	7	80	51
2	50	5	2	12	80	62
3	50	15	2	12	80	62
4	150	5	2	21	80	69
5	250	5	2	30	80	78
6	250	15	2	30	80	78

Table 32. WEDM parameters for the experiments.

In the experiments, a large volume of water with debris particles was collected by the collecting system which was introduced in the previous section. The debris particles need to be separated from the collected liquid for increasing the concentration of debris particles. Usually, the membrane is used to do the filtering. But considering the high cost and difficulty of operation, other alternative methods were proposed. The

first one was to add desiccant. Whereas, this kind of method may affect particle size results. Another proposed method was evaporating the collected liquid for obtaining the debris particles. An objective condition was that a too-high temperature could cause debris adhesion and then affect the final results. Therefore, evaporating excess water at not too-high temperatures was an insurance method and it was finally adopted, even at a high time cost.

Preliminary experiments were carried out on a constant temperature furnace, and the temperature is set to 80 degrees. It cost 24 hours to evaporate 1.5L water because the concentration of the original solution was extremely low, it took about 48 hours to get the ideal solution for each experiment. Two factors determine the amount of water evaporated, one was temperature and the other was the evaporation area. The maximum temperature was limited, so increasing the evaporation area was the only way to improve efficiency. The rotary vacuum evaporator was used in this stage. Finally, the Heidolph Laborota 4000 rotary vacuum evaporator (Figure 117) was used to do the evaporation and a 500ml plastic bottle was used to store the solution to be tested.

Figure 117. Overview of rotary vacuum evaporator.

VI.3.2. Analysis of debris particles

As demonstrated by J. W. Murray [62], through experimentation, the morphology of the fragments produced in the actual EDM process was mostly spherical. In addition, spherical particles can be described using a discrete number of diameters. A variety of length and width measurements (horizontal and vertical projections) can be used to describe non-spherical particles. These descriptions provide greater accuracy but are

also more complex. Therefore, many techniques make each particle a useful and convenient assumption for a sphere, and also the recorded value is usually the equivalent spherical diameter. The shape of the particles produced by most industrial processes made spherical assumptions [111]. Therefore, in this study, the profile of the particle was also seen as a sphere.

VI.3.2.1. Size and distribution of debris

Firstly, the Master size 2000 laser diffraction particle analyzer shown in Figure 118 was adopted. Its measurement range was from 0.02μm to 2000μm. Therefore, debris less than 0.02μm was ignored because of the limitations of the employed equipment. The result of debris of experiment 1 (Table 32) size distribution from Master size 2000 is shown in Figure 119. Several conclusions can be obtained. The diameter of 10% of the debris in volume is no more than 8.047μm, 50% is no more than 16.012μm and 90% is no more than 31.314μm. Most particles have a diameter in the range of 5μm to 50μm.

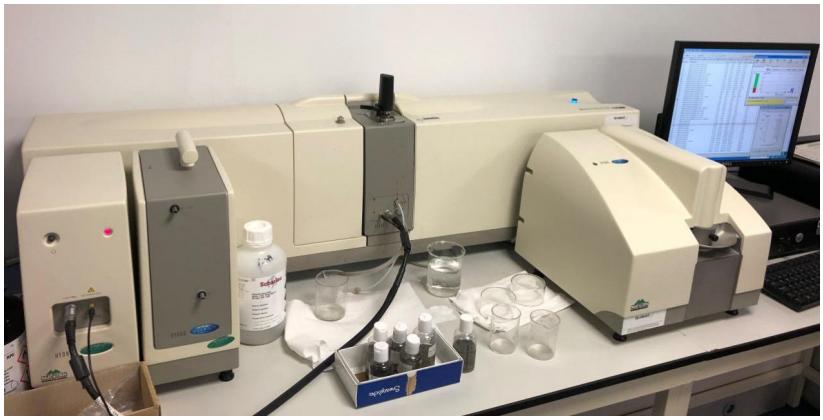

Figure 118. Overview of Master Size 2000.

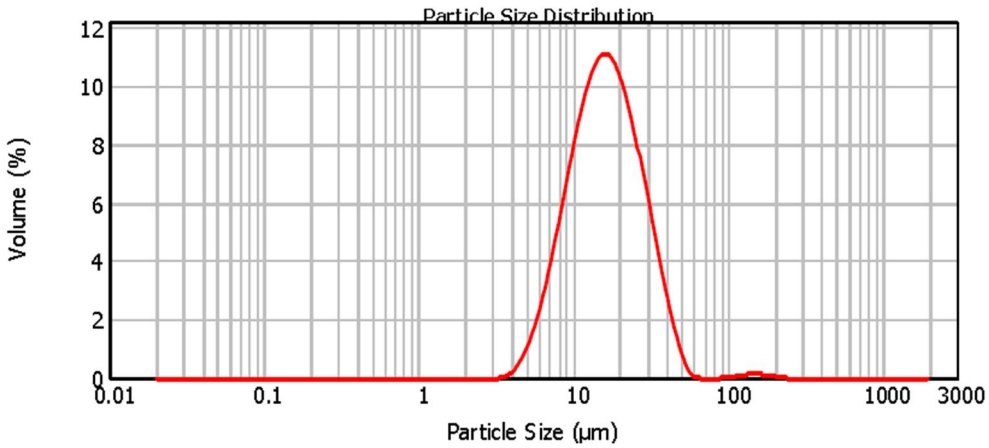

Figure 119. Debris size distribution.

After that, SEM was used to measure micron fragments and observe the surface topography of the sample by imaging, magnifying and displaying the information [112]. When an image was obtained, image analysis software (ImageJ) was used to obtain the granularity information. The size, composition and morphology of debris particles from experiment 1 (Table 32) were carried out using JSM-6400 equipment for SEM-EDX analysis. First, a general view of the sample was taken (see Figure 120(a)), in a region of about 1mm^2 area. This was labeled as region A. In this region, 13 local analyses were performed including composition and morphology. These were labeled from A1 to A13. Local analyses were performed including composition and morphology. The general view shows white particles that correspond to metals. Some large regions do not look spherical. Going forward in magnification (for instance, around region A13, see Figure 120(b)), large depositions of what are probably nanometric-size metal oxides are observed. Because of the drying method used, nanoparticles tend to agglomerate like dust.

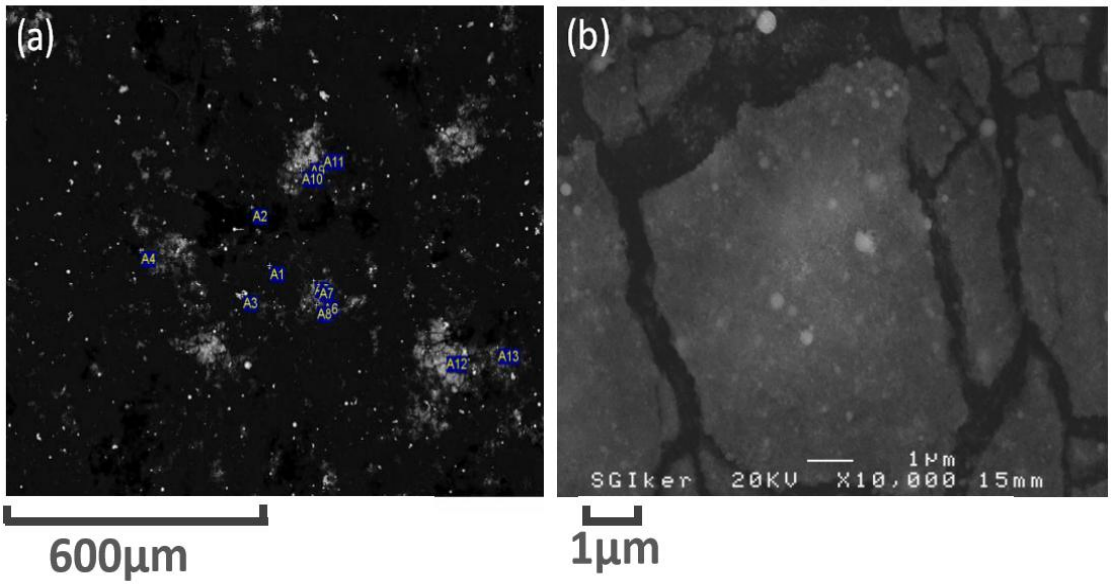

Figure 120. (a) General view of the sample and location of local analyses; (b) Detail of Region A13, where agglomeration of nanometric-size particles can be observed.

A few typical cases are shown in Figure 121. Figure 121 (a) and Figure 121 (b) are the samples A1 and A2, their size is about 8µm and 9µm, the particle in Figure 121 (a) is slightly non-spherical and in Figure 121 (b) is spherical, they are composed of Cu and Zn elements and from the wire. Figure 121 (c) is sample A5, its shape is close to a sphere, its size is 9µm, it is composed of Fe, V, Cr elements, and it is from steel. Figure 121 (d) is sample A13, some metallic sub-micron particles (white spots) are present, but a clear agglomeration of very small darker particles is also evident.

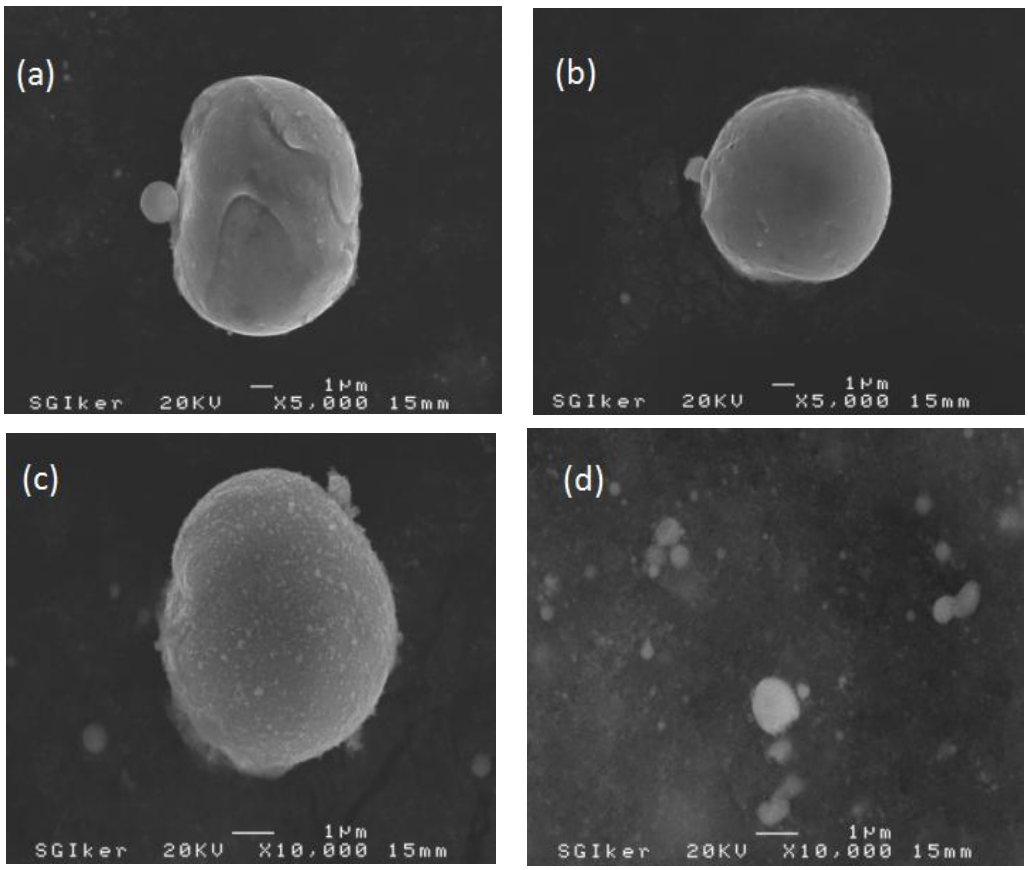

Figure 121. Typical cases of sample.

The image processing software ImageJ then was used to measure the size distribution of the sample fragments. From Figure 120 (a) it was found that the individual particles were significantly brighter than the accumulated ones. Individual particles can be filtered using appropriate thresholds. The software then converted the original image to a binary image. After processing the software ImageJ, the detected particles were marked with a red circle. Finally, the software automatically calculates the particle size detected in the image and generates a data file. In this experiment, to display the size information of the fragments, the fragment size was divided into two levels, the micro-level and intermediate level between the micro and nano levels. In microscopic-level statistics, particles smaller than 1 micron and larger than 22 microns were ignored, and the results are shown in Figure 122. At intermediate levels between microscopic and nanoscale statistics, only particles of 0.46 to 15 microns were considered, and the results are shown in Figure 123.

From the results of SEM, particle aggregation was very serious, which had a great impact on the measurement results. To alleviate the phenomenon of particle aggregation, the sample preparation stage was omitted, and the liquid during the processing was directly taken for measurement, and the degree of particle

aggregation was significantly reduced.

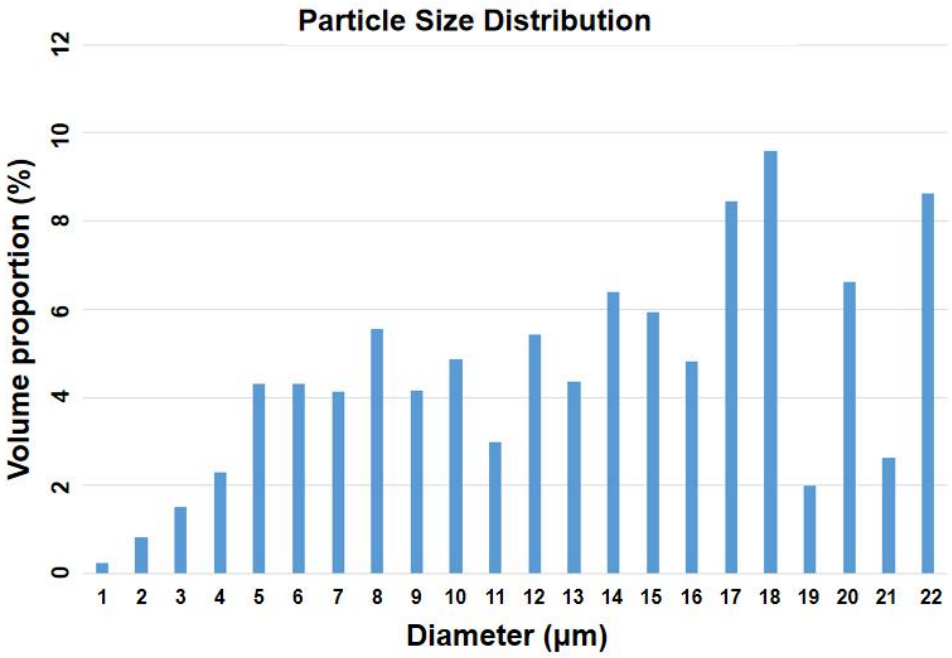

Figure 122. Size distribution of micro-level debris.

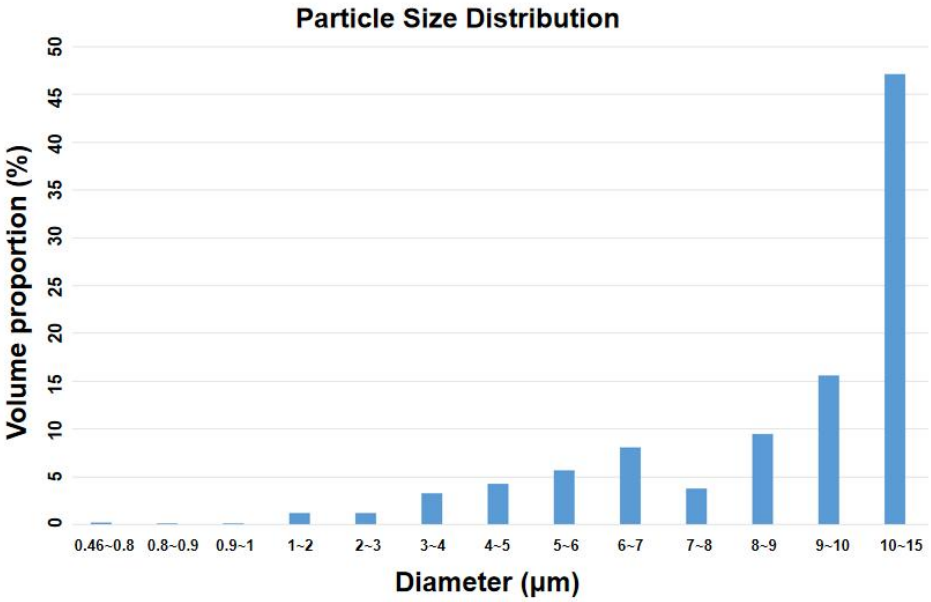

Figure 123. Size distribution of intermediate level between micro and nano-level debris.

Finally, for resolving the nature of sub-micrometric particles, JEOL JEM 1400plus transmission electron microscope (TEM) which is shown in Figure 124 was used to do further observation. The image obtained by TEM was also processed in ImageJ software. To avoid particle aggregation, the sample was measured by TEM without

sample preparation. Results are shown in Figure 125. Among all the observed particles, the largest diameter was 25μm, and the smallest diameter was lower than 100nm.

Figure 124. Overview of TEM-1400 Plus.

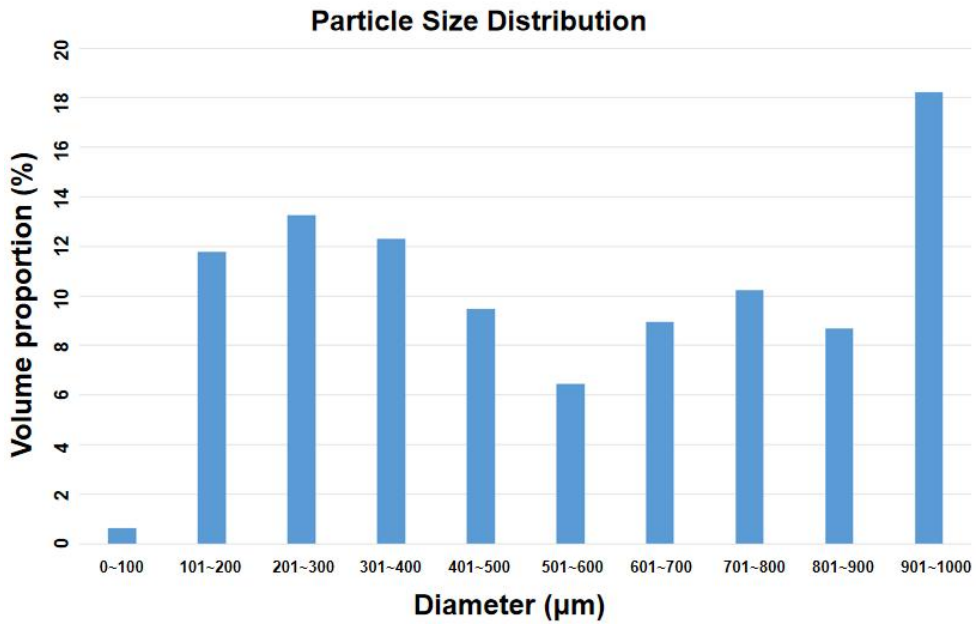

Figure 125. Size distribution of nano-level debris.

The first aspect to be noticed is the good agreement between the volume distributions obtained through using two very different techniques, namely laser diffraction and image processing. Probably the results from laser diffraction may exhibit some uncertainty in the region of the largest particles, because some agglomeration may occur. In any case, it can be seen that the volume is mostly dominated by particles of

diameter within the range between 5 and 25µm. However, as said before, volume distribution hides the existence of very small particles. Amount distribution (Figure 126) shows that 98% of the particles correspond to diameters below 1µm.

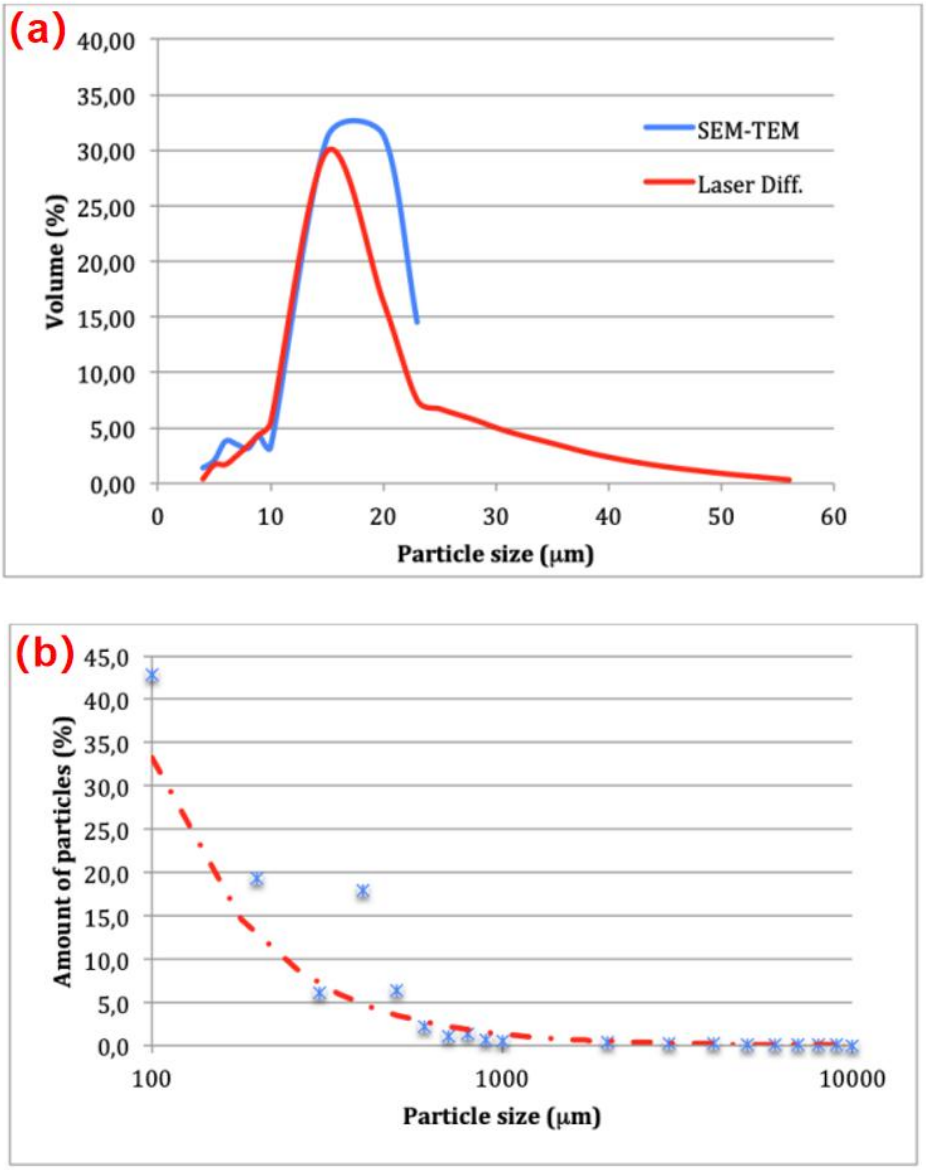

Figure 126. Histograms of particle size distribution: (a) Volume distribution (from image processing) and comparison with results from laser diffraction; (b) Amount distribution.

The presence of the smallest particles might also support the hypothesis placed first by Yang [113], after which vaporization might remove part material as clusters of atoms, or even single atoms during discharge on time. This was also described by Murray in SEDM experiments. Guo [114] and Murray [62] suggest that larger particles could be produced by either thermal shock during the first picoseconds of the discharge, or by pressure drop on molten metal at the end of the discharge.

VI.3.2.2. Composition of debris

To get more detailed information about the debris, the composition of the debris must be analyzed. From the SEM-EDX that is referred to in the previous section, some observations were done while measuring the size of the debris. A closer look at the largest particles reveals the morphology of debris. The largest particles are spherical, or very close to this shape. Figures 127 and Figure 128 show spherical particles and the EDX analysis, showing the presence of Cu-Zn from the wire electrode (Figure 127) and components from steel (Fe, Cr, V, Mo) from the workpiece (Figure 128).

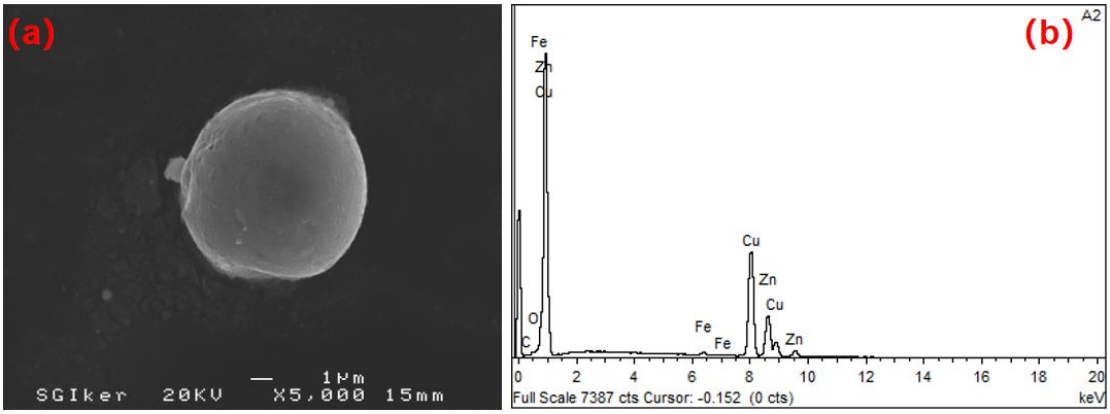

Figure 127. (a) Spherical particle of diameter 7.8µm; (b) EDX analysis of the particle, revealing the dominant presence of Cu and Zn from the wire electrode.

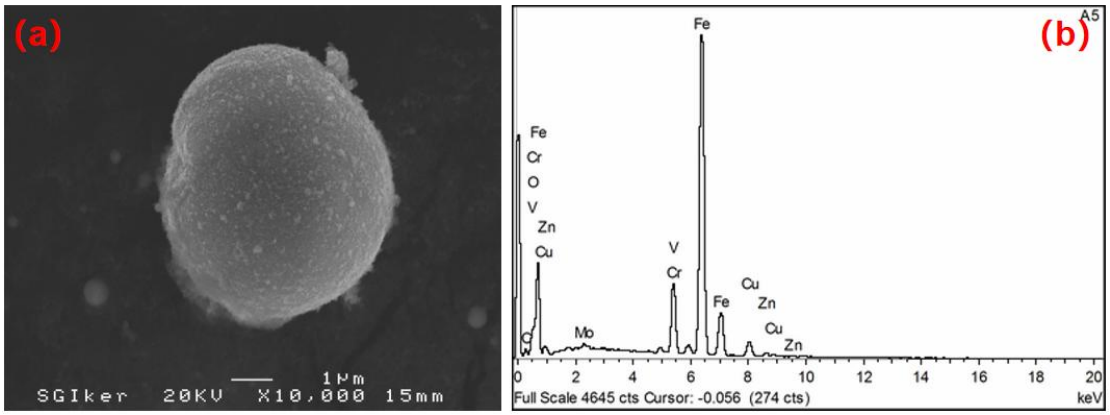

Figure 128. (a) Nearly spherical particle of diameter 9µm; (b) EDX analysis of the particle, revealing the dominant presence of Fe, Cr, V and Mo from the workpiece.

The observed particle sizes are sound with the previous findings from laser diffraction. The largest observed particles are about 20µm in diameter, but most of the samples are within 5-10µm. Large metallic particles look brilliant in SEM images. Particles of Fe and other elements (original components from AISI D2 tool steel) and Cu-Zn are observed in diameters between 1 and 20µm. These particles are mainly spherical, although some of them are slightly deformed. Non-spherical shapes, normally larger

than 20µm correspond to agglomerations due to the drying process and they can be clearly identified. Fe-based particles are present, but to a lesser extent, probably because Fe oxidizes more easily than Cu-Zn.

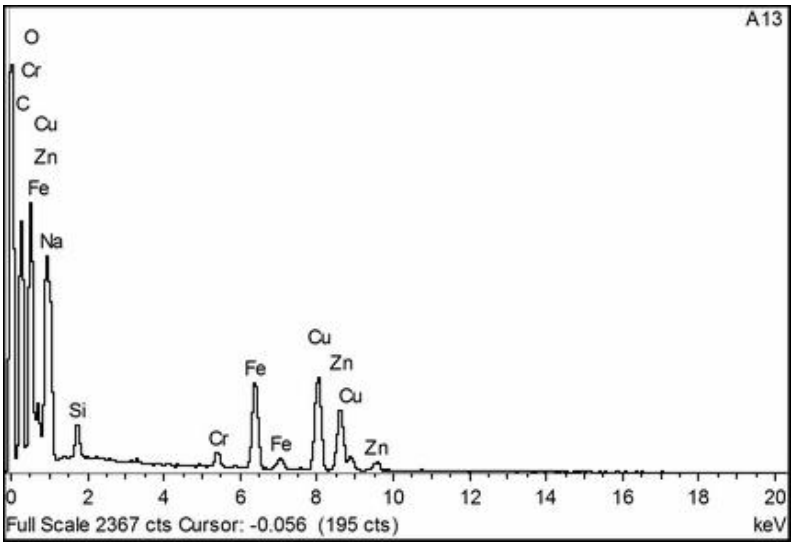

Figure 129. EDX analysis of the sample.

Because the spot of the EDX probe is 1µm^3, composition analysis of sub-micron particles cannot accurately be carried out (several different particles will lie inside the EDX spot). Even though, observation of those sub-micron particles was carried out. Figure 129 shows the EDX analysis of the sample shown in Figure 120 (b). The analysis reveals the presence of metals (Fe, C, Zn), but also probably Fe oxides. This is known because, due to the low atomic number, oxides look darker in the SEM image. The results are in accordance with the already mentioned SEDM experiments by Murray [62], who found many spherical particles of a diameter smaller than 2µm and even suggested the possible presence of sub-nanometer particles that could not be detected.

In addition, another X-ray system (Figure 130) was used for detecting the composition of debris. This machine is from the company of Fischer, the type is Fischer scope X-ray system XDAL. X-ray measuring instruments generally use an instrument that excites a target element in a sample to generate characteristic X-rays and determines the target element and its content by measuring the exposure rate of the characteristic X-ray. Taking into account the content of elements in the sample, only three elements were considered, Fe, Zn, and Cu respectively. Fe comes from the workpiece. Cu and Zn come from the wire. Analysis of these three elements can estimate the percentage of particles from the workpiece and the wire. For each sample, 5 measurements were obtained. The summary of results is gathered in Table 33 (mean values). Only the most important elements from the workpiece and wire are presented in Table 33.

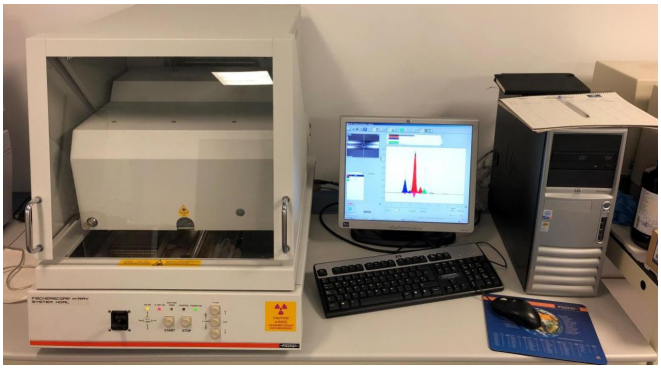

Figure 130. Overview of X-ray system.

h (mm)	*I* (A)	*g* (µm)	Fe (%)	Cu (%)	Zn (%)
20	5	51	19.43	44.756	35.91
50	5	62	10.34	44.538	45.11
50	15	62	9.10	43.798	47.09
150	5	69	9.42	37.39	53.18
250	5	78	4.39	26.85	68.75
250	15	78	3.13	34.53	62.33

Table 33. Results of X-ray system analysis of debris samples.

Results show the dominant presence of material from the wire in the debris. As explained in the previous section, some large (1-20µm diameter) Fe particles can be found in SEM analysis, but much less in number than Cu-Zn particles. Although further research is required on this point, it must be considered that Fe tends to oxidize more easily than Cu and Zn.

When increasing part thickness, gap width also increases, and under these conditions, the percentage of material from the wire increases as well. It must be mentioned the important increase in the presence of Zn. Larger gap width results in decreased heat flux density under the same current, as observed by Kojima [25] using optical emission spectroscopy. Also, a larger gap involves more heat loss toward the dielectric fluid. Probably because of a reduced heat flux density, the removal of low melting point metals such as Zn becomes more important when compared to that of Fe and/or Cu. The increase in discharge current does not introduce significant differences in the composition of debris.

VI.4. Conclusions

In this chapter, a study of the composition and size distribution of debris particles in the working gap in WEDM was presented. The objective is to get a deeper insight

because little information about WEDM debris can be found in the literature. Existing numerical models for WEDM apply data obtained from SEDM experiments. From the work carried out the following conclusions can be drawn:

- Obtaining debris in the WEDM process is difficult because of the small machining gap width and the debris separation from the collected liquid. Some possible methods for collecting debris were discussed and contrasted. Finally, a novel debris particle collecting system that contains the collecting debris device, conveying debris device, and storage debris device was designed and manufactured. In addition, the procedure for separating the debris from the collected liquid was also introduced.

- Results of the composition of collected debris using EDXRF show a dominant presence of material from the wire electrode (Cu+Zn) in the working gap. The relative percentage of wire material with respect to workpiece material increases when part thickness increases. Especially noticeable is the increase in the relative amount of Zn. Although further research is required at this point, this could be related to the lower melting point of Zn and to the reduced heat flux density when increasing the working gap width.

- Spherical particles in the range of diameters between 1 and 20µm were found by SEM analysis. Most of the particles observed correspond to material from the wire (Cu-Zn), but some Fe spherical particles have also been found. Agglomerations of sub-micrometric particles due to the drying method were found as well.

- TEM analysis allows for resolving lower-scale particles. Histograms of size distribution obtained by image processing show that 98% of the particles are of a diameter smaller than 1µm. A large number of particles show diameters below 100nm. However, micrometric-size particles occupy most of the volume. Results of volume distribution from laser diffraction are in good agreement with those obtained using image processing.

Chapter VII: Conclusions and future works

VII. CONCLUSIONS AND FUTURE WORKS

In this chapter, the main conclusions of this thesis will be listed, and the future research interest that has been found in the research and learning will also be proposed.

VII.1. Conclusions

Improving machining quality and efficiency has always been the top priority in the field of precision machining. To achieve this, an in-depth understanding of the machining process and machining principles become essential and indispensable. This thesis is dedicated to further analyzing some fundamental aspects of the WEDM process through experiments and relevant discussion.

In Chapter I, the existing scientific research work in the field of WEDM was reviewed and summarized. Based on this, the research directions that should be further explored were defined. As it is known that the quality of WEDM depends to a large extent on the quality of discharge, it is necessary to achieve a better understanding of discharge occurrence. Therefore, the discharge delay time which is used to distinguish the type of discharge or to judge the discharge situation was investigated in Chapter II. In the experiment of single discharge, 3 kinds of machining parameters, which were gap width, surface roughness and volume flushing flow rate respectively, were selected to study their influence on the discharge delay time. Based on the experimental result, it was observed that an increase in gap width or a smoother workpiece surface made the discharge delay time larger. Then for the flushing condition, it was found that, with a higher volume flushing flow rate, the discharge delay time increased. Using an apparatus that included plastic optical fiber and He-Ne laser, the wire movement under different volume flushing flow rates was studied. With a higher volume flushing flow rate, the average position of the wire is farther from the initial position and it made the gap width larger. This was determined as the main reason why the higher volume flushing flow rate made discharge delay time longer.

Then, continuous discharging conditions were investigated. The observation using a high-speed video camera was also finished during discharging. Through observation, the discharge location was successfully detected through grayscale analysis of photos, and the corresponding discharge delay time of each discharge was measured using an oscilloscope. Results show that the probability that the discharge occurs within 0.5mm from the location of the previous discharge is the highest, and if there are a sufficiently large number of discharges between two discharges, the distribution tends to be

random. In addition, when discharges occurred around the previous discharge, most discharges occurred near the boundary of the bubble, and few discharges occurred inside the bubble. It verifies the influence of the debris particles concentrated at the bubble boundary on the discharge occurrence in WEDM. For exploring the influence of the previous discharge on the occurrence of the following discharge, the bubble generated by the discharge was measured. As the result, the size of the bubble and the first cycle of bubble oscillation is almost uniform under the same machining condition. If the discharges generate under different peak discharge currents, the oscillation cycle and the size of the generated bubble are different. With a lower peak discharge current, the first oscillation cycle is shorter, and the bubble size is smaller. Then, by comparing the bubble oscillation cycle and the relationship between the discharge delay time and the undischarged rate, it was observed that more discharges occurred in the process of bubble expansion. It verifies the influence of the bubble expansion on the discharge occurrence, and it can be explained by the effect of the debris particles concentrated at the bubble boundary.

Next, the workpiece material removal in WEDM was studied in Chapter III. The plasma channel between the wire and the workpiece is generated after reaching the breakdown point in the process of machining. After that the produced heat transfers into the workpiece and this causes the crater on the surface. Material removal is due to the superposition of the huge number of craters forming on the workpiece. Hence, it is very important to understand the process of crater forming and the influence of parameters on this process.

From the experiments using workpieces with different surface roughness values, it was determined that the diameter of the crater on the rough surface was typically smaller than that on the flat surface. Moreover, on a flat surface, the situation of three consecutive and four consecutive or even more than four consecutive craters was observed. Whereas, in terms of rough surface, there were few consecutive craters. Simultaneously, the percentage of continuous craters on a rough surface was lower than on a flat surface. In addition, on a flat surface, the center of consecutive craters always appeared on the rim of the previous crater. Because the reason for this is that around the first crater, there were some roughness peaks. These peaks made the consecutive crater easier to take place on the rim of the first crater. Whereas, as the roughness of the rough surface, it made not evident those roughness peaks around the first crater. Therefore, the consecutive craters did not often appear on the rough surface. In addition, on a rougher surface, the crater depth is smaller but the crater diameter kept similar. This means that the crater volume on the smoother surface is larger. Next, the influence of gap width on crater forming was also investigated. Through corresponding experiments, it is found that the larger gap width made the

crater volume smaller.

Furthermore, the plasma channel radius and the heat partition of the heat source to the workpiece were studied by combining experiments and numerical simulation. Through building a thermal model and comparing the numerical values of the boundary conditions between the flat surface and rough surface, it is found that the plasma channel radius was not affected a lot by the surface roughness. Whereas, the heat partition to the workpiece on the flat surface was 29.6% higher than that on the rough surface. The result of this part is useful for further understanding the principle of materials removal in WEDM and the relative influence of different machining conditions.

Although it is known that the heat transferred to the workpiece realizes the material removal, another part of the heat source was also transferred to the wire. It makes the wire wear and even wire breakage. Wire breakage will reduce processing efficiency and affect the quality of processing. Therefore, the study of wire breakage in WEDM processing was investigated in-depth. From the work describe in Chapter IV, it can be concluded that the heat accumulation and the damage caused by the craters caused by continuous discharge on the wire is the reason that causes the breakage. For detecting the effect of discharge accumulation on wire breakage in the WEDM process, the experiment of continuous discharge was performed and after that, the wire after discharges was collected. Next, the wire with craters was observed, and it is found that discharges occurred at 68% of the total wire circumference. In addition, through the measuring of the recast layer, the flushing efficiency was determined to be 44.48%. Based on this, a more comprehensive and complete model was established. By comparing the simulation result and experimental result, the heat partition to the wire was also obtained and the value was 46.74%.

Furthermore, the reason for the wire breakage was discussed from two aspects. Firstly, heat accumulation in the wire was studied. Through comparing two kinds of pulse intervals, it was determined that, if all continuous discharges are adjacent, with a shorter pulse interval the heat accumulation in the wire is faster and the wire breakage occurs earlier. Then, a spark location method for locating the position of several discharges just before wire breakage was presented and verified. Using this method, a wire breakage experiment was finished and the position of 50 sparks just before wire breakage was obtained. Based on the numerical model that was mentioned before, a simulation that can simulate the removal crater on the wire was developed in order to analyze the process of wire breakage. From the simulation result, the wire cross-section area reduced caused of the continuous adjacent craters. This kind of reduction makes the stress higher than the UTS of the wire and causes the wire breakage. This

result reveals the wire damage from the discharge accumulation and the caused decrease of the area in cross-section is the essential reason for the wire breakage.

As it is known that in the WEDM process, the material of both the workpiece and the wire is removed and it is emitted as debris from the working gap. In Chapter II the fact that debris can affect the discharge occurrence is discussed. Therefore, the debris formed in the WEDM process was gotten a deeper insight in Chapter V. Because of the continuous movement of wire in the machining process, the collection of debris becomes very difficult. For resolving this problem, some possible methods for collecting debris were discussed and contrasted. Finally, a novel and efficient debris particle collecting system that contains the collecting debris device, conveying debris device, and storage debris device was designed and manufactured. After the collection procedure, the rotary vacuum evaporator was used to separate the debris from the collected liquid. With the gathered debris, energy dispersive X-Ray and laser diffraction were adopted were used to analyze the composition. As the result, a dominant presence of material from the wire electrode was found in the working gap. The relative percentage of wire material with respect to workpiece material increased when the workpiece thickness increased. The increase in the relative amount of Zn was especially noticeable. After that, SEM and TEM were used to characterize WEDM debris. Based on that, a histogram of size distribution obtained by image processing showed that 98% of the particles were of a diameter smaller than 1µm. A large number of particles showed diameters below 100nm. However, micrometric-size particles occupied most of the volume. This result can help in the understanding of the debris particles since the complete volume distribution of debris particles has been clarified.

VII.2. Future works

Because of the complexity of the WEDM process, there are still many aspects that are worth studying in depth. Several future research focuses are proposed:

To develop a system to monitor and predict the machining quality and result

As the discharge location system and thermal model have been obtained, the material removal process of continuous discharge can be simulated in real time. This can be used for monitoring and predicting the machining result and it can be useful to enhance the machining quality.

To study the influence of turbulence on the wire vibration

Flushing flow always exists in the WEDM process for helping the debris emission from

the working gap to improve the machining quality. However, through the calculation of the Reynolds number, it can be observed that the flushing flow may form turbulence during the machining process. This can be a reason for the wire vibration and it may affect the machining quality to a certain extent. Therefore, it is worth doing a further study about this aspect of the process in the future.

To further observe the WEDM discharging process using a transparent electrode

It has been proved that the bubbles generated by discharges can influence the discharge occurrence and it is assumed that this happens because of the debris concentrated around the bubbles. In SEDM, the debris around the bubble was clearly observed by using a transparent electrode and high speed-video camera [19]. In WEDM the process of discharge occurrence and the bubble oscillation are also worth studying using similar transparent parts.

References

REFERENCES

[1] "Web of Science." https://clarivate.com/webofsciencegroup/solutions/web-of-science

[2] B. R. I., Lazarenko N. and Lazarenko, "Electric Spark Method for Machining Metals," *Stanki i Instrument*, vol. 17, 1946.

[3] S. K. Choudhary and R. S. Jadoun, "Current Advanced Research Development of Electric Discharge Machining (EDM): A Review," *International Journal of Research in Advent Technology*, vol. 2, no. 3, pp. 2321–9637, 2014.

[4] G. F. Benedict, "Electrical discharge machining (EDM)," *Non-Traditional Manufacturing Processes*, pp. 231–232, 1987.

[5] R. D. A. K.H Ho, S.T Newman, S Rahimifard, "State of the art in wire electrical discharge machining (WEDM)," *Int J Mach Tools Manuf*, vol. 44, no. 12–13, 2004.

[6] C. J. L. I. Puertas, "A study of optimization of machining parameters for electrical discharge machining of boron carbide," *Materials and Manufacturing Processes*, pp. 1041–1070, 2004.

[7] V. Domnich, S. Reynaud, R. A. Haber, and M. Chhowalla, "Boron carbide: Structure, properties, and stability under stress," *Journal of the American Ceramic Society*, vol. 94, no. 11, pp. 3605–3628, 2011, doi: 10.1111/j.1551-2916.2011.04865.x.

[8] C.MartinB.CalesP.VivierP.Mathieu, "Electrical discharge machinable ceramic composites," *Materials Science and Engineering: A*, vol. 109, pp. 351–356, 1989.

[9] K. W. U. Maradia, M. Scuderi, R. Knaak, M. Boccadoro, I. Beltrami, J. Stirnimann, "Super-finished Surfaces using Meso-micro EDM," *Procedia CIRP*, vol. 6, pp. 157–162, 2013.

[10] I. Ayesta, B. Izquierdo, O. Flaño, J. A. Sánchez, J. Albizuri, and R. Avilés, "Influence of the WEDM process on the fatigue behavior of Inconel® 718," *Int J Fatigue*, vol. 92, pp. 220–233, 2016, doi: 10.1016/j.ijfatigue.2016.07.011.

[11] A. Mandal and A. R. Dixit, "State of art in wire electrical discharge machining process and performance," *International Journal of Machining and Machinability of Materials*, vol. 16, no. 1, pp. 1–21, 2014, doi: 10.1504/IJMMM.2014.063918.

[12] A. Sanchez JA, López de Lacalle LN, Lamikiz, "A computer-aided system for the optimization of the accuracy of the wire electro-discharge machining process," *Int J Comput Integr Manuf*, pp. 413–420, 2004.

[13] "https://www.gfms.com/country_TR/en/products-and-solutions/edm-electrical-discharge-machining/wire-cut-edm/high-speed-machining/cut-200-dedicated.html."

[14] "No Title." https://www.etmm-online.com/firtree-profile-machining-with-wire-edm-to-save-time-and-costs-a-794977/

[15] M. Boccadoro, R. D'Amario, and M. Baumeler, "Towards a better controlled EDM: Industrial applications of a discharge location sensor in an industrial wire electrical discharge machine.," *Procedia CIRP*, vol. 95, pp. 600–604, 2020, doi: 10.1016/j.procir.2020.02.266.

[16] "https://www.gfms.com/country_UK/en/about-gf-machining-solutions/press-room/press-releases/2020/controlling-sparks-edm-wire-life.htm."

[17] M. A. Volosova, A. A. Okunkova, S. V. Fedorov, K. Hamdy, and M. A. Mikhailova, "Electrical Discharge Machining Non-Conductive Ceramics: Combination of Materials," *Technologies (Basel)*, vol. 8, no. 2, p. 32, 2020, doi: 10.3390/technologies8020032.

[18] M. Kunieda, B. Lauwers, K. P. Rajurkar, and B. M. Schumacher, “Advancing EDM through fundamental insight into the process,” *CIRP Ann Manuf Technol*, vol. 54, no. 2, pp. 64–87, 2005, doi: 10.1016/s0007-8506(07)60020-1.

[19] K. M. Yoshida M., “Study on the Distribution of Scattered Debris Generated by a Single Pulse Discharge in EDM Process,” *Int J Educ Method*, vol. 3, pp. 39–47, 1998.

[20] M. Takeuchi, H., Kunieda, “Effects of Volume Fraction of Bubbles in Discharge Gap on Machining Phenomena of EDM,” in *ISEM XV*, 2007, pp. 63–68.

[21] T. Kitamura, M. Kunieda, and K. Abe, “High-speed imaging of EDM gap phenomena using transparent electrodes,” *Procedia CIRP*, vol. 6, pp. 314–319, 2013, doi: 10.1016/j.procir.2013.03.082.

[22] A. Descoeudres, “Characterization of Electrical Discharge Machining Plasmas,” vol. 3542, p. 137, 2006, doi: 10.5075/epfl-thesis-3542.

[23] A. Descoeudres, C. Hollenstein, R. Demellayer, and G. Wälder, “Optical emission spectroscopy of electrical discharge machining plasma,” *J Phys D Appl Phys*, vol. 37, no. 6, pp. 875–882, 2004, doi: 10.1088/0022-3727/37/6/012.

[24] Nagahanumaiah, J. Ramkumar, N. Glumac, S. G. Kapoor, and R. E. Devor, “Characterization of plasma in micro-EDM discharge using optical spectroscopy,” *J Manuf Process*, vol. 11, no. 2, pp. 82–87, 2009, doi: 10.1016/j.jmapro.2009.10.002.

[25] A. Kojima, W. Natsu, and M. Kunieda, “Spectroscopic measurement of arc plasma diameter in EDM,” *CIRP Ann Manuf Technol*, vol. 57, no. 1, pp. 203–207, 2008, doi: 10.1016/j.cirp.2008.03.097.

[26] F. Snoeys, R., Van Dijck, “Investigations of EDM operations by means of thermo mathematical models,” *Annals of the CIRP*, vol. 20, pp. 35–36, 1971.

[27] James V. Beck, “Transient temperatures in a semi-infinite cylinder heated by a disk heat source,” *Int J Heat Mass Transf*, vol. 24, no. 10, pp. 1631–1640, 1981.

[28] James V. Beck, “Large time solutions for temperatures in a semi-infinite body with a disk heat source,” *Int J Heat Mass Transf*, vol. 24, no. 1, pp. 155–164, 1981.

[29] D. D. DiBitonto, P. T. Eubank, M. R. Patel, and M. A. Barrufet, “Theoretical models of the electrical discharge machining process. I. A simple cathode erosion model,” *J Appl Phys*, vol. 66, no. 9, pp. 4095–4103, 1989, doi: 10.1063/1.343994.

[30] D. D. D. M.R. Patel, A. Barrufet, P.T. Eubank, “Theoretical models of the electrical discharge machining process—II: The anode erosion model,” *J Appl Phys*, vol. 66, no. 9, pp. 4104–4111, 1989.

[31] S. H. Yeo, W. Kurnia, and P. C. Tan, “Electro-thermal modelling of anode and cathode in micro-EDM,” *J Phys D Appl Phys*, vol. 40, no. 8, pp. 2513–2521, 2007, doi: 10.1088/0022-3727/40/8/015.

[32] B. Izquierdo, J. A. Sánchez, S. Plaza, I. Pombo, and N. Ortega, “A numerical model of the EDM process considering the effect of multiple discharges,” *Int J Mach Tools Manuf*, vol. 49, no. 3–4, pp. 220–229, 2009, doi: 10.1016/j.ijmachtools.2008.11.003.

[33] S. Banerjee and B. V. S. S. S. Prasad, “Numerical evaluation of transient thermal loads on a WEDM wire electrode under spatially random multiple discharge conditions with and without clustering of sparks,” *International Journal of Advanced Manufacturing Technology*, vol. 48, no. 5–8, pp. 571–580, 2010, doi: 10.1007/s00170-009-2300-8.

[34] H. Singh, “Experimental study of distribution of energy during EDM process for utilization

in thermal models," *Int J Heat Mass Transf*, vol. 55, no. 19–20, pp. 5053–5064, 2012, doi: 10.1016/j.ijheatmasstransfer.2012.05.004.

[35] B. Shao and K. P. Rajurkar, "Modelling of the crater formation in micro-EDM," *Procedia CIRP*, vol. 33, pp. 376–381, 2015, doi: 10.1016/j.procir.2015.06.085.

[36] K. T. Hoang, S. K. Gopalan, and S. H. Yang, "Study of energy distribution to electrodes in a micro-EDM process by utilizing the electro-thermal model of single discharges," *Journal of Mechanical Science and Technology*, vol. 29, no. 1, pp. 349–356, 2015, doi: 10.1007/s12206-014-1241-9.

[37] H. XIA, M. KUNIEDA, and N. NISHIWAKI, "Research on Removal Amount Difference between Anode and Cathode in EDM Process.," *Journal of The Japan Society of Electrical Machining Engineers*, vol. 28, no. 59, pp. 31–40, 1994, doi: 10.2526/jseme.28.59_31.

[38] F. Klocke, S. Schneider, M. Mohammadnejad, L. Hensgen, and A. Klink, "Inverse Simulation of Heat Source in Electrical Discharge Machining (EDM)," *Procedia CIRP*, vol. 58, pp. 1–6, 2017, doi: 10.1016/j.procir.2017.03.178.

[39] Zingerman A.S., "The effect of thermal conductivity upon the electrical erosion of metals," *Journal of Soviet Physics*, vol. 1, pp. 1945–1958, 1956.

[40] Zolotykh B.N., "The mechanism of electrical erosion of metals in liquid dielectric media," *Journal of Soviet Physics*, vol. 4, pp. 1370–1383, 1960.

[41] H. Hocheng, W. T. Lei, and H. S. Hsu, "Preliminary study of material removal in electrical-discharge machining of SiC/Al," *J Mater Process Technol*, vol. 63, no. 1–3, pp. 813–818, 1997, doi: 10.1016/S0924-0136(96)02730-6.

[42] V. Yadav, V. K. Jain, and P. M. Dixit, "Thermal stresses due to electrical discharge machining," *Int J Mach Tools Manuf*, vol. 42, no. 8, pp. 877–888, 2002, doi: 10.1016/S0890-6955(02)00029-9.

[43] "https://nptel.ac.in/content/storage2/courses/113106067/Week1/HeatSources.pdf."

[44] S. N. Joshi and S. S. Pande, "Development of an intelligent process model for EDM," *International Journal of Advanced Manufacturing Technology*, vol. 45, no. 3–4, pp. 300–317, 2009, doi: 10.1007/s00170-009-1972-4.

[45] M. Shabgard, R. Ahmadi, M. Seyedzavvar, and S. N. B. Oliaei, "Mathematical and numerical modeling of the effect of input-parameters on the flushing efficiency of plasma channel in EDM process," *Int J Mach Tools Manuf*, vol. 65, pp. 79–87, 2013, doi: 10.1016/j.ijmachtools.2012.10.004.

[46] H. K. Kansal, S. Singh, and P. Kumar, "Numerical simulation of powder mixed electric discharge machining (PMEDM) using finite element method," *Math Comput Model*, vol. 47, no. 11–12, pp. 1217–1237, 2008, doi: 10.1016/j.mcm.2007.05.016.

[47] K. Ikai, T., Hashiguchi, "Heat input for crater formation in EDM," in *ISEM XI*, 1995, pp. 163–170.

[48] Z. Chen, G. Zhang, F. Han, Y. Zhang, and Y. Rong, "Determination of the optimal servo feed speed by thermal model during multi-pulse discharge process of WEDM," *Int J Mech Sci*, vol. 142–143, no. September 2017, pp. 359–369, 2018, doi: 10.1016/j.ijmecsci.2018.05.006.

[49] A. Erden, "Effect of materials on the mechanism of electric discharge machining (EDM)," *J Eng Mater Technol*, vol. 108, pp. 247–251, 1983.

[50] J. Spur, G., Schönbeck, "Anode Erosion in Wire-EDM - A Theoretical Model," *CIRP Annals*, vol. 42, pp. 253–256, 1993.

[51] W. Natsu, M. Shimoyamada, and M. Kunieda, “Study on expansion process of EDM arc plasma,” *JSME International Journal, Series C: Mechanical Systems, Machine Elements and Manufacturing*, vol. 49, no. 2, pp. 600–605, 2006, doi: 10.1299/jsmec.49.600.

[52] S. T. J. P.C. Pandey, “Plasma channel growth and the resolidified layer in EDM,” *Precis Eng*, vol. 8, no. 2, pp. 104–110, 1986.

[53] S. Banerjee, B. V. S. S. S. Prasad, and P. K. Mishra, “Analysis of three-dimensional transient heat conduction for predicting wire erosion in the wire electrical discharge machining process,” *J Mater Process Technol*, vol. 65, no. 1–3, pp. 134–142, 1997, doi: 10.1016/0924-0136(95)02253-8.

[54] F. Klocke, M. Mohammadnejad, M. Zeis, and A. Klink, “Investigation on the Variability of Existing Models for Simulation of Local Temperature Field during a Single Discharge for Electrical Discharge Machining (EDM),” *Procedia CIRP*, vol. 68, no. April, pp. 260–265, 2018, doi: 10.1016/j.procir.2017.12.059.

[55] K. Oßwald, I. Lochmahr, H. P. Schulze, and O. Kröning, “Automated Analysis of Pulse Types in High Speed Wire EDM,” *Procedia CIRP*, vol. 68, no. April, pp. 796–801, 2018, doi: 10.1016/j.procir.2017.12.157.

[56] Masanori Kunieda and Takanobu Nakashima, “Factors Determining Discharge Location in EDM,” *International Journal of Electrical Machining*, pp. 53–58, 1998.

[57] K. Morimoto and M. Kunieda, “Sinking EDM simulation by determining discharge locations based on discharge delay time,” *CIRP Ann Manuf Technol*, vol. 58, no. 1, pp. 221–224, 2009, doi: 10.1016/j.cirp.2009.03.069.

[58] X. Y. Jiajing TANG, “Study on Influence of Tool Electrode Material on Discharge Delay Time in EDM,” *Journal of the Japan Society for Precision Engineering*, vol. 85, no. 11, 2019.

[59] P. I. Journal and E. Machining, “Fundamental Study on Quantitative Estimation of Discharge Delay Time in EDM,” *International Journal of Electrical Machining*, vol. 14, no. 0, pp. 43–50, 2009, doi: 10.2526/ijem.14.43.

[60] I. ARAIE, S. SANO, and M. KUNIEDA, “Effect of Electrode Surface Profile on Discharge Delay time in Electrical Discharge Machining,” *Denki Kako Gakkaishi*, vol. 41, no. 97, pp. 61–68, 2007, doi: 10.2526/jseme.41.61.

[61] K. Y. Masanori Kunieda, “Study on Debris Movement in EDM Gap,” *International Journal of Electrical Machining*, vol. 2, 1997.

[62] J. W. Murray, J. Sun, D. V. Patil, T. A. Wood, and A. T. Clare, “Physical and electrical characteristics of EDM debris,” *J Mater Process Technol*, vol. 229, pp. 54–60, 2016, doi: 10.1016/j.jmatprotec.2015.09.019.

[63] K. Oßwald, J. Woidasky, A. M. Hoffmann, and M. Moser, “Suitability of electrical discharge machining debris particles for usage as a powder for selective laser melting: an explorative study,” *Progress in Additive Manufacturing*, vol. 4, no. 4, pp. 443–449, 2019, doi: 10.1007/s40964-019-00080-y.

[64] Y. Liu, H. Chang, W. Zhang, F. Ma, Z. Sha, and S. Zhang, “A simulation study of debris removal process in ultrasonic vibration assisted electrical discharge machining (EDM) of deep holes,” *Micromachines (Basel)*, vol. 9, no. 8, 2018, doi: 10.3390/mi9080378.

[65] W. Zhang, Y. Liu, S. Zhang, F. Ma, P. Wang, and C. Yan, “Research on the Gap Flow Simulation of Debris Removal Process for Small Hole EDM Machining with Ti Alloy,” no. Icmmcce, pp. 2121–2126, 2015, doi: 10.2991/icmmcce-15.2015.409.

[66] J. Wang and F. Han, “Simulation model of debris and bubble movement in consecutive-pulse discharge of electrical discharge machining,” *Int J Mach Tools Manuf*, vol. 77, pp. 56–65, 2014, doi: 10.1016/j.ijmachtools.2013.10.007.

[67] S. Cetin, A. Okada, and Y. Uno, “Effect of debris distribution on wall concavity in deep-hole EDM,” *JSME International Journal, Series C: Mechanical Systems, Machine Elements and Manufacturing*, vol. 47, no. 2, pp. 553–559, 2004, doi: 10.1299/jsmec.47.553.

[68] M. Tanjilul, A. Ahmed, A. S. Kumar, and M. Rahman, “A study on EDM debris particle size and flushing mechanism for efficient debris removal in EDM-drilling of Inconel 718,” *J Mater Process Technol*, vol. 255, no. December 2017, pp. 263–274, 2018, doi: 10.1016/j.jmatprotec.2017.12.016.

[69] “https://www.novotec-edm.com/wire-selection.”

[70] R. Kumar, “EFFECT OF DIFFERENT WIRE ELECTRODE ’ S MATERIAL ON THE EFFECT OF DIFFERENT WIRE ELECTRODE ’ S MATERIAL ON THE PERFORMANCE OF WIRE ELECTRODE DISCHARGE MACHINING,” no. April, pp. 1–6, 2017.

[71] “https://www.southernfabsales.com/blog/whats-the-best-wire-choice-for-electrical-discharge-machining-edm.”

[72] Y. F. Luo, “Rupture failure and mechanical strength of the electrode wire used in wire EDM,” *J. Mater. Process. Technol.*, vol. 94, no. 2, pp. 208–215, 1999.

[73] G. G. N. Kinoshita, M. Fukui, “Control of wire-EDM preventing electrode from breaking,” *Ann. CIRP*, vol. 31, no. 1, pp. 111–114, 1982.

[74] T. Itoh, “Wire EDM for detecting discharge concentrations using inductance”

[75] P. K. Banerjee, S., Prasad, B.V.S.S.S., Mishra, “A simple model to estimate the termal loads on an EDM wire electrode,” *J. Mater. Process. Technol.*, vol. 39, no. 3–4, pp. 305–317, 1993.

[76] N. Tosun and C. Cogun, “An investigation on wire wear in WEDM,” *J Mater Process Technol*, vol. 134, no. 3, pp. 273–278, 2003, doi: 10.1016/S0924-0136(02)01045-2.

[77] M. J. Saha, S., Pachon, M., Ghoshal, A., Schulz, “Finite element modeling and optimization to prevent wire breakage in electro-discharge machining,” *Mech. Res. Commun*, vol. 31, no. 4, pp. 451–463, 2004.

[78] A. A. Fedorov, A. I. Blesman, D. V. Postnikov, D. A. Polonyankin, G. S. Russkikh, and A. V. Linovsky, “Investigation of the impact of Rehbinder effect, electrical erosion and wire tension on wire breakages during WEDM,” *J Mater Process Technol*, vol. 256, no. April 2017, pp. 131–144, 2018, doi: 10.1016/j.jmatprotec.2018.02.002.

[79] A. P.M. and C. D., “ANFIS modelling of mean gap voltage variation to predict wire breakages during wire EDM of Inconel 718,” *CIRP J Manuf Sci Technol*, vol. 31, pp. 153–164, 2020, doi: 10.1016/j.cirpj.2020.10.007.

[80] S. Das and S. N. Joshi, “Measurement and analysis of molybdenum wire erosion and deformation during wire electric discharge machining of Ti-6Al-4V alloy,” *Measurement (Lond)*, vol. 179, no. April, p. 109440, 2021, doi: 10.1016/j.measurement.2021.109440.

[81] K. N. Kunieda M, Kojima H, “On-Line Detection of EDM Spark Locations by Multiple Connection of Branched Electric Wires,” *Annals of the CIRP*, vol. 39, no. 1, pp. 171–174, 1990.

[82] F. Han, M. Kunieda, T. Sendai, and Y. Imai, “Simulation of Wedm Using Discharge Location Searching Algorithm,” *Initiatives of Precision Engineering at the Beginning of a Millennium*, pp. 319–323, 2005, doi: 10.1007/0-306-47000-4_62.

[83] A. Okada, Y. Uno, M. Nakazawa, and T. Yamauchi, “Evaluations of spark distribution and wire vibration in wire EDM by high-speed observation,” *CIRP Ann Manuf Technol*, vol. 59, no. 1, pp. 231–234, 2010, doi: 10.1016/j.cirp.2010.03.073.

[84] Z. Chen, H. Zhou, Z. Yan, F. Han, and H. Yan, “A new high-speed observation system for evaluating the spark location in WEDM of Inconel 718,” *Journal of Materials Research and Technology*, vol. 13, pp. 184–196, 2021, doi: 10.1016/j.jmrt.2021.04.064.

[85] F. Han, M. Kunieda, and H. Asano, “Improvement of Controllability of Discharge Locations in WEDM,” *International Journal of Electrical Machining*, vol. 9, no. 0, pp. 37–42, 2004, doi: 10.2526/ijem.9.37.

[86] S. Das, M. Klotz, and F. Klocke, “EDM simulation: Finite element-based calculation of deformation, microstructure and residual stresses,” *J Mater Process Technol*, vol. 142, no. 2, pp. 434–451, 2003, doi: 10.1016/S0924-0136(03)00624-1.

[87] J. F. Liu and Y. B. Guo, “Thermal Modeling of EDM with Progression of Massive Random Electrical Discharges,” *Procedia Manuf*, vol. 5, pp. 495–507, 2016, doi: 10.1016/j.promfg.2016.08.041.

[88] A. Tlili, F. Ghanem, and N. Ben Salah, “A contribution in EDM simulation field,” *International Journal of Advanced Manufacturing Technology*, vol. 79, no. 5–8, pp. 921–935, 2015, doi: 10.1007/s00170-015-6880-1.

[89] R. Pérez, J. Carron, M. Rappaz, G. Wälder, B. Revaz, and R. Flükiger, “Measurement and metallurgical modeling of the thermal impact of EDM discharges on steel,” *Proceedings of the 15th International Symposium on Electromachining, ISEM 2007*, no. August 2015, pp. 17–22, 2007.

[90] G. Zhang, H. Huang, Z. Zhang, and Y. Zhang, “Study on the effect of three dimensional wire vibration on WEDM based on a novel thermophysical model,” *International Journal of Advanced Manufacturing Technology*, vol. 100, no. 5–8, pp. 2089–2101, 2019, doi: 10.1007/s00170-018-2796-x.

[91] S. Senkathir and K. Sai Sandeep, “Finite element modelling and machining using WEDM,” *IOP Conf Ser Mater Sci Eng*, vol. 402, no. 1, 2018, doi: 10.1088/1757-899X/402/1/012076.

[92] A. Kumar, D. K. Bagal, and K. P. Maity, “Numerical modeling of Wire Electrical Discharge machining of super alloy inconel 718,” *Procedia Eng*, vol. 97, pp. 1512–1523, 2014, doi: 10.1016/j.proeng.2014.12.435.

[93] P. K. Singh, “Fea for WEDM Process of Titanium Alloy,” vol. 3, pp. 284–293, 2017.

[94] S. K. Hargrove and D. Ding, “Determining cutting parameters in wire EDM based on workpiece surface temperature distribution,” *International Journal of Advanced Manufacturing Technology*, vol. 34, no. 3–4, pp. 295–299, 2007, doi: 10.1007/s00170-006-0609-0.

[95] S. Shahane and S. S. Pande, “Development of a Thermo-Physical Model for Multi-spark Wire EDM Process,” *Procedia Manuf*, vol. 5, pp. 205–219, 2016, doi: 10.1016/j.promfg.2016.08.019.

[96] W. Rajurkar, K.P., Wang, “Thermal modeling and on-line monitoring of wire-EDM,” *J. Mater. Process. Technol.*, vol. 38, pp. 417–430, 1993.

[97] S. Kumar. Vikas Kumar, A. Verma, “Statically Approach towards Finite Element Analysis of Temperature Distribution and Residual Stresses in Wire Electrical Discharge Machining Process,” *Imperial Journal of Interdisciplinary Research*, vol. 2, no. 12, 2016.

[98] S. N. Joshi. Jitendra Kumar, Sanghamitra Das, “Three-Dimensional Numerical Modelling of Temperature Profiles on the Wire Electrode During Wire Electric Discharge Machining Process,” *Advances in Mechanical Engineering*.

[99] S. P, J. AK, and M. SK, “Analysis of Wire Electrode Discharge Machining Process using FEA,” *J Appl Mech Eng*, vol. 6, no. 5, 2017, doi: 10.4172/2168-9873.1000288.

[100] B. Boipai, “FEM analysis for WEDM process FEM analysis for WEDM process,” 2014.

[101] S. Das and S. N. Joshi, *Thermal Modeling and Simulation of Crater Generation on Wire Electrode During Wire EDM Operation*. Springer Singapore, 2020. doi: 10.1007/978-981-32-9487-5_10.

[102] S. Das and S. N. Joshi, “Estimation of wire strength based on residual stresses induced during wire electric discharge machining,” *J Manuf Process*, vol. 53, no. March, pp. 406–419, 2020, doi: 10.1016/j.jmapro.2020.03.015.

[103] K. Joshi, G. Sharma, G. Dongre, and S. S. Joshi, “Numerical Modelling of Wire-EDM for Predicting Erosion Rate of Silicon,” *Journal of The Institution of Engineers (India): Series C*, vol. 98, no. 1, pp. 63–73, 2017, doi: 10.1007/s40032-016-0237-x.

[104] T. I. Masanori Kunieda, Haruka Takeuchi, Yuya Kusakabe, Hirokazu Sunagawa, “Clarifying EDM Gap Phenomena by Gas Chromatography Analysis of Bubbles,” *IJEM*, vol. 16, pp. 15–19, 2011.

[105] N. T. Hayakawa S, Doke T, Itoigawa F, “Observation of Bubble Expansion and Flying Debris in Parallel Flat Gap Space in Electrical Discharge Machining,” *IJEM*, vol. 14, pp. 29–35, 2009.

[106] R. P.] Toboła D, Brostow W, Czechowski K, “Improvement of wear resistance of some cold working tool steels,” *Wear*, vol. 382, pp. 29–39, 2017.

[107] L. R. Thomas R. Newton, Shreyes N. Melkote, Thomas R. Watkins, Rosa M. Trejo, “Investigation of the effect of process parameters on the formation and characteristics of recast layer in wire-EDM of Inconel 718,” *Mater. Sci. Eng. A.*, vol. 513, pp. 208–215, 2009.

[108] P. D. Bredgauer IO, Polonyankin DA, Fedorov AA, Blesman AI, Linovsky AV, “Investigating wire breakage during EDM with fractographic analysis,” *J. Phys. Conf. Ser.*, vol. 1791, 2021.

[109] A. Gatto, E. Bassoli, L. Denti, and L. Iuliano, “Bridges of debris in the EDD process: Going beyond the thermo-electrical model,” *J Mater Process Technol*, vol. 213, no. 3, pp. 349–360, 2013, doi: 10.1016/j.jmatprotec.2012.10.020.

[110] M. Tanjilul, A. Ahmed, A. S. Kumar, and M. Rahman, “A study on EDM debris particle size and flushing mechanism for efficient debris removal in EDM-drilling of Inconel 718,” *J Mater Process Technol*, vol. 255, no. December 2017, pp. 263–274, 2018, doi: 10.1016/j.jmatprotec.2017.12.016.

[111] H. Scientific, *A guidebook to particle size analysis*. 2017.

[112] “https://en.wikipedia.org/wiki/Scanning_electron_microscope.”

[113] X. Yang, J. Guo, X. Chen, and M. Kunieda, “Molecular dynamics simulation of the material removal mechanism in micro-EDM,” *Precis Eng*, vol. 35, no. 1, pp. 51–57, 2011, doi: 10.1016/j.precisioneng.2010.09.005.

[114] H. Guo, J., Zhang, G., Huang, Y., Ming, W., Liu, M., Huang, “Investigation of the removing process of cathode material in micro-EDM using an atomistic-continuum model,” *Appl Surf Sci*, vol. 315, pp. 323–336, 2014.